DOTTORATO DI RICERCA IN

FISICA

Ciclo 36

Settore Concorsuale: 02/A1 - FISICA SPERIMENTALE DELLE INTERAZIONI FONDAMENTALI

Settore Scientifico Disciplinare: FIS/01 - FISICA SPERIMENTALE

VALIDATION OF SIPMS FOR THE DUNE FAR DETECTOR PHOTON DETECTION SYSTEM THROUGH THE DEVELOPMENT AND COMMISSIONING OF A CRYOGENIC FACILITY

Presentata da: Elisabetta Montagna

Coordinatore Dottorato

Alessandro Gabrielli

Supervisore

Alessandro Gabrielli

Co-supervisore

Michele Pozzato

Esame finale anno 2024

Abstract

The Deep Underground Neutrino Experiment (DUNE) is a next generation long baseline neutrino experiment in preparation in the US. Its main scientific goals are the measurement of neutrino parameters such as the CP-violating phase, δ_{CP}, determine the neutrino mass ordering, and precisely measure the oscillation angles θ_{23} and θ_{13}.

DUNE will be implemented with a Near Detector and a Far Detector, located at 500 m and 1300 km, respectively, along the neutrino beamline originating at Fermilab. The FD complex will consist of four detectors modules of Liquid Argon Time Projection Chambers, instrumented with a Photon Detection System (PDS) to detect the scintillation light produced inside the active volume. The PDS will be based on light collectors coupled to Silicon Photomultipliers (SiPMs) working in a Liquid Argon environment.

This thesis is focused on the test activities and the validation of the photosensors for the experiment, along with the optimization of the PDS performance for its first module. The results of a selection process of SiPMs are reported, as well as the full characterization of these devices at room and cryogenic temperatures (77 K). Based on these results, the SiPMs for the first module prototype (ProtoDUNE, at CERN) were produced. A description of the semi-automated system used to validate these sensors is given along with the results obtained.

A campaign of validation of all the SiPMs ($\sim$300000) which will be eventually installed in the first DUNE Far Detector module is currently undergoing using this system. The results for the samples tested up to now are here presented.

Contents

Introduction

Neutrino physics is an active field of research that has attracted many studies in the past decades. One of the main topics is the neutrino flavour oscillation phenomenon, which has been explored by various experiments that have improved our understanding of the neutrino properties. However, there are still some unresolved questions, such as the determination of the neutrino mass ordering and the detection of a possible CP violation in the leptonic sector. These challenges motivate the development of a new generation of neutrino oscillation experiments.

The Deep Underground Neutrino Experiment (DUNE) is a future international project that aims to address these questions. In addition to its primary goal, DUNE will also conduct a physics programme that includes the observation of supernova neutrinos and the search for physics beyond the standard model.

DUNE is a dual site experiment with a Near Detector (ND) located at Fermilab and a Far Detector (FD) situated in South Dakota, at a distance of ~1300 km and exposed to an intense neutrino beam. The ND complex will consist of three different detectors that mainly serve to reduce the systematic uncertainties for the neutrino oscillation measurements at the FD. The FD will consist of four multi-kiloton modules of Liquid Argon Time Projection Chambers (LAr TPCs), placed about 1.5 km underground.

The neutrino interactions in the TPCs will be reconstructed from the tracks of the secondary charged particles yielding scintillation light (which provides the event reference time) and free charge carriers by ionization along their path in Liquid Argon (LAr). To collect light, the FD will be equipped with a Photon Detection System (PDS) based on light collectors coupled to Silicon Photomultipliers (SiPMs) operating in a Liquid Argon bath. Considering the demanding working conditions of these photosensors, a careful selection of the best SiPM technology that meets the experiment requirements has been performed, followed by a necessary validation campaign of all the SiPMs to be installed in the PDS of the first module of the FD.

This thesis focuses on the activity that I performed for the the selection of SiPMs technology and the sensors' validation campaign. The aim was to verify the compatibility of the photosensors' performances with the experiment specifications

1

and to ensure a uniform response of the PDS. I participated in the development and commissioning of a cryogenic facility used to test the samples produced first for a DUNE prototype (ProtoDUNE, CERN) and then for the first DUNE Far Detector module.

The thesis is organized as follows: Chapter 1 gives an overview of the neutrino oscillation phenomenon and a summary of the experimental results in this field. In Chapter 2 a description of the DUNE design and physics programme is presented. The working principle of a Liquid Argon Time Projection Chamber (LAr TPC) is illustrated along with the two configuration for the Single Phase technology that will be implemented in DUNE: the Horizontal Drift and the Vertical Drift, in the first and second LAr TPC module, respectively. Chapter 3 provides a detailed description of the Photon Detection System for both the Horizontal and the Vertical Drift LAr TPCs. It is here also presented a study I carried out during my training period at CERN, on the optimization of the PDS electronic box design. Chapter 4 presents the down-selection campaign for identifying the optimal SiPMs model based on the experiment requirements, chosen from the proposed options. The selection criteria and the results obtained during their characterization are reported along with the description of a newly observed "signal burst" phenomenon. In Chapter 5 the development and commissioning phase of the cryogenic apparatus for the mass test campaign is detailed. The results obtained through this system to validate the SiPMs production for ProtoDUNE and that for the first module of the DUNE Far Detector are here presented.

Chapter 1

Neutrino Physics

1.1 Neutrinos in the Standard Model

In the Standard Model (SM) particles are divided into two main categories: *gauge bosons* and *fermions*. The Gauge bosons (spin 1) are the mediators of fundamental interactions. The *photon* is the mediator of the electromagnetic interaction, $W^{\pm}$ and Z^0 bosons are the mediators of the weak interaction and *gluons* of the strong interaction. In addition, the *Higgs Boson* (spin 0) is responsible of the mass generation through the Higgs mechanism [1]. In the SM fermions (spin 1/2) are divided into *leptons* and *quarks*. Both of them are present in three different generations. In the case of leptons, each family is composed of a charged lepton (e, μ, τ), coupled to a neutrino of the corresponding flavour (ν_e, ν_μ, ν_τ). In this description, fermions are coupled in doublets of left chirality (Tab. 1.1) and singlets of right chirality. Neutrinos are left-handed only and antineutrinos can be right-handed only.

	flavour			charge
quarks	$\begin{pmatrix} u \\ d \end{pmatrix}_L$	$\begin{pmatrix} c \\ s \end{pmatrix}_L$	$\begin{pmatrix} t \\ b \end{pmatrix}_L$	+2/3
				-1/3
leptons	$\begin{pmatrix} e \\ \nu_e \end{pmatrix}_L$	$\begin{pmatrix} \mu \\ \nu_\mu \end{pmatrix}_L$	$\begin{pmatrix} \tau \\ \nu_\tau \end{pmatrix}_L$	-1
				0

Table 1.1: Fermions families in the Standard Model description.

Neutrinos in the SM are massless neutral particles. They can interact only weakly through Charge Current (CC) interaction by exchanging of a $W^{\pm}$ boson, or through Neutral Current (NC) mediated by a Z^0 boson. The number of neutrino families has been confirmed to be only three by the study of the Z boson decay width at the e^+e^- LEP collider (Fig. 1.1) [2].
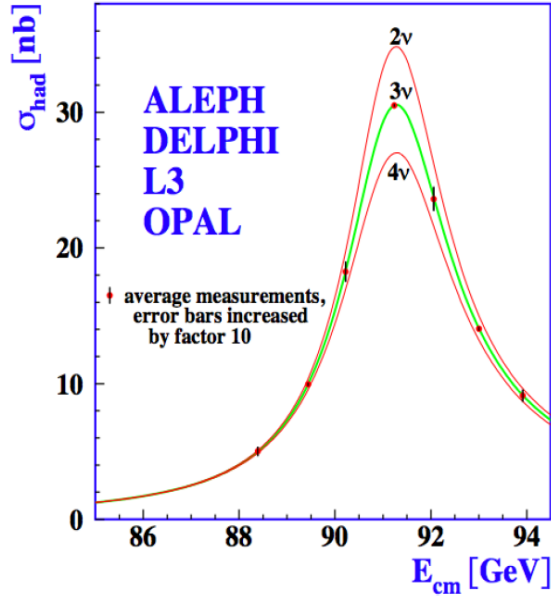
Figure 1.1: Theoretical predictions of the hadron production cross section as a function of the center of mass energy, for different numbers of neutrinos families. Measurements from LEP are compatible with a three families structure of neutrinos [2].

Even if neutrinos in the SM are massless particles, the observation of neutrino mixing, which implies a non-zero neutrino mass, undermines this assumption. Differents experiments have demonstrated neutrino mixing giving evidence of neutrino mass and of physics beyond the SM. Several methods are used to determine the absolute neutrino mass. From studies on the Tritium β-decay, the KATRIN experiments has set an upper limit of m_ν <0.8 eV at 90% of CL [3]. Experiments exploiting cosmological data are able to provide an upper limit of the sum of the three flavours masses. The most robust constraints come from Planck2018 temperature and polarization data alone: $\Sigma_i m_\nu$ <0.26 eV (95% CL) [4].

1.2   Massive neutrinos

In the Standard Model, particles gain mass through the Brout-Englert-Higgs (BEH) mechanism. Altought this mechanism produces masses for most of the fermions, it keeps neutrinos massless. Neutrino mass can be introduced following three different approaches. In the first scenario, neutrino is described as a Dirac particle. Following this approach, the Dirac mass term of the Lagrangian is:

$$\mathcal{L}_m = -m_D(\overline{\nu}_L \nu_R + \overline{\nu}_R \nu_L) \qquad (1.1)$$

4

A non-zero Dirac mass requires neutrino to have both left and right-handed chiral state. So far, there is no evidence of a right-handed neutrino. This leads to the hypothesis that they can not interact weakly, acquiring the definition of *sterile* neutrinos. Left-handed neutrinos, which conversely are experimentally observed, would be then called *active* neutrinos. In this scenario the leptonic number is conserved and neutrino and antineutrino are different particles ($\nu \neq \bar{\nu}$).

In the second scenario, neutrino is a Majorana particle. The Majorana mass term of the Lagrangian is then written using only left-handed component of the field:

$$\mathcal{L}_m = -\frac{1}{2} m_M (\bar{\nu}_L^c \nu_L + \bar{\nu}_L \nu_L^c), \tag{1.2}$$

where $\nu^c = C\gamma^0 \nu^*$ is the neutrino field term to which has been applied the charge conjugation matrix C and $\nu_L^c \equiv (\nu_L)^c = \frac{(1+\gamma_5)}{2}\nu^c$. Under this assumption, neutrino and antineutrino are the same particle ($\nu = \bar{\nu}$) and the leptonic number is not conserved.

The last scenario considers a more unified approach which is a combination of Eq. 1.1 and 1.2, plus a Dirac-Majorana mass term m_R of right chirality. The Lagrangian can be now written as:

$$\mathcal{L} = -\frac{1}{2} \begin{pmatrix} \bar{\nu}_L & \bar{\nu}_R^c \end{pmatrix} \begin{pmatrix} m_L & m_D \\ m_D & m_R \end{pmatrix} \begin{pmatrix} \nu_L \\ \nu_R^c \end{pmatrix}. \tag{1.3}$$

The mass matrix can be diagonalized through a unitary matrix $\mathcal{U}$, obtaining the mass eigenstates. The corrisponding mass eigenvalues are:

$$m_\pm = \frac{1}{2} \left[(m_L + m_R) \pm \sqrt{(m_L - m_R)^2 + 4m_D^2} \right]. \tag{1.4}$$

In the case $m_L = m_R = 0$ neutrino is a Dirac particles as described before, while $m_D = 0$ corresponds to neutrino as Majorana particles. A particular case is when $m_L = 0$ e $m_R \gg m_D$. From the diagonalization of the mass matrix one can obtain two mass eigenvalues, a light mass term m_- and a heavy mass term m_+:

$$m_- \simeq \frac{m_D^2}{m_R}, \quad m_+ \simeq m_R(1 + \frac{m_D^2}{m_R^2}) \simeq m_R. \tag{1.5}$$

This scenario describes the Type I See-Saw mechanism. In this mechanism m_- would correspond to the active neutrino mass of the experimentally observed neutrino, while m_+ to the heavy sterile neutrino one. The reason why the active neutrino mass is light is because it is associated with a very massive particle ($m_R \gg m_D$).

1.3 Neutrino Oscillations

Neutrino flavour mixing is a natural consequence of massive neutrinos. The phenomenon, similarly to the quark sector, is due to the fact that flavour and mass eigenstates do not coincide. It was first proposed by Bruno Pontecorvo in 1957 as neutrino oscillations .

Neutrino flavour eigenstates ν_α ($\nu_\alpha = \nu_e, \nu_\mu, \nu_\tau$) are described as a linear combination of mass eigenstates ν_i ($\nu_i = \nu_1, \nu_2, \nu_3$):

$$|\nu_\alpha\rangle = \sum_i U_{\alpha i} |\nu_i\rangle \tag{1.6}$$

where U is the unitary matrix of Pontecorvo-Maki-Nakagawa-Sakata (PMNS).

Oscillation in vacuum

In the case of oscillation in vacuum, the time evolution of the flavour eigenstates ν_α, is described as:

$$|\nu_\alpha(t)\rangle = \sum_i U_{\alpha i} |\nu_i(t)\rangle \tag{1.7}$$

where the neutrino state is considered relativistic and described by plane wave equation:

$$|\nu_i(t)\rangle = e^{-E_i t} |\nu(0)\rangle . \tag{1.8}$$

Assuming same momentum, the energies of the mass eigenstates are:

$$E_i = \sqrt{p^2 + m_i} \simeq p + \frac{m_i^2}{2p}. \tag{1.9}$$

The so called *appearance* probability that a neutrino generated with flavour α oscillates into a neutrino of different flavour β after a time t is:

$$P(\nu_\alpha \to \nu_\beta) = |\langle \nu_\alpha \, | \, \nu_\beta(t) \rangle|^2 \tag{1.10}$$

which is:

$$= \left| \sum_i U_{\beta i} e^{-E_i t} U_{\alpha i}^* \right|^2 = \sum_i \sum_j U_{\alpha i}^* U_{\beta i} U_{\alpha j} U_{\beta j}^* e^{-(E_i - E_j)t} \tag{1.11}$$

In the assumption of relativistic neutrinos, $t \simeq L$ and $p \simeq E$. Taking into account this approximation and Eq. 1.8, the exponent's argument assumes the form:

$$(E_i - E_j)t \simeq \frac{(m_i^2 - m_j^2)}{2p} t \simeq \frac{\Delta m_{ij}^2}{2p} t \simeq \frac{\Delta m_{ij}^2}{2E} L \tag{1.12}$$

where Δm_{ij}^2 is the mass squared difference between two different mass eigenstates and L is the distance travelled by the neutrino. The factor $\Delta m_{ij}^2 L/2E$ describes the sensitivity of the experiments to the oscillations parameters.

The oscillation probability becomes:

$$P(\nu_\alpha \to \nu_\beta) = \delta_{\alpha\beta} - 4 \sum_{i>j} \text{Re}(U_{\alpha i}^* U_{\beta i} U_{\alpha j} U_{\beta j}^* \sin^2[1.27\Delta m_{ij}^2 (L/E)])$$
$$+ 2 \sum_{i>j} \text{Im}(U_{\alpha i}^* U_{\beta i} U_{\alpha j} U_{\beta j}^* \sin^2[2.54\Delta m_{ij}^2 (L/E)]). \tag{1.13}$$

In the simplified case of considering only two neutrino flavours involved in the mixing, the oscillation probability is (for $\alpha \neq \beta$):

$$P(\nu_\alpha \to \nu_\beta) = \sin^2 2\theta \cdot \sin^2 \left(1.27 \frac{\Delta m^2 [\text{eV}^2] L[\text{km}]}{E[\text{GeV}]}\right). \tag{1.14}$$

The shape of the probability depends on two factors: the amplitude of the sinusoidal oscillation (equal to $\sin^2 2\theta$ where θ is the *mixing* angle), and the oscillation length (distance between two consecutive maxima) defined as:

$$L_{osc} = \frac{4\pi E \frac{\hbar}{c^3}}{\Delta m^2} = 2.48[\text{km}] \frac{E[\text{GeV}]}{\Delta m^2 [\text{eV}]^2}. \tag{1.15}$$

Eq. 1.14 has a minimum value equal to zero for $L=0$ or multiple of L_{osc}, and a maximum value of $\sin^2 2\theta$ for $L = (n + \frac{1}{2})L_{osc}$.

The ratio L/E plays a crucial role in the optimization of experiments aimed to study neutrino oscillations, by determing their sensitivity to Δm^2. Usually neutrino oscillations experiments are classified, by the different value of this ratio, into two main categories:

- short-baseline (SBL) experiments. They exploit neutrino sources of reactor or accelerator type. The propagation distance between the source and the detector is usually short. The range for L/E and their sensitivity is:

$$\text{Reactors}: \quad \frac{L}{E} \lesssim 10\,\text{m/MeV}, \quad \text{which implies} \quad \Delta m^2 \gtrsim 0.1\,\text{eV}^2;$$
$$\text{Accelerators}: \quad \frac{L}{E} \lesssim 1\,\text{km/GeV}, \quad \text{which implies} \quad \Delta m^2 \gtrsim 1\,\text{eV}^2. \tag{1.16}$$

- long-baseline (LBL) experiments. In this category, along with reactor and accelerator neutrinos source, there are also atmospheric neutrinos source.

The propagation distance is larger than in the SBL case. The ratio L/E in the reactor and accelerator case is similar, and so their sensitivity:

$$\text{Reactors:} \quad L/E \lesssim 10^3 \text{ m/MeV}$$
$$\text{Accelerators:} \quad L/E \lesssim 10^3 \text{ km/GeV} \quad \text{which implies} \quad \Delta m^2 \gtrsim 10^{-3} \text{ eV}^2. \tag{1.17}$$

In the case of atmospheric neutrino source, considering both *upgoing* and *downgoing* neutrinos, the range in the propagation distance is wider and gives:

$$\frac{L}{E} \lesssim 10^4 \, \text{km/GeV}, \quad \text{which implies} \quad \Delta m^2 \gtrsim 10^{-4} \, \text{eV}^2. \tag{1.18}$$

A more complete description of neutrino oscillation, extends the mixing to the case of three active neutrinos. The notation then takes the form:

$$\begin{pmatrix} \nu_e \\ \nu_\mu \\ \nu_\tau \end{pmatrix} = U_{PMNS} \begin{pmatrix} \nu_1 \\ \nu_2 \\ \nu_3 \end{pmatrix} \tag{1.19}$$

where the PMNS matrix can be parametrized as:

$$U_{PMNS} = \begin{pmatrix} 1 & 0 & 0 \\ 0 & c_{23} & s_{23} \\ 0 & -s_{23} & c_{23} \end{pmatrix} \times \begin{pmatrix} c_{13} & 0 & s_{13}e^{-i\delta} \\ 0 & 1 & 0 \\ -s_{13}e^{i\delta} & 0 & c_{13} \end{pmatrix}$$
$$\times \begin{pmatrix} c_{12} & s_{12} & 0 \\ -s_{12} & c_{12} & 0 \\ 0 & 0 & 1 \end{pmatrix} \times \begin{pmatrix} 1 & 0 & 0 \\ 0 & e^{i\alpha_1} & 0 \\ 0 & 0 & e^{i\alpha_2} \end{pmatrix} \tag{1.20}$$

with $c_{ij} = \cos\theta_{ij}$, $s_{ij} = \sin\theta_{ij}$ (θ_{ij} mixing angles) and α_i being the Majorana phases. The Dirac phase δ is non-zero only in the case of CP violation in the leptonic sector.

Summarizing the description of the neutrino oscillation phenomenon we can underline few important parameters. The phenomenon requires $\Delta m_{ij}^2 \neq 0$. The oscillation probability depends on three mixing angles $\theta_1, \theta_2, \theta_3$ and on two independent mass squared differences. These latter ones are usually defined as Δm_{21}^2 and Δm_{31}^2, while Δm_{32}^2 is $\Delta m_{32}^2 = \Delta m_{31}^2 - \Delta m_{21}^2$. To observe a possible CP violation in the leptonic sector, the δ phase has to be $\delta_{CP} \neq 0, \pi$. This condition would represent an asymmetry between neutrino and antineutrino oscillations. Experiments aimed to study neutrino oscillation have to be design in order to optimized their sensitivity to these parameters.
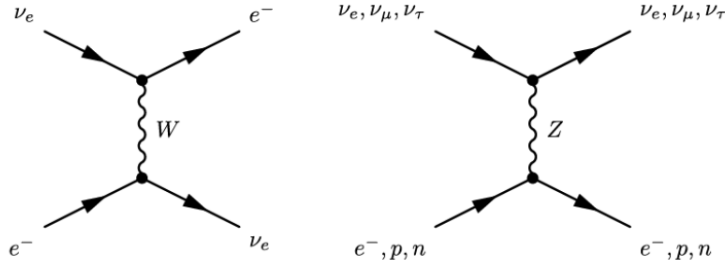
Figure 1.2: Feynman diagram of Charged Current interaction (left) and Neutral Current interaction (right) in matter. It is shown how just electron neutrinos can partecipate in CC interactions, while all neutrino flavours can be involved in NC interactions.

Oscillation in matter

A more general case is neutrinos propagation in matter. When travelling through matter, the coherent forward scattering of neutrino with electrons and nucleons, can change the oscillation probability from the one described in vacuum. Although the interaction probability is very low, their oscillation pattern can be modified. The scattering can be induced by both Charge Current (CC) and Neutral Current (NC) interactions. While in the NC case all neutrino flavours can partecipate, in the CC case only electron neutrinos can be involved in the interaction (Fig. 1.2). This generates a dependency of the effect on the neutrino flavour. The effect, named Mikheyev-Smirnov-Wolfenstein (MSW) effect [5], can be described by two different effective potential for the CC and NC case:

$$V_{CC} = \pm\sqrt{2}G_F n_e, \quad V_{NC} = \mp\frac{\sqrt{2}}{2}G_F n_n; \tag{1.21}$$

where G_F is the Fermi constant, n_e and n_n are respectively the electron and neutron density of the medium. The two signs of each effective potential, stand for the neutrino and antineutrino case. V_{CC} in the case of ν_μ and ν_τ is zero since matter does not contain the corresponding charged leptons. Neutrino oscillation in matter also depend on matter density. Only the case of constant matter density is treated in the following description. In the simplest case of just two neutrino flavours, the transition probability in matter is:

$$P_M(\nu_e \rightarrow \nu_\nu) = \sin^2 2\theta^M \cdot \sin^2\left(\frac{\Delta m_M^2 2L}{E}\right), \tag{1.22}$$

9

which has the same form of Eq. 1.14 but with the effective values in matter of $\sin^2 2\theta^M$ and Δm^2_M defined as:

$$\sin^2 2\theta^M \equiv \frac{\sin^2 2\theta_{12}}{\sin^2 2\theta_{12} + (\cos 2\theta_{12} - A)^2}$$

$$\Delta m^2_M \equiv \Delta m^2 \sqrt{\sin^2 2\theta + (\cos 2\theta - A)^2} \qquad (1.23)$$

$$A \equiv \frac{2\sqrt{2} G_F N_e E}{\Delta m^2}.$$

Considering Eq. 1.22 and 1.23, the phenomenon presents a resonance if $\cos 2\theta \simeq A$. This corresponds to a large enhancement of oscillation probability even for small mixing angles.

An interesting case to describe is the one of accelerator neutrino experiment. A neutrino beam, mainly of ν_μ type produced at the source, is measured at the detector after the propagation through matter. The appearance probability for ν_e at the detector is:

$$
\begin{aligned}
P(\nu_\mu \to \nu_e) \simeq\ & \sin^2\theta_{23} \sin^2 2\theta_{13} \frac{\sin^2(\Delta_{31} - aL)}{(\Delta_{31} - aL)^2} \Delta_{31}^2 \\
& + \sin 2\theta_{23} \sin 2\theta_{13} \frac{\sin(\Delta_{31} - aL)}{\Delta_{31} - aL} \Delta_{31} \frac{\sin(aL)}{aL} \Delta_{21} \cos(\Delta_{31} \pm \delta_{CP}) \\
& + \cos^2\theta_{23} \sin^2\theta_{12} \frac{\sin^2(aL)}{(aL)^2} \Delta_{21}^2
\end{aligned}
$$

$$(1.24)$$

with:

$$\Delta ij = \Delta_{ij}^2 \frac{L}{4E_\nu}$$

$$a = \pm \frac{G_F N_e}{\sqrt{2}}. \qquad (1.25)$$

In the case of neutrino, a and δ_{CP} are positive while in the antineutrino case they are negative. Eq. 1.24 shows how both the parameters play a role in the neutrino-antineutrino asymmetry in oscillations through matter.

1.3.1 Neutrino oscillations experiments and results

Many experiments have investigated the field of neutrino oscillation since the phenomenon was theorized. They are divided mainly into two categories: *appearance* experiments and *disappearance* ones. The first investigate the probability,

for a given neutrino flavour at the source, to change flavour after having travelled through a distance L. The second ones, measure the probability for a given neutrino flavour produced at the source to survive after a distance L and thus a decrease in the neutrino flux for that flavour. Neutrino oscillations experiments can be classified based on the neutrino source studied. The neutrino source energy and the propagation distance determine the sensitivity of the experiment to the oscillation parameters. In Tab. 1.2 are reported different typology of experiments along with the parameter to which they are sensitive:

neutrino source	ν type	parameter	L (m)	E (MeV)
sun	ν_e	$\sin^2\theta_{12}, \Delta m^2_{21}$	10^{10}	1
atmosphere	$\nu_\mu, \nu_e\ (\overline{\nu}_\mu, \overline{\nu}_e)$	$\sin^2\theta_{23}, \Delta m^2_{31}$	10^4-10^7	10^2-10^5
reactor	$\overline{\nu}_e$	θ_{13}	(SBL) 10-10^3 (LBL) 10^4-10^5	1
accelerator	$\nu_\mu, (\overline{\nu}_\mu)$	$\sin^2\theta_{23}, \Delta m^2_{31}, \theta_{13}$	(SBL) 10^2 (LBL) 10^5-10^6	10^3-10^4 10^3-10^4

Table 1.2: Different typologies of neutrino oscillations experiments along with: the correspondent investigated oscillation parameters, observed ν type and characteristic values of L and E.

Solar neutrino experiments

These experiments study electron neutrinos produced by solar fusion reactions. Two different processes generate ν_e from the Sun: the pp chain and the CNO cycle (Fig. 1.3). The flux spectrum of the different reactions is shown in Fig. 1.4, with the main neutrino energy equal to $\langle E_\nu \rangle \simeq 0.42$ MeV. The theory which describes the solar neutrino flux on Earth is the Solar Standard Model (SSM). According to it, the expected ν_e flux to reach the Earth is: $\Phi_{\nu_e} = 6 \times 10^{10} \text{cm}^{-2}\text{s}^{-1}$ [6].

The first experiment that detected solar neutrinos was designed by R. Davis in Homestake, South Dakota. It measured the flux of neutrinos coming from the Sun by exploiting their interactions with a target of ^{37}Cl. The detector was located underground and observed the absorption of ν_e by the medium through CC interaction:

$$\nu_e + ^{37}\text{Cl} \rightarrow ^{37}\text{Ar} + e^- \quad (E_{th} = 814 \text{ keV}); \tag{1.26}$$
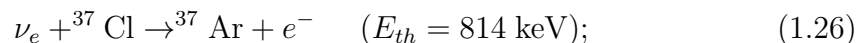
By measuring the decay of the produced radioactive ^{37}Ar nuclei, it was possible to reconstruct the number of interacting neutrinos. The results obtained showed
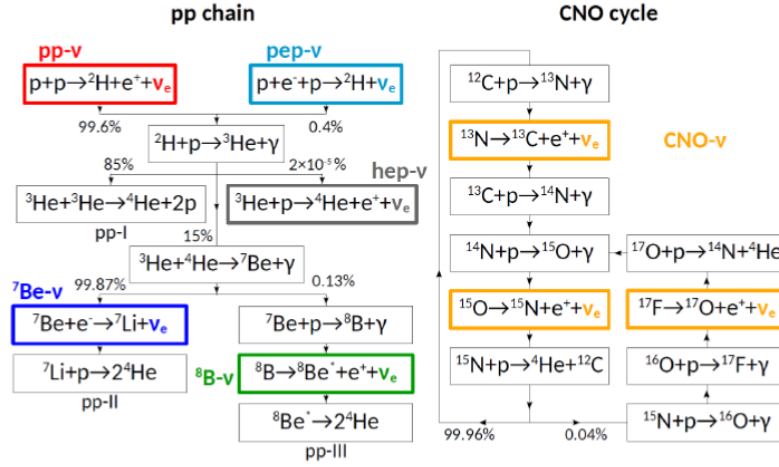
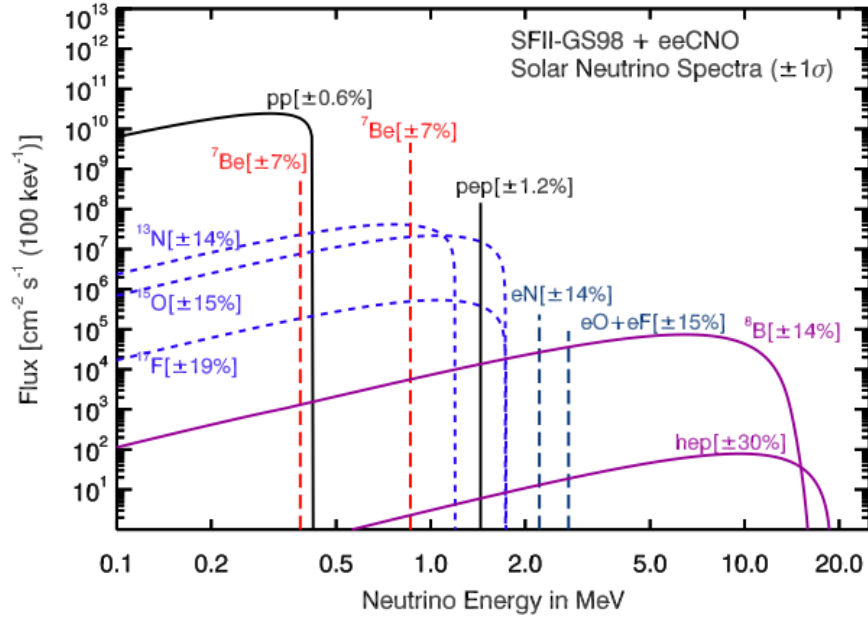Figure 1.3: Processes generating electron neutrinos from solar fusion reactions.

Figure 1.4: Energy spectrum of solar neutrinos arriving on Earth along with standard solar model uncertainties. The solid lines refer to neutrinos from the *pp* chain while dashed lines represent those from the CNO cycle.[7]

a deficit in the measured neutrino flux compared to the one predicted by the SSM [8] giving origin to the so called "solar neutrino problem".

Two experiments dedicated to the study of solar neutrinos were GALLEX/GNO (at Gran Sasso, Italy) and SAGE (Baksan, Russia). They used the same detection technique but using gallium as target for the neutrino interaction:

$$\nu_e + {}^{71}\text{Ga} \to {}^{71}\text{Ge} + e^- \qquad (E_{th} = 233 \text{ keV}); \qquad (1.27)$$
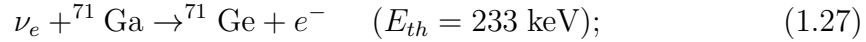
Both of them measured a reduction in the solar neutrino flux, giving another evidence of a disagreement between experimental results and theoretical models.

Other experiments used a different approach in the detection of ν_e coming from the Sun. By exploiting the Cherenkov light produced by a neutrino interacting with water, it is possible to perform not only a solar flux measurement, but also to verify the solar origin of the neutrinos by effectively separating them from the background events. The directionality of the emitted photons allows a pattern recognition for the interactions that happen in the medium. The technique is then sensitive to the three neutrino flavours. The Kamiokande experiment in Japan, was a 2.14 kt water Cherenkov detector designed to study solar neutrinos exploiting the process above described. It measured [9], along with its successor Super-Kamiokande [10], a deficit of $\sim 1/2$ in the expected neutrino flux in agreement with the previous evidences.

A decisive contribution was the one played by the SNO (Sudbury Neutrino Observatory) experiment, in Canada. Located underground, it used a 1 kt of heavy water target to detect Cherenkov light produced by charged particles, surrounded by a veto of 1.5 kt of normal water. SNO was not only sensitive to the elastic scattering as the previous experiment, but also to the CC and NC interactions:

$$
\begin{array}{lll}
\text{Electron scattering:} & \nu_x + e^- \to \nu_x + e^- \ ; & \\
\text{Charged Current:} & \nu_e + p \to e^- + n \ ; & (1.28) \\
\text{Neutral Current:} & \nu_x + d \to \nu_x + p + n & (\nu_x = \nu_{e,\mu,\tau}).
\end{array}
$$

Charged Current interaction allow to measure the flux $\Phi_{\nu_e} = \Phi_{CC}$. Neutral Current interaction produce a proton which can be capture emitting a photon. Through the observation of this photon it was possible to measure the total flux $\Phi_{\nu_e + \nu_\mu + \nu_\tau} = \Phi_{NC}$. This sensitivity to all the three flavours, allowed to measure the decrease in the flux of a particular flavour, compared to the total expected flux. SNO indeed measured a ratio Φ_{CC}/Φ_{NC} of $\sim 1/3$. While the total neutrino flux was in agreement with the one predicted by the SSM, the electron neutrino flux showed a deficit, giving proof of a flavour transition in the solar neutrino flux. This proved that neutrinos can oscillate while traveling from the Sun to the Earth.

An important contribution in solving the solar neutrino problem came also from the KamLAND experiment [11]. The Kamioka Liquid Scintillator Anti-Neutrino

13

Detector (KamLAND), is composed of a primary volume of 1 kt of ultra-pure liquid scintillator which provides the interaction target. The detector is located underground at a depth of ~ 2700 m water-equivalent, able to detect $\overline{\nu}_e$ produced by nuclear reactor, through inverse beta decay. The particular energy of reactor antineutrinos and the average baseline of ~ 180 km, allowed the measurements of Δm_{21} and θ_{12} which can be then combined with data coming from solar neutrino experiment (Fig. 1.5).
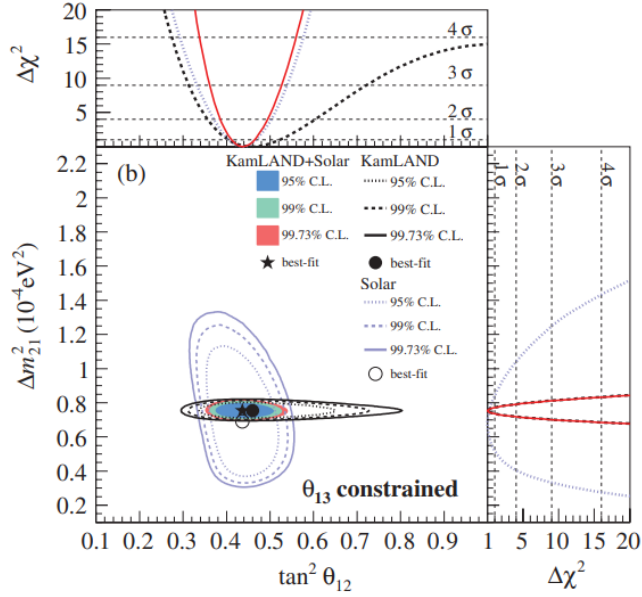

Figure 1.5: Allowed neutrino oscillation parameters regions from KamLAND. The analysis allowed a precise determination of the oscillation parameters and also place constraints on the θ_{13} parameter.

Lastly, an experiment to mention in the study of neutrinos in the solar sector is Borexino [12]. Borexino is an ultra-pure liquid scintillator detector located at the LNGS , at a depth of 3800 meters water equivalent. It is the radio-purest large-scale neutrino experiment ever built, able to investigate low energy neutrino physics with a high signal-to-noise ratio. It is sensitive to solar neutrinos via neutrino–electron elastic scattering. It was able to measure: the interaction rate for solar neutrino from ^{7}Be, solar neutrinos flux from *pep* and *pp* and the interaction rate for solar neutrinos from ^{8}Be with low energy threshold. Borexino has provided also the first experimental evidence at 5σ significance of neutrinos produced in the CNO fusion cycle in the Sun [13].

Atmospheric neutrino experiments

Cosmic Rays (CR) interacting with nucleons in the upper atmosphere, produce hadronic showers containing also pions and kaons. While travelling through the atmosphere, they can decay before reaching the Earth surface ($\pi^+ \to \mu^+ \nu_\mu$, $K^+ \to \mu^+ \nu_\mu$ and then $\mu^+ \to e^+ \nu_e \overline{\nu}_\mu$), creating neutrinos and antineutrinos (Fig. 1.6). The ratio $R_{\mu/e} = (\nu_\mu + \overline{\nu}_\mu)/(\nu_e + \overline{\nu}_e)$ is expected to be ~ 2. Atmospheric neutrinos can be classified as: *downgoing* and *upgoing*, basing on their arrival direction respect to the detection site (Fig. 1.6). In the first case they arrive above the observation point traveling a distance of 10-20 km in the atmosphere, while in the second case they come from the opposite direction traveling through the Earth for $\sim 10^4$ km. Given the fact that earth absorption in the GeV energy range is negligible, the neutrino flux should be the same in both the two cases assuming isotropic properties and no oscillation.
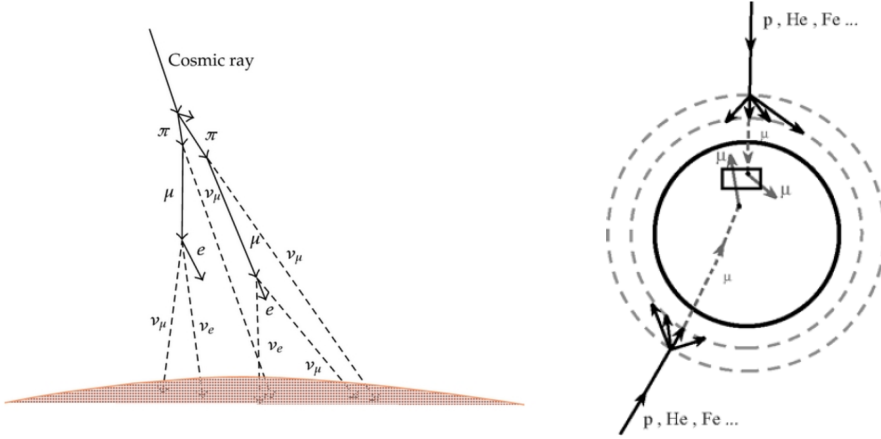

Figure 1.6: Cosmic Rays (CR) interacting with the upper atmosphere generating neutrinos of electron and muon type (right). Arrival direction to the observation point of *upgoing* and *downgoing* neutrinos produced by CR (left).

Atmospheric neutrinos experiments are sensitive to $\Delta m^2_{31(32)}$ and $\sin^2 2\theta_{31(32)}$. Among the many detectors designed to investigate this sector, there are the water Cherenkov detectors: Kamiokande, Super-Kamiokande and IMB. All of them measured a discrepancy between the measured and expected ratio R. They initially reported a deficit in the $(\nu_\mu + \overline{\nu}_\mu)$ flux. Later Super-Kamiokande, being able to measure neutrino fluxes as functions of the zenith angle (θ), showed a decrease for the *upgoing* ν_μ flux ($\cos\theta < 0$) respect to the predicted one with no oscillation. This was a proof of a strong disappearance for *upgoing* neutrinos dependent on the zenith angle and thus on the travel distance, pointing to neutrino oscillations from the initial flavour to another. The first results from Super-Kamiokande

provided an estimation of the atmospheric parameters as $\sin^2 \theta > 0.82$ and $5 \times 10^{-4} < \Delta m^2 < 6 \times 10^{-3}$ eV^2 at 90% of confidence level (Fig. 1.7) [14]. These parameters, in the two flavour scenario where $\nu_\mu \to \nu_\tau$, corresponds to $\theta = \theta_{23}$ and $\Delta m^2 = \Delta m_{31}^2$. The atmospheric neutrino oscillation parameters obtained from the most recent results are reported in [15].
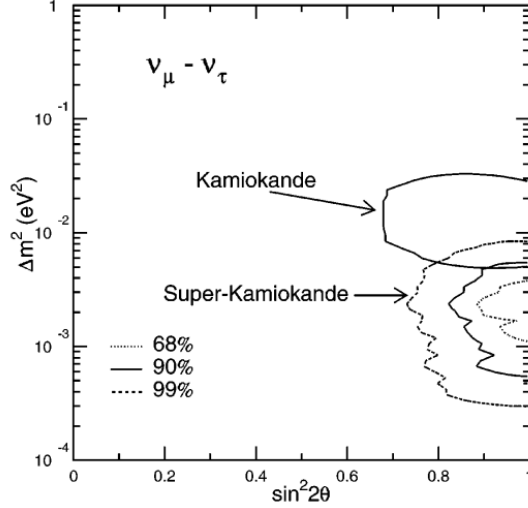

Figure 1.7: Regions for different confidence intervals for $\sin^2 \theta$ and Δm^2 in the case of two neutrino oscillations ($\nu_\mu \to \nu_\tau$) obtained from the first results of Super-Kamiokande. The Kamiokande 90% confidence interval is also reported as comparison.

Nuclear reactor neutrino experiments

Fission processes happening inside nuclear reactors generate products which can decay through β^- decay, creating electron antineutrinos. This flux of $\overline{\nu}_e$ coming from the nuclear reactors can be studied to investigate the field of neutrino oscillations. However, due to the low antineutrino energy $E_{\overline{\nu}}$ correspondent to few MeV, it is not possible to observe the appearance of $\overline{\nu}_\tau$ and $\overline{\nu}_\mu$. The energy threshold to produce the correspondent leptons is indeed too high for the process. For this reason experiment exploiting nuclear reactor neutrinos sources are of *disappearance* type. The observation technique is to observe inverse β decay processes initiated by $\overline{\nu}_e$ and compare the measured rate of the produced positrons with the expected one. The signature is the coincidence of a prompt positron and a delayed neutron emitting photons during its capture. Liquid scintillator doped with Gadolinium are typically used to increase the neutron capture cross-section and the energy of the γ released.

Experiments studying nuclear reactor neutrinos were Chooz and Palo Verde. Due to their baseline distance between 1 and 2 km, they are both classified as short-baseline experiments. This, along with the average neutrino energy of ~ 4 MeV, allowed a direct measurement of $\sin^2 \theta_{13}$. The Chooz experiments set an upper limit of $\sin^2 2\theta_{13} <0.1$ at 90% of CL.

Later, the determination of θ_{13} was possible thanks to a new generation of nuclear reactors experiments: Double Chooz (France) [16], RENO (South Korea) [17] and Daya Bay (China) [18]. All of them reported the disappearance of $\overline{\nu}_e$ and precisely measured θ_{13}. Among them, the most decisive contribution came from Daya Bay, with $\sin^2 2\theta_{13} =0.00841 \pm 0.0027(\text{stat}) \pm 0.0019(\text{syst})$ with a data taking of 1230 days [19].

A long-baseline experiment which studied reactor neutrinos was KamLAND. It has determined a precise value for the neutrino oscillation parameter Δm_{21}^2 and stringent constrains on θ_{12}. Located underground in the old Kamiokande's site in Japan, it was surrounded by 55 nuclear power reactor units. Electron anti-neutrinos were detected via inverse β-decay ($\overline{\nu}_e + p \rightarrow e^+ + n$) with a 1.8 MeV threshold. The analysis conducted on KamLAND data combining them with solar neutrino data, gave as results for the oscillation parameters $\Delta m_{21} = 7.59^{+0.21}_{-0.21} \times 10^{-5}$ eV^2 and $\tan^2\theta_{12} = 0.47^{+0.06}_{-0.05}$ [20].

Accelerator neutrino experiments

A beam of neutrinos can be produced by accelerated high energy protons into a nuclear target. The produced secondary particles, mostly kaons and pions, can decay into neutrinos or antineutrinos. Given the composition of the decaying particles, the most abundat flavour for the beam is ν_μ and $\overline{\nu}_\mu$ ($\pi^+, K^+ \rightarrow \mu^+ + \nu_\mu$ and $\pi^-, K^- \rightarrow \mu^- + \overline{\nu}_\mu$), with a contamination of ν_e and $\overline{\nu}_e$ coming from the muon decay ($\mu^+ \rightarrow e^+ + \overline{\nu}_\mu + \nu_e$ and $\mu^- \rightarrow e^- + \nu_\mu + \overline{\nu}_e$). The primary proton beam can be varied in energy and intensity in order to control features of the neutrino beam. Furthermore by tuning the distance between source and detector it is possible to make more effective the study of specific desired neutrino oscillation parameters as already described in Sec. 1.3. Accelerator neutrino experiment can be thus of short-baseline (SBL) or long-baseline (LBL) type. Among them, many have a dual site design. They are composed of a *near* and a *far* detector. This makes possible to compare the measured flux at the near site immediately after the neutrino source, with the one measured at the far detector after a possible flavour oscillation.

The KEK-to-Kamioka (K2K) was one of the first long baseline accelerator neutrino experiment to be build. The KEK- Proton Synchrotron produced a beam of muon neutrinos with a mean energy of about 1.3 GeV towards the Super-Kamiokande detector at a distance of L=250 km. The experiment had a dual site

design with a near detector located at 300 m from the beam source. K2K was able to confirm the ν_μ disappearance in the same region studied by atmospheric neutrinos [21].

MINOS (the Main Injector Neutrino Oscillation Search) gave another important contribution studying the oscillation parameters both in disappearance and appearance mode. It exploited a beam of muon neutrinos with $E_\nu \sim 3\text{GeV}$ produced by the NuMI (Neutrinos at the Main Injector) facility present at the Fermi National Accelearator Laboratory (FNAL). The beam was directed towards a far detector located underground in the Soudan Mine at a distance of 735 km. MINOS, along with its successor MINOS+, confirmed the ν_μ disappearance setting new limits and constraints [22].

OPERA was designed as a long baseline accelerator experiment, to prove the ν_τ appearance in a high energy muon neutrino beam ($E_{\nu_\mu} \sim 17$ GeV). The ν_μ beam was produced at CERN towards the detector at the Gran Sasso Laboratory, travelling a distance of 732 km. The energy threshold to produce the τ lepton in charged current interactions is $\langle E_\nu \rangle \sim 3.5$ GeV. The observation of 10 events of ν_τ appearance confirmed the $\nu_\mu \rightarrow \nu_\tau$ oscillation with a significance larger than 5σ [23].

The T2K (Tokai to Kamioka) experiment was the first to measure the ν_e appearance, giving proof of the $\nu_\mu \rightarrow \nu_e$ oscillation. With its particularly design, the detector was placed with a 2.5° off-axis angle respect to the neutrino beam. This allowed to have a narrow energy spectrum, setting the maximum of the neutrino energy beam at 0.6 GeV. In this way it was possible to study the first maximum of oscillation at the defined baseline of 295 km [24].

Another off-axis experiment is NOνA. It was designed with a near and a far detector, both placed 14.5 mrad off-axis of a neutrino beam with mean energy ~ 2 GeV and a flight distance of 810 km. It was dedicated to study the ν_μ disappearance, but it was also the first one to observe the $\overline{\nu}_e$ appearance in a $\overline{\nu}_\mu$ beam [25].

Among the new future experiments studying neutrino oscillations, there is the Deep Underground Neutrino Experiment (DUNE). It will be a long-baseline accelerator neutrino experiment, with a dual site design.

1.4 Neutrino Mass Ordering and CP violation

Through neutrino oscillation experiment it is possible only to measure the mass squared difference Δm_{ij}^2 but not the individual mass value. While the sign for Δm_{21}^2 has been defined from data of solar neutrino experiments, the sign of Δm_{31}^2 is still unknown. In the three flavour framework, two different scenarios in the neutrino mass ordering arise from this. Depending on the sign of Δm_{31}^2 one can

Experiment	L (km)	E$_\nu$ (GeV)
K2K	250	1.3
MINOS	735	3
MINOS+	735	7
OPERA	730	17
T2K	295	0.6
NovA	810	2
DUNE	1300	2-3

Table 1.3: Summary of the main long-baseline accelerator neutrino experiments, with their characteristic travel distance and mean neutrino beam energy.

have:

- **Normal Ordering (NO)**

$$m_1 < m_2 < m_3, \quad \Delta m_{31}^2 = \Delta m_{atm}^2 > 0, \quad \Delta m_{21}^2 = \Delta m_\odot^2 > 0; \qquad (1.29)$$

- **Inverted Ordering (IO)**

$$m_3 < m_1 < m_2, \quad \Delta m_{32}^2 = \Delta m_{atm}^2 < 0, \quad \Delta m_{21}^2 = \Delta m_\odot^2 > 0. \qquad (1.30)$$

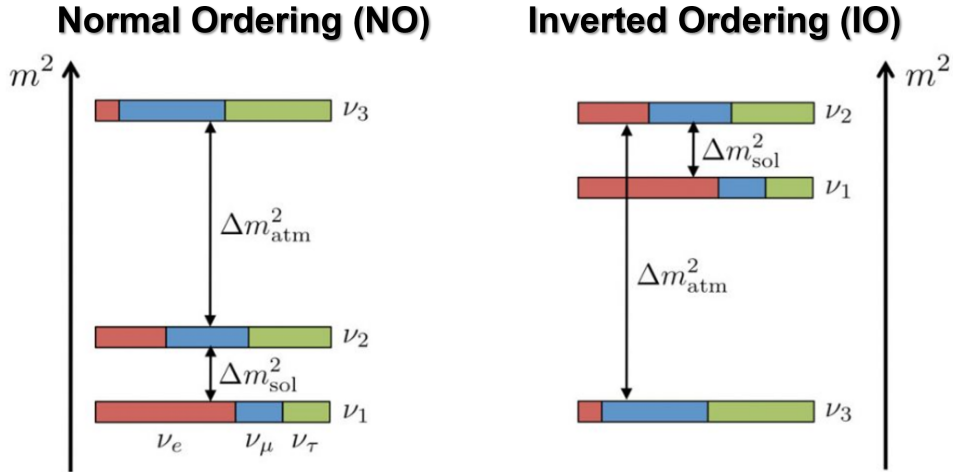The two situations are schematically represented in Fig. 1.8.

Figure 1.8: Schematic representation of the two possible mass ordering scenarios in the case of three active neutrinos. The flavour content in each mass eigenstate with the different colours.

19

Goal of the next generation of neutrino experiments will be to unveil the correct ordering in order to better understand the flavour physics. Until now, thanks also to cosmological studies, it has been possible to set an upper limit for the sum of the neutrino masses:

$$\sum_j m_j < 0.26 \text{ eV}, \quad 95\% \text{ CL}. \tag{1.31}$$

A possible CP violation in the leptonic sector would be of great interest to be observed. While CP violation has been already proved in quark sector, it has not yet observed in leptons. In the formalism of neutrino oscillation, CPV phases term are present in the parametrization of the mixing matrix U_{PMNS}. In the three flavour mixing scenario, a value of $\delta_{CP} \neq 0, \pi$ would represent a CP violation. It would also manifest itself as a difference in the oscillation probability for neutrinos and antineutrinos $P(\nu_\alpha - \nu_\beta) \neq P(\overline{\nu}_\alpha - \overline{\nu}_\beta)$. This difference can be studied as the CP asymmetry:

$$\mathcal{A}_{CP} = \frac{P(\nu_\alpha \to \nu_\beta) - P(\overline{\nu}_\alpha \to \overline{\nu}_\beta)}{P(\nu_\alpha \to \nu_\beta) + P(\overline{\nu}_\alpha \to \overline{\nu}_\beta)} \tag{1.32}$$

Another asymmetry is also introduced by the matter effect described in Sec. 1.3 by Eq. 1.24, where the a term has different sign for neutrinos and antineutrinos. This, as already mentioned, is mainly due to the presence of only electrons and absence of positrons in the Earth. In this field of research, T2K has been the first experiment to put significant constrains on the CP violation phase both for NO and IO [26].

1.5 Updated global analysis of three flavor neutrino oscillations

A global analysis has been performed on the data obtained from the different experiments. A summary of the global fits obtained is reported in Fig. 1.10 [27]. The results determine the ranges of allowed values for the six relevant parameters in the flavour oscillation phenomenon, for both NO and IO (Fig. 1.9).

1.5.1 Future prospects

Even thought important results have been obtained in the field of neutrino physics, there are still some open questions to be solved. The remaining questions yet to be answered are:

- the determination of the sign of Δm_{31}^2 which would assess the neutrino mass ordering;

- the measurement of a possible CP violation in the leptonic sector;

- the determination of the neutrino nature whether a Majoran or Dirac particle.

Related to this scenario, in the long-baseline field the Deep Underground Experiment (DUNE) will play a significant role in determining the neutrino mass ordering and measuring of the δ_{CP} violating phase. This will be mainly possible thanks to the characteristic baseline of the experiment ($\sim$1300 km), which will give access to observe the MSW effect, and to a neutrino beam capable of producing both neutrinos and antineutrinos.
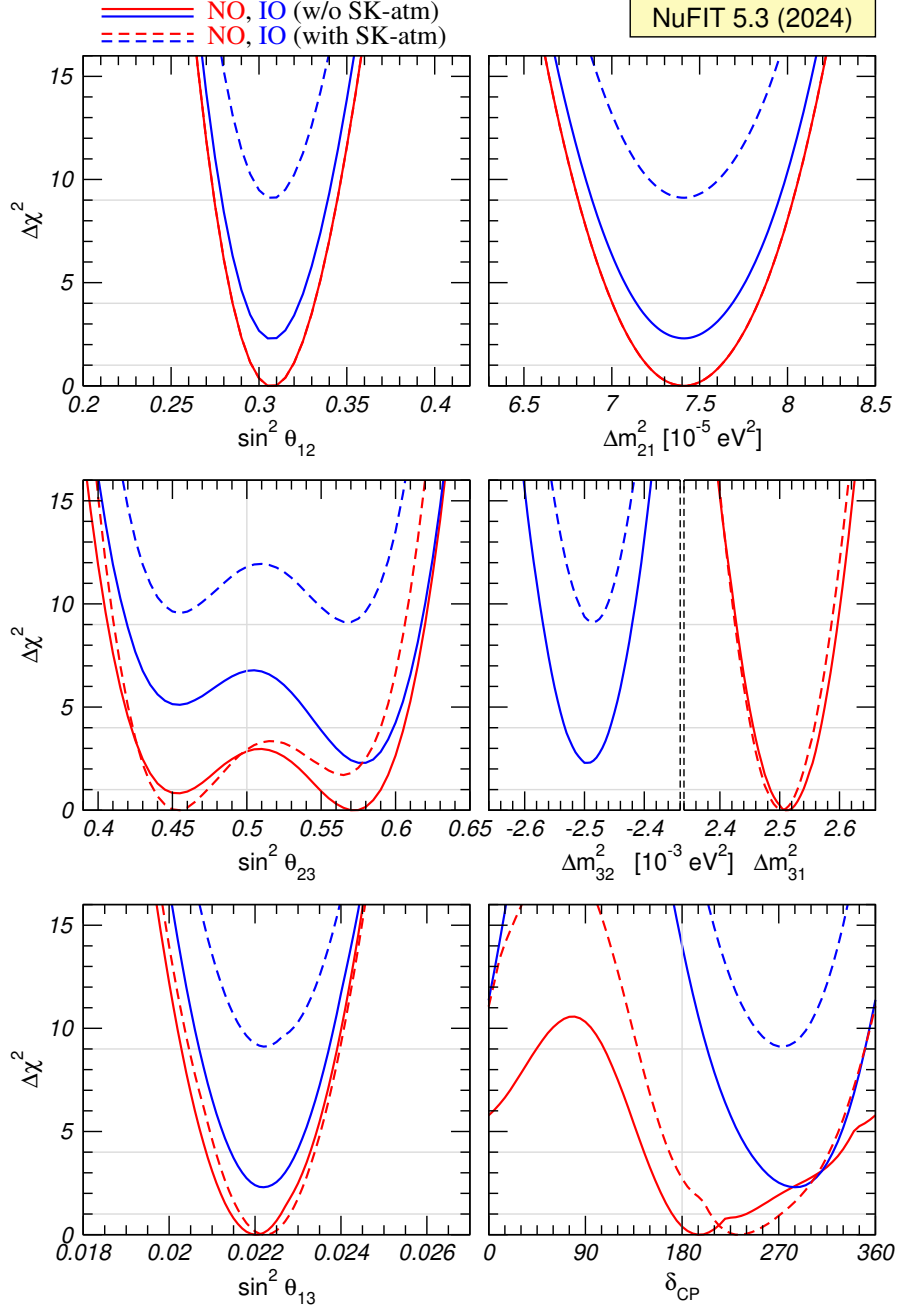
Figure 1.9: Global 3ν oscillation analysis. The red (blue) curves correspond to Normal (Inverted) Ordering. Solid (dashed) curves are without (with) adding the tabulated SK-atm $\Delta\chi^2$. In the second column second row plot, as atmospheric mass-squared splitting it has been used Δm^2_{31} for NO and Δm^2_{32} for IO.

		Normal Ordering (best fit)		Inverted Ordering ($\Delta\chi^2 = 2.3$)	
		bfp $\pm 1\sigma$	3σ range	bfp $\pm 1\sigma$	3σ range
without SK atmospheric data	$\sin^2\theta_{12}$	$0.307^{+0.012}_{-0.011}$	$0.275 \to 0.344$	$0.307^{+0.012}_{-0.011}$	$0.275 \to 0.344$
	$\theta_{12}/°$	$33.66^{+0.73}_{-0.70}$	$31.60 \to 35.94$	$33.67^{+0.73}_{-0.71}$	$31.61 \to 35.94$
	$\sin^2\theta_{23}$	$0.572^{+0.018}_{-0.023}$	$0.407 \to 0.620$	$0.578^{+0.016}_{-0.021}$	$0.412 \to 0.623$
	$\theta_{23}/°$	$49.1^{+1.0}_{-1.3}$	$39.6 \to 51.9$	$49.5^{+0.9}_{-1.2}$	$39.9 \to 52.1$
	$\sin^2\theta_{13}$	$0.02203^{+0.00056}_{-0.00058}$	$0.02029 \to 0.02391$	$0.02219^{+0.00059}_{-0.00057}$	$0.02047 \to 0.02396$
	$\theta_{13}/°$	$8.54^{+0.11}_{-0.11}$	$8.19 \to 8.89$	$8.57^{+0.11}_{-0.11}$	$8.23 \to 8.90$
	$\delta_{\mathrm{CP}}/°$	197^{+41}_{-25}	$108 \to 404$	286^{+27}_{-32}	$192 \to 360$
	$\dfrac{\Delta m^2_{21}}{10^{-5}\ \mathrm{eV}^2}$	$7.41^{+0.21}_{-0.20}$	$6.81 \to 8.03$	$7.41^{+0.21}_{-0.20}$	$6.81 \to 8.03$
	$\dfrac{\Delta m^2_{3\ell}}{10^{-3}\ \mathrm{eV}^2}$	$+2.511^{+0.027}_{-0.027}$	$+2.428 \to +2.597$	$-2.498^{+0.032}_{-0.024}$	$-2.581 \to -2.409$
		Normal Ordering (best fit)		Inverted Ordering ($\Delta\chi^2 = 9.1$)	
		bfp $\pm 1\sigma$	3σ range	bfp $\pm 1\sigma$	3σ range
with SK atmospheric data	$\sin^2\theta_{12}$	$0.307^{+0.012}_{-0.011}$	$0.275 \to 0.344$	$0.307^{+0.012}_{-0.011}$	$0.275 \to 0.344$
	$\theta_{12}/°$	$33.67^{+0.73}_{-0.71}$	$31.61 \to 35.94$	$33.67^{+0.73}_{-0.71}$	$31.61 \to 35.94$
	$\sin^2\theta_{23}$	$0.454^{+0.019}_{-0.016}$	$0.411 \to 0.606$	$0.568^{+0.016}_{-0.021}$	$0.412 \to 0.611$
	$\theta_{23}/°$	$42.3^{+1.1}_{-0.9}$	$39.9 \to 51.1$	$48.9^{+0.9}_{-1.2}$	$39.9 \to 51.4$
	$\sin^2\theta_{13}$	$0.02224^{+0.00056}_{-0.00057}$	$0.02047 \to 0.02397$	$0.02222^{+0.00069}_{-0.00057}$	$0.02049 \to 0.02420$
	$\theta_{13}/°$	$8.58^{+0.11}_{-0.11}$	$8.23 \to 8.91$	$8.57^{+0.13}_{-0.11}$	$8.23 \to 8.95$
	$\delta_{\mathrm{CP}}/°$	232^{+39}_{-25}	$139 \to 350$	273^{+24}_{-26}	$195 \to 342$
	$\dfrac{\Delta m^2_{21}}{10^{-5}\ \mathrm{eV}^2}$	$7.41^{+0.21}_{-0.20}$	$6.81 \to 8.03$	$7.41^{+0.21}_{-0.20}$	$6.81 \to 8.03$
	$\dfrac{\Delta m^2_{3\ell}}{10^{-3}\ \mathrm{eV}^2}$	$+2.505^{+0.024}_{-0.026}$	$+2.426 \to +2.586$	$-2.487^{+0.027}_{-0.024}$	$-2.566 \to -2.407$

Figure 1.10: Three-flavor oscillation parameters from fit to global data as of March 2024 for both NO and IO.

Chapter 2

The Deep Underground Neutrino Experiment

The Deep Underground Neutrino Experiment (DUNE) is an international project enabling a broad study of the three flavour neutrino physics scenario with unprecedented detail. Primary goals of DUNE will be to search for leptonic charge parity (CP) violation, determine the neutrino mass ordering and obtain precise measurement of neutrino mixing parameters. Its physics program will include also search for nucleon decay as a possible sign of a Grand Unified Theory and the observation of supernova neutrino bursts (SNBs) from supernovae [28].

2.1 DUNE design

DUNE will be a long-baseline neutrino experiment located in the U.S. . Its dual site design will consist of a Near Detector (ND) complex and a Far Detector (FD) site. The ND will be housed at Fermilab, Illinois, while the FD will be located at a distance of 1300 km, at the Sanford Underground Research Facility (SURF) in South Dakota (Fig. 2.1). The Long-Baseline Neutrino Facility (LBNF) beamline at Fermilab will provide the world's most intense neutrino beam to the Near and Far Detectors. The composite ND, placed downstream the beamline, will serve mostly to constrain systematic uncertainties. The FD will be a multi kiloton modular Liquid Argon Time Projection Chamber (LAr TPC) aimed to reconstruct neutrino interactions inside the detector volume.

The DUNE project foresees different phases of deployment both in term of the detectors and of beam power. During the so called Phase I, the fiducial mass of the FD will be of 20 kt LAr, the ND complex will have a temporary configuration and a proton beam of 1.2 MW will be used. While during Phase II, the FD fiducial mass will reach 40 kt and the proton beam will be upgraded to 2.4 MW. This will
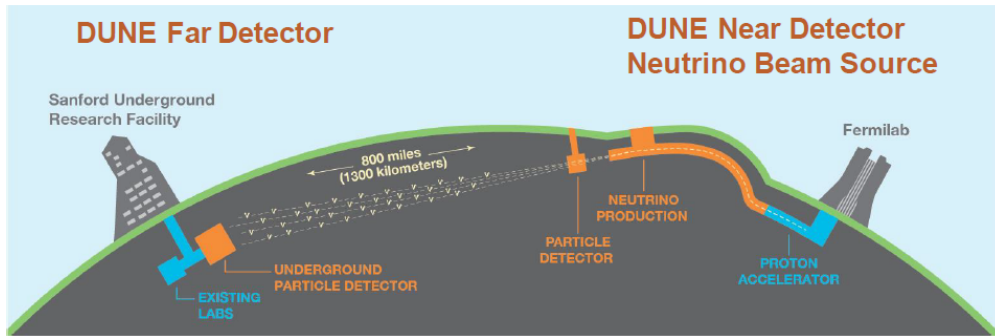
Figure 2.1: Sketch of the DUNE long-baseline design.

allow DUNE to fulfill its scientific program.

2.1.1 Neutrino beam

The neutrino beam will be provided by the LBNF at Fermilab [29] (Fig. 2.2). The Proton Improvement Plan II, or PIP-II, project is an essential upgrade to Fermilab's accelerator complex to enable the world's most intense high-energy beam of neutrinos for DUNE. Currently under construction, it will provide between 1.0 and 1.2 MW of proton beam power from the Fermilab Main Injector, exploiting a superconducting linear proton accelerator. The beam will then be aimed and focused and the protons with energy between 60 GeV and 120 GeV eventually will collide on a fixed production target [30]. A secondary beam will be then created mainly composed of pions and kaons. The hadronic shower will be focused by magnetic horns into a 194 m long pipe and left decaying mainly into $\mu^{\pm}$ and $\nu_{\mu}/\overline{\nu}_{\mu}$. By selecting the charge of the initial pions through magnetic field, the beam will run in neutrino or antineutrino mode. An absorber placed at the end of the decay pipe will stop muons although not completely, resulting in a partial contamination of the beam. The resulting ν_{μ} beam energy will be peaked at about 2.5 GeV. This will allow to cover the first and second maximum of the oscillation probability in the study of neutrino oscillations, exclusive characteristic of DUNE. Fig. 2.3 shows the expected neutrino fluxes in neutrino and antineutrino mode at the ND, while Fig. 2.4 at the FD. The flux uncertainties at the ND and FD as a function of neutrino energies for both production modes are shown in Fig. 2.5 (for on-axis and off-axis positions) and Fig. 2.6.

2.1.2 Near Detector

The Near Detector will serve as experiment's control by constraining systematic errors and mitigating their effects. This will be achieved by a high-statistics charac-
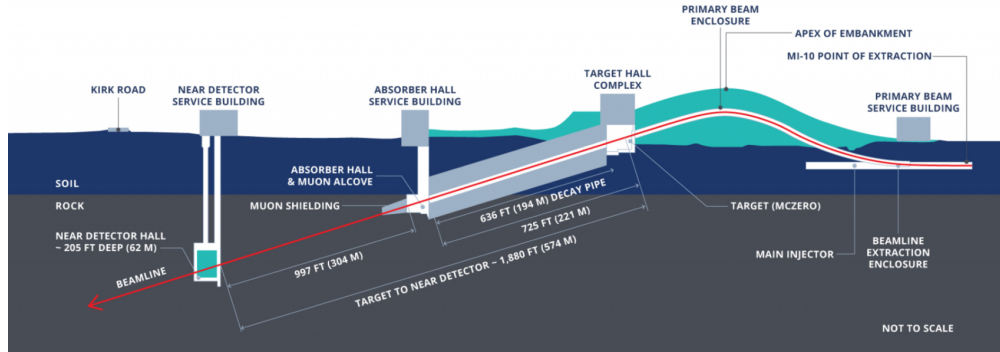
Figure 2.2: Schematic representation of the beam production at the LBNF, Fermilab.

terization of the beam. The ND will also measure the unoscillated energy spectra and the beam composition near the source. The interaction rate obtained will then be compared to the rate at the Far Detector. The precise measurement of the spectra for neutrinos and antineutrinos interactions at the ND will help in the study of the neutrino interaction model giving input on what to expect at the Far Detector.

The ND complex will be composed of different elements later described in this section. Part of them will be able to move to off-axis beam positions. This will allow the ND to provide data sets with different beam spectra. This capability will serve to study and minimizing the errors arising from the near-to-far flux difference due to the different angular acceptance.

The three primary detectors componing the Near Detector complex will be: a highly modular LAr TPC (ND-LAr), the Temporary Muon Spectrometer (TMS) which will be present in DUNE phase I, later replaced by a magnetized gaseous Argon TPC (ND-GAr) during phase II, and a large magnetized beam monitor, the System of on-Axis Neutrino Detection (SAND). The complex will be located underground at approximately 574 m from the neutrino source. SAND will be the only one to be fixed in an on-axis configuration, while the other two components will make use of rails to move off-axis to the direction of the neutrino beam (Fig. 2.8).

ND-LAr

Having a major component of LAr in the ND complex arises as a necessity in order to have the same target material as the one used in the FD modules. This will allow to reduce cross section and systematic uncertainties for oscillation analysis. Due to the intense neutrino flux and high event rate, a traditional LAr TPC would have been not appropriate as an option. To solve this, the design proposed
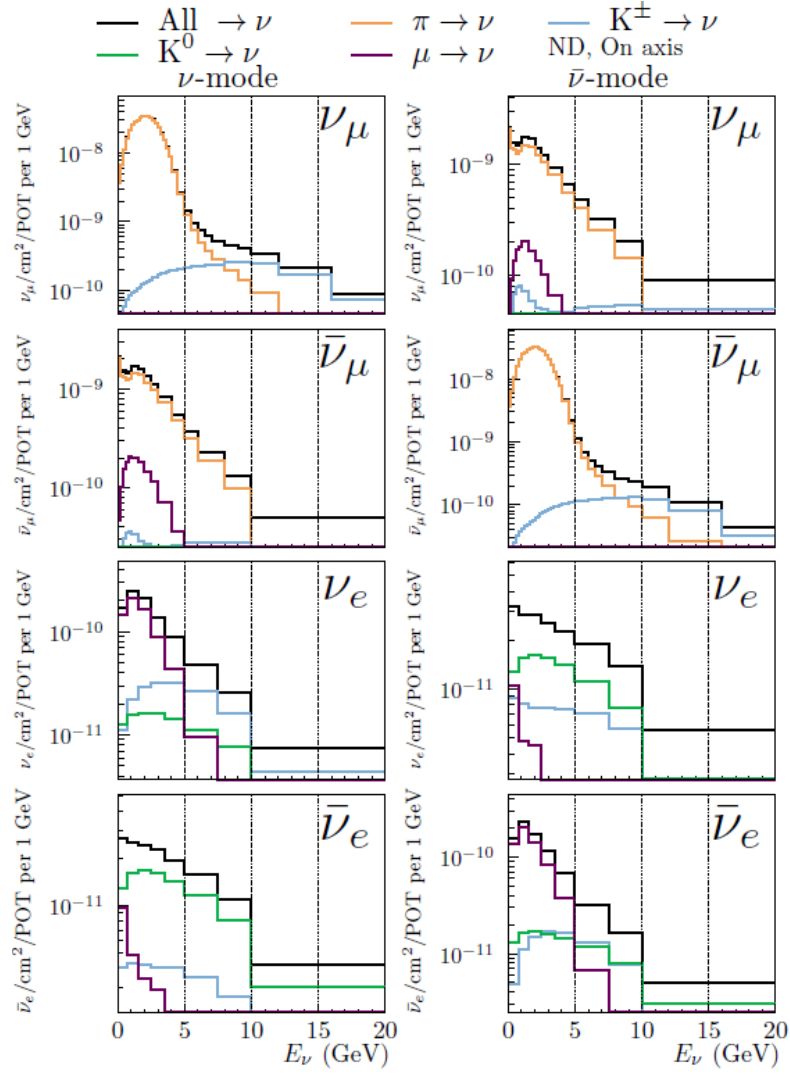
Figure 2.3: Expected neutrino fluxes at the Near Detector for neutrino (left) and antineutrino mode (right) as a function of the neutrino energy.
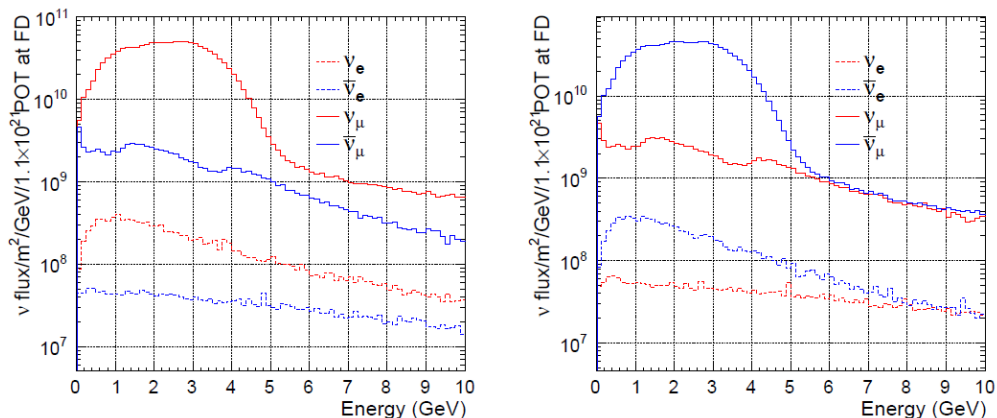
Figure 2.4: Expected neutrino fluxes composition at the Far Detector for neutrino (left) and antineutrino mode (right) as a function of the neutrino energy.

for ND-LAr is a large TPC composed as a matrix of smaller, optically isolated TPCs, with individual pixelated readout [31]. A subdivided volume means shorter drift distances and times. This configuration allows to mitigate overlapping of interactions inside the detector. The detector will be able to provide an intrinsic 3D reconstruction of tracks. ND-LAr will be composed of 5×7 individual modules, for a total active volume of 5×7×3 m^3 and a fiducial mass of 67 tons.

ND-GAr

ND-GAr will be a magnetized high pressure gaseous argon TPC (HPgTPC) surrounded by an electromagnetic calorimeter (ECAL) (Fig. 2.9). Both the detectors will be in a 0.5 T magnetic field and a muon system. The detector will measure momentum and sign of the charged particles exiting ND-LAr, extending this measurements to lower energies. It will also improve the particle identification (PID) capabilities. During Phase I ND-GAr will not be operational, but only during Phase II. As already mentioned, a Temporary Muon Spectrometer (TMS) will be initially used instead. TMS will have a simple design inspired by MINOS, consisting of interleaved planes of scintillators and magnetized steel.

ND-GAr and ND-LAr will both partecipate in the DUNE Precision Reaction - Independent Spectrum Measurement (PRISM) program, thanks to their capability of moving up to 33 m off-axis. During this time, exploiting their position, they will take data with different neutrino spectra. At an off-axis angle relative to the initial beam direction, the neutrino energy spectrum is narrower and peaked at a lower energy than the on-axis spectrum, becoming more monochromatic. The capability to modify the energy spectrum at the near site by measuring at off-axis positions is useful to diagnose beamline aberrations and further constrain flux uncertainties.
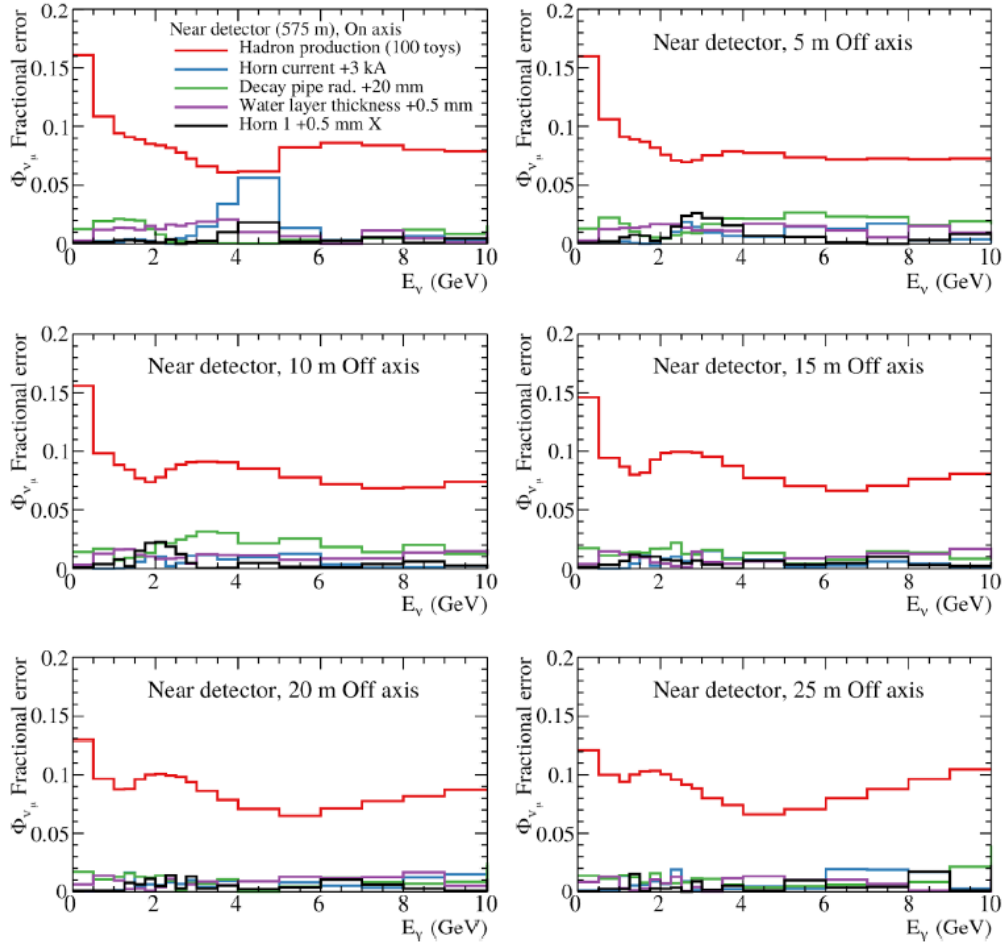
Figure 2.5: Flux uncertainties for on-axis Near Detector position (top left) and for different off-axis positions as a function of E_ν.
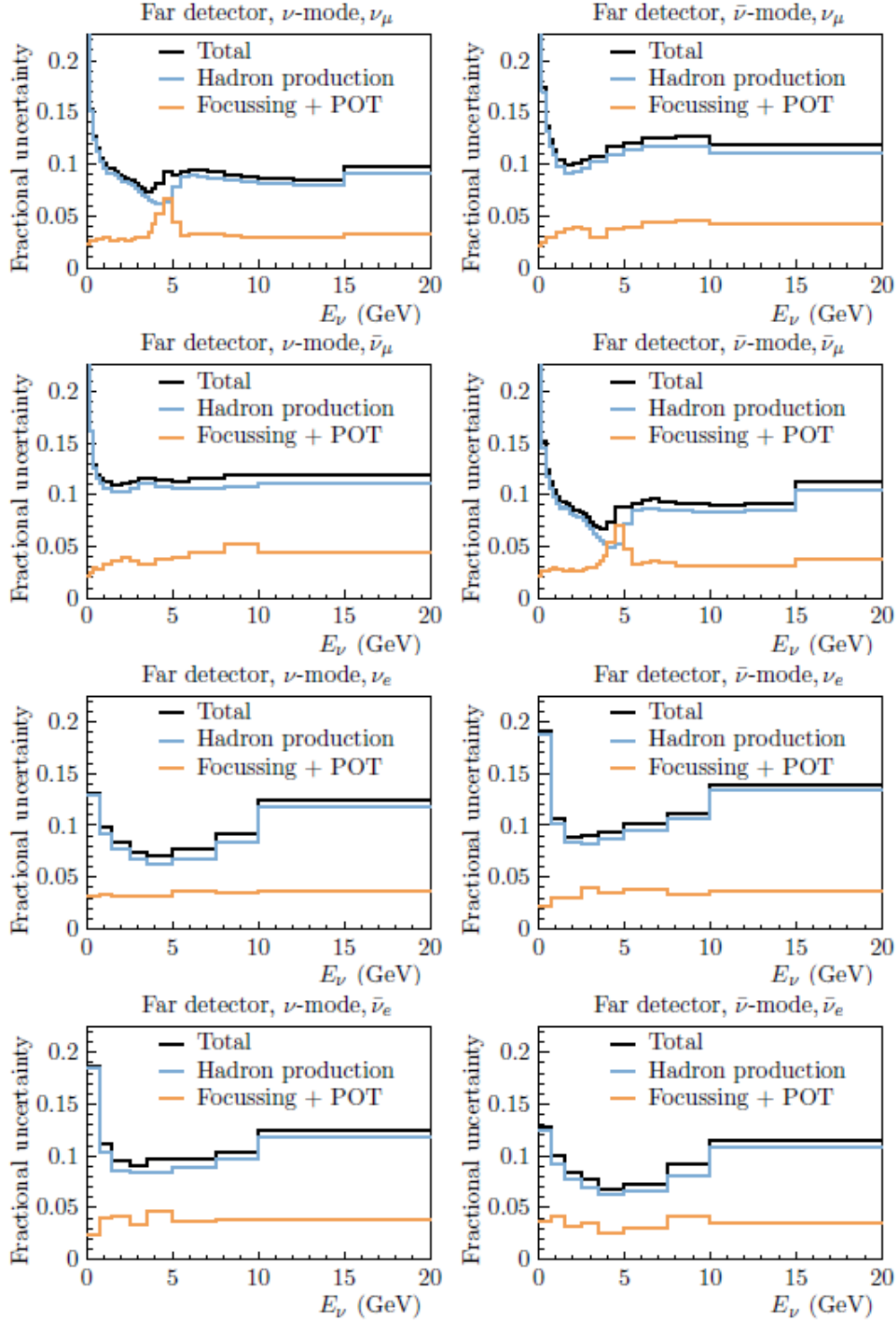
Figure 2.6: Flux uncertainties at the Far Detector as a function of the neutrino energy for both neutrino and antineutrino modes.
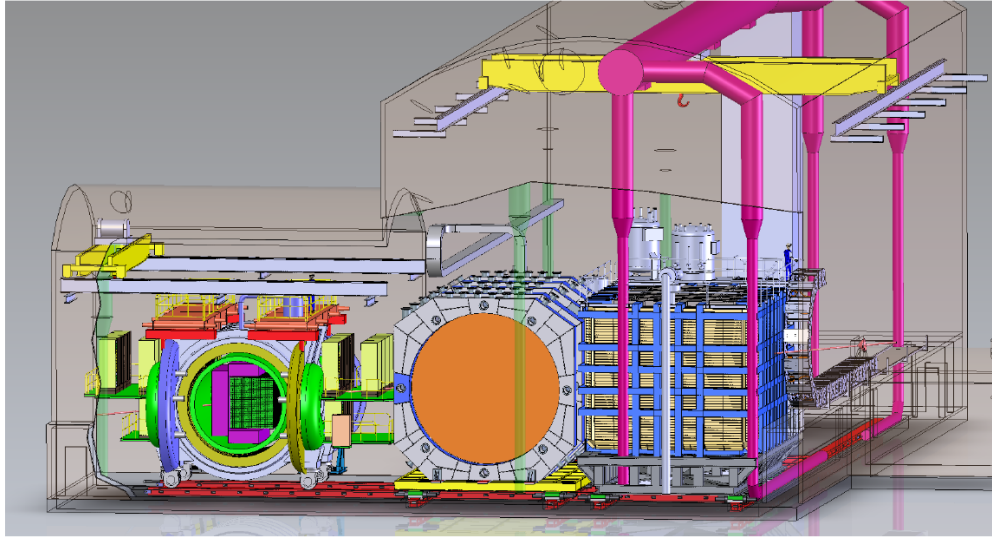
Figure 2.7: Representation of the Near Detector hall. From right to left (direction of the ν beam) are represented: ND-LAr, ND-GAr, SAND.
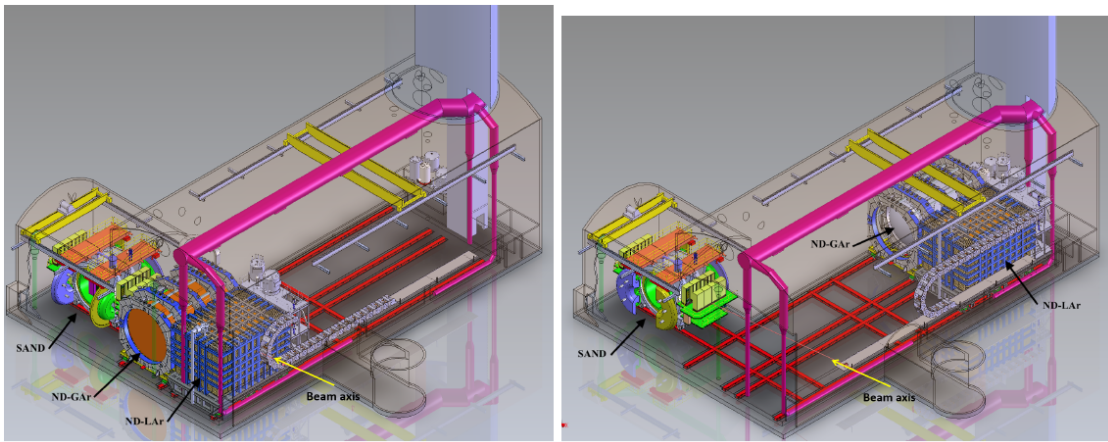

Figure 2.8: Design of the Near Detector complex. In the figure are visible the three detectors. While ND-LAr and ND-Gar will be movable off-axis (right), SAND will be the only one fixed in an on-axis position.
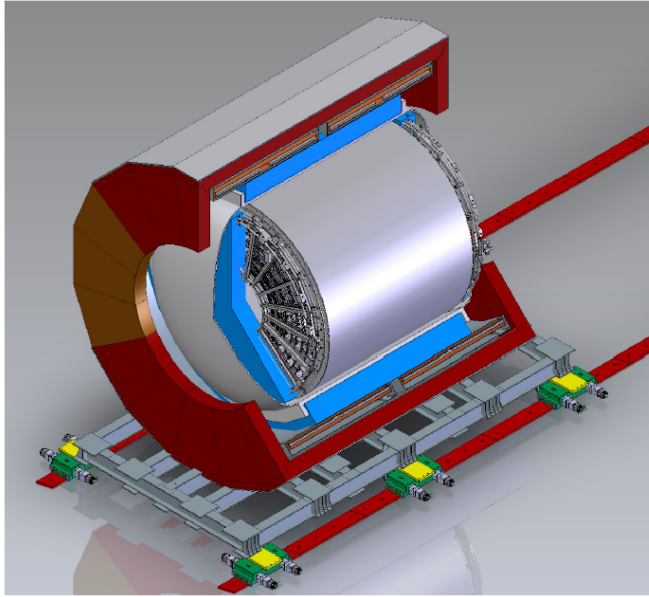
Figure 2.9: Design of ND-GAr.

SAND

The System for on-Axis Neutrino Detection (SAND) will serve as a continuous on-axis beam monitoring system. It is essential to have a detector able to quickly identify beam variation. SAND design is based on a superconducting solenoid magnet of 0.6 T and an Electromagnetic Calorimeter (ECAL), both refurbished from the KLOE experiment. The inner volume will be instrumented with an inner Straw Tube Tracker (STT) and a thin active LAr target (GRAIN) (Fig. 2.10).

Figure 2.10: Desing of SAND and its components.

Figure 2.11: Left: site of the Far Detector complex and SURF facility. Right: cryostat for the FD1 module.

2.1.3 Far Detector

The Far Detector will be composed of four independent modules of Liquid Argon TPC. During phase I, only the first two modules will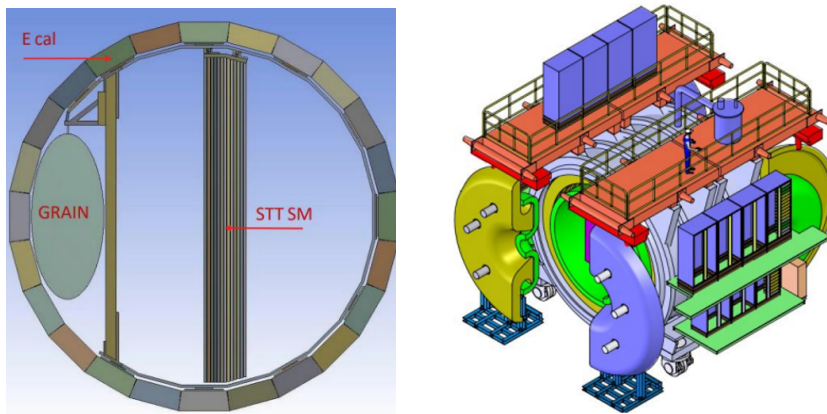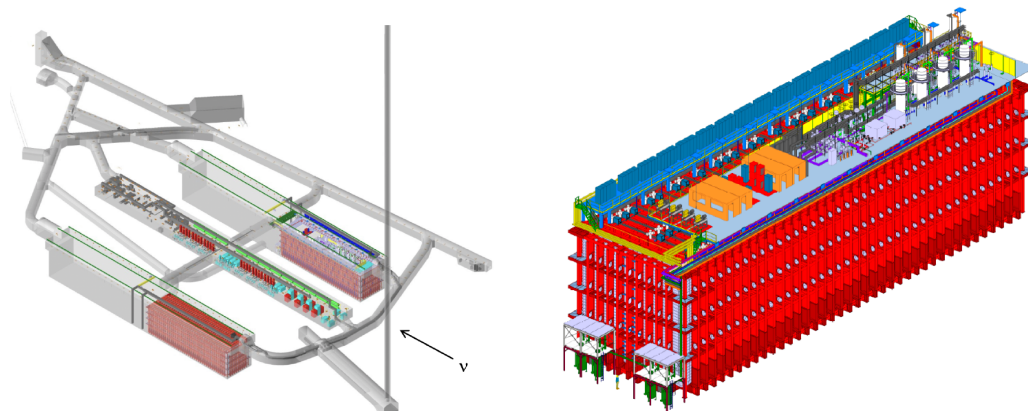 be operating, called FD1 and FD2. The remaining two, FD3 and FD4 will be present during phase II. The detectors will have an active mass of 13 kton and housed inside a membrane cryostat with passive insulation of dimensions $19 \times 18 \times 66$ m^3. The Far Detector complex will be located 1.5 km underground in the SURF cavern, in South Dakota (Fig. 2.11) [32]. The technology chosen for FD1 is the single-phase (SP) horizontal drift (HD) LAr TPC. FD2 will be again a single-phase LAr TPC but with vertical drift (VD). The design for FD3 and FD4 instead has yet to be defined.

Single-Phase Liquid Argon Time Projection Chamber (SP LAr-TPC)

Neutrinos interacting with the liquid argon volume produce ionization and scintillation light. The working principle of a Time Projection Chamber is to drift the produced ionization electrons towards an anode under the effect of a uniform electronic field. The charge of the drifted electrons is collected at the anode. It is possible to reconstruct the full topology of the neutrino interaction. Two of the three spatial coordinates (y and z) are established from the position of the collected charged. The third one is obtained by the time difference between the the arrival time of the electrons and the t_0 of the event. This latter one is deduced exploiting the scintillation light produced by the LAr excitation, collected by a Photon Detection System (PDS). Knowing the electron drift velocity, it is possible to calculate the position. In addition the LAr TPC exploits the intrinsically excellent calorimetry and tracking capability of LAr.

The choice of Liquid Argon as radiation detection medium presents both ad-

vantages and challenges. LAr presents a relatively abundant primary ionization and, if kept purified, a long drift distances which mean high electron lifetime. It has also a high light yield of 40k γ/MeV, in absence of electric field. This noble gas is easy available since it represents 1% of the atmosphere and usually relatively cheap. In order to fulfill the DUNE requirements some characteristics are to be considered. The requested purity from electronegative elements in Argon is <100 parts per trillions O_2 equivalent, to ensure an ionization-electron lifetime >3 ms at 500 V/cm drift voltage. To ensure its purification, a dedicated continuous purification system is necessary. Very low noise readout amplifiers are required in order to detect low primary charge deposition. A high voltage (HV) system is needed to provide a uniform E-field in a large drift volume. Some technological challenges for the DUNE LAr TPCs are represented by: a continuous non distructive readout of the detector necessary for its physics program, an online data filtering and reconstruction and a possible LAr doping.

Horizontal Drift SP LAr-TPC

The first module of the Far Detector, as already mentioned, will be a Horizontal Drift (HD) Single-Phase LAr TPC.

The design for FD1 is shown in Fig. 2.12. The inner volume of the detector is segmented in four drift regions. The structure is composed of alternated Anode and Cathode walls, with a drift distance of 3.5 m. An electric field of 500 V/cm is applied, which allows the drift process to develop on a time scale of the milliseconds.

The anode walls design consists of three planes of active wires, two faces each, plus an additional shielding grid layer around them. The first two layers produce bipolar induction signals and the final one collects the drifting electrons, producing a unipolar signal. The unit element of the anode wall is the Anode Planes Assembly (APA). Each wall is made of 50 of them, with two APAs high and 25 APAs wide. Vertically the APAs are stacked two by two (Fig. 2.13, left). There is a total of 150 APAs for the entire detector. The cryogenic front end read out electronic is attached at the top end and bottom end of each top APA (Fig. 2.13, right).

A Photon Detection System (PDS) is embedded inside the inactive space of the Anode Plane Assemblies structure, covering 12.5% of the APA surface. This allows to minimize the impact of the PD system on the active volume. The Photon Detectors used to collect scintillation light, are the so called X-ARAPUCAs. They consists of cells which act as light trap and captures photons inside boxes with highly reflective internal surfaces, with an expected Photon Detection Efficiency (PDE) of $\sim$3%. The photons are then collected by Silicon Photomultipliers (SiPMs), having a PDE of $\sim$45%, located on the long side of each PD module. A more detailed description of the different components of the PDS for FD1 will be

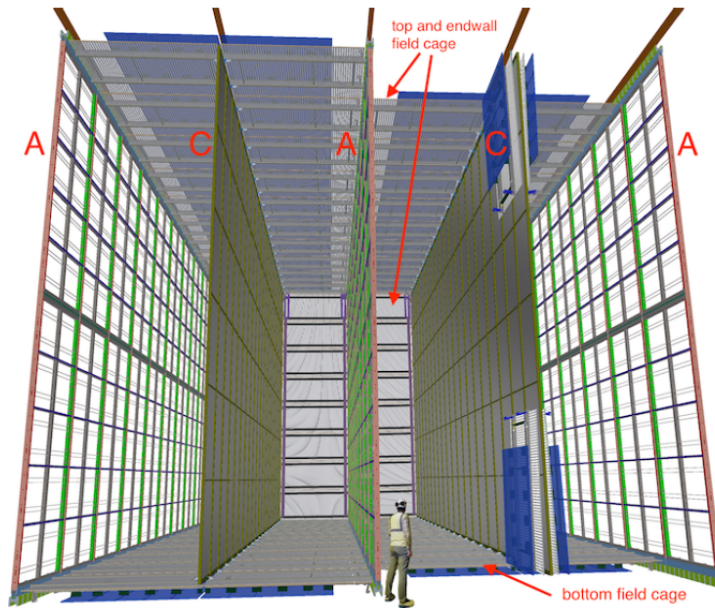Figure 2.12: Scheme for design of DUNE's Horizontal Drift SP LArTPC. The anode (A) and cathode (C) walls are visible. All around the detector is present a Field Cage (FC) to ensure the uniformity of the E-field inside the active volume.
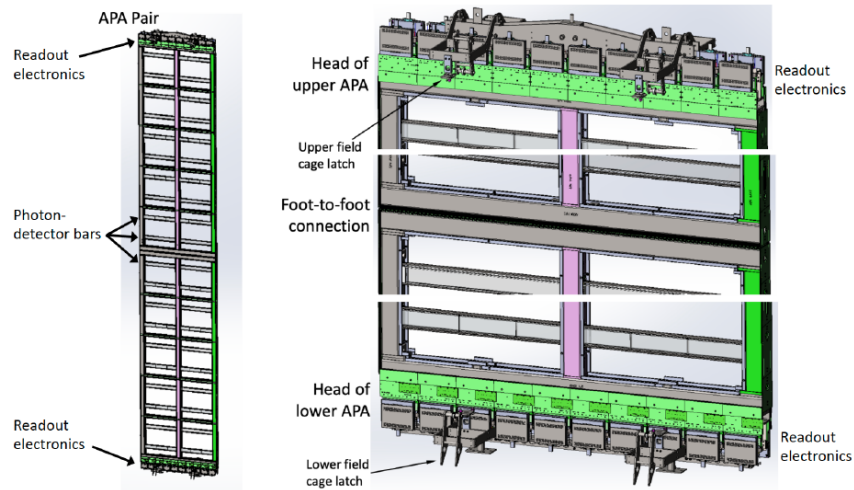

Figure 2.13: Left: an APAs pair consisting of two units linked together. Right: detail of the top end and bottom end of a top APA, where the front end electronic is attached.

given in the next chapter.

Similarly to the anode walls, the Cathode walls are composed of the Cathode Planes Assemblies (CPAs) and are 25 CPAs wide and 2 high, for a total of 100 CPA. A Field Cage (FC) surrounds the detector active volume to ensure the uniformity of the E-field throughout inside.

Vertical Drift SP LAr-TPC

The second module of the Far Detector (FD2) will be again a SP LArTPC but implementing the vertical drift technology. This choice allows to maximize the detector active volume.

Its design foresees the anodes close to the LAr surface and cryostat floor, while the cathode is suspended at middle height (Fig. 2.14). This configuration of the
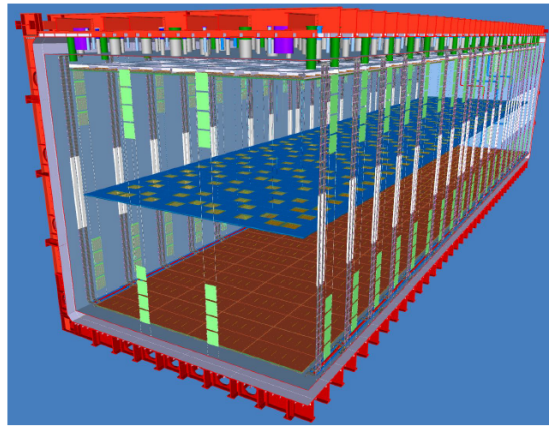

Figure 2.14: Design of the second module of the DUNE Far Detector. It is shown the Vertical Drift technology with the cathode suspended at mid high and the charge readout planes at the top and bottom of the cryostat.

cathode presents better High Voltage, stability due to LAr hydrostatic pressure and closer distance to cryostat walls. The produced electrons drift vertically towards the anodes where the readout units are located. The drift distance is 6.5 m, with 450 V/cm and the cathode at 300 kV. The read out units for the anodes are perforated multilayer printed circuit boards (PCBs), with integrated electronic interfaces. The anode plane design consists in stacking two double-sided anode PCBs, plus a shield layer facing the cathode. The first layer of PCB is cathode-facing and its back side is the first induction plane. The second layer has the second induction plane and its back face is the collection plane (Fig. 2.15). Electrons trajectories are so focused into 2D holes. A PCB-based anode presents some advantages compared to wire based. It is less expensive and less delicate, it also has a simpler support structure. Most components can be mass produced more
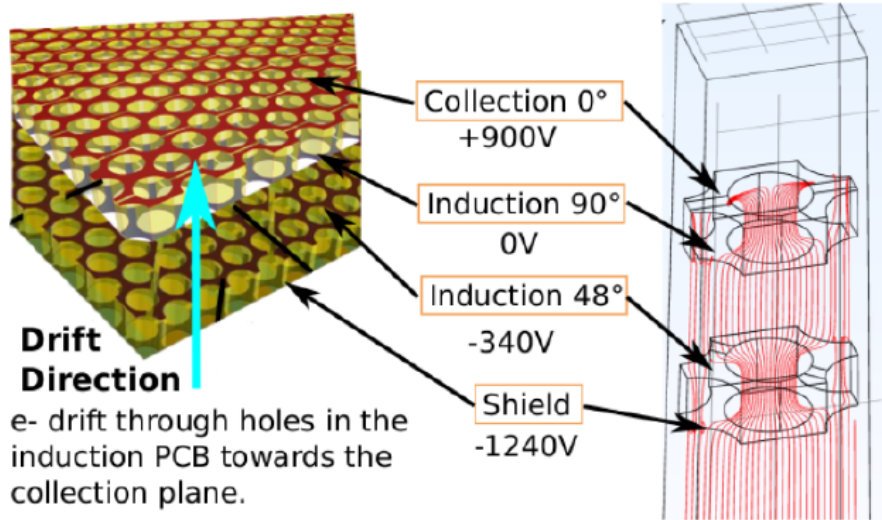
Figure 2.15: Detailed view of the perforated printed circuit componing the charge readout plane (left) and electric field lines inside (right).

rapidly using commercially available tools. The electric field is more uniform inside the holes. The signal is intrinsically larger than with wires and less dispersed, since mostly concentrated on a single electrode. This allows more uniform calorimetric response on all readout planes and less blurred imaging.

The anode planes are mounted on frames, to form Charge Read-out Planes (CRPs). Each full-size CRP is assembled from two half-CRPs. The CRPs that compose the top anode plane are suspended from the cryostat roof with suspension cables. Adjustments in the position are allowed in order to compensate for possible deformation of the cryostat roof geometry after LAr cooling and filling, maintaining the planarity of the anode plane. The botttom CRP is held about 160mm above the cryostat floor, by some bearing supports directly posed on the flat part of the membrane floor.

The PDS of the detector is integrated in the cathode planes and also placed on the cryostat walls. Similarly to FD1, it is based on the X-ARAPUCA technology, but with a different design for the photon detection module. A more detailed description of them will be given in the next chapter. The PDS has a total coverage up to 40%. The different components of FD2 are shown in Fig. 2.16.

2.1.4 ProtoDUNE at CERN Neutrino Platform

In the past years, the DUNE Collaboration has carried out an intense R&D program in order to validate the Liquid Argon Time Projection Chamber (LArTPC) technology for the multi-kt Far Detector. Following this effort, two different pro-
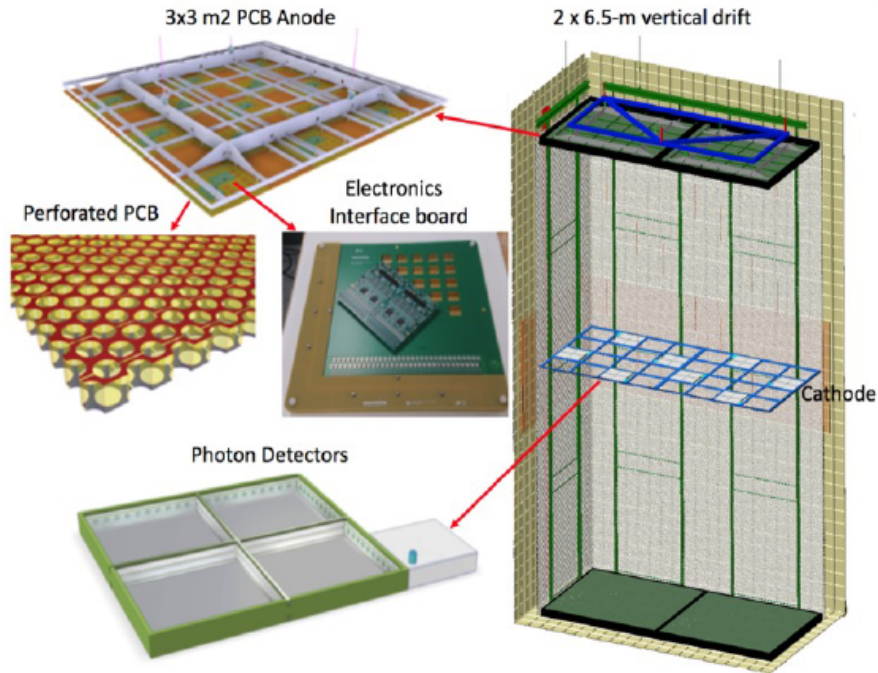
Figure 2.16: Details of the different components instrumenting the Vertical Drift LAr TPC detector.

totypes have been constructed at the so called Neutrino Platform, CERN. The Neutrino Platform (NP) provides the infrastructure needed to construct, install, and operate two large LArTPCs prototypes: ProtoDUNE Single Phase (SP) and ProtoDUNE Dual Phase (DP). After the approval of the project in 2015, the construction and installation of ProtoDUNE-SP was completed in early July 2018 and the first beam delivered in August of the same year. The beam run was completed in November 2018 but the detector remained operational until summer 2020. ProtoDUNE-SP represents the largest monolithic single-phase LArTPC detector ever built, with a total mass of 770 t of liquid argon. It was exposed to a dedicated test-beam line of charged particles. The data collected during this time validated the technology and demonstrated its operational stability [33]. The prototype served also as a test bench for the production and installation of all the different detector components. In addition, it is exploited to study the hadron and meson production inside the detector, the Ar cross-section interaction and other aspects relevant for the neutrino physics at the GeV energy scale.

ProtoDUNE-DP was a prototype of the Dual Phase technology. The working principle of a Dual Phase Liquid Argon TPC is reported in Fig. 2.18. This design has been taken into account since it presents, other to the usual Liquid Argon
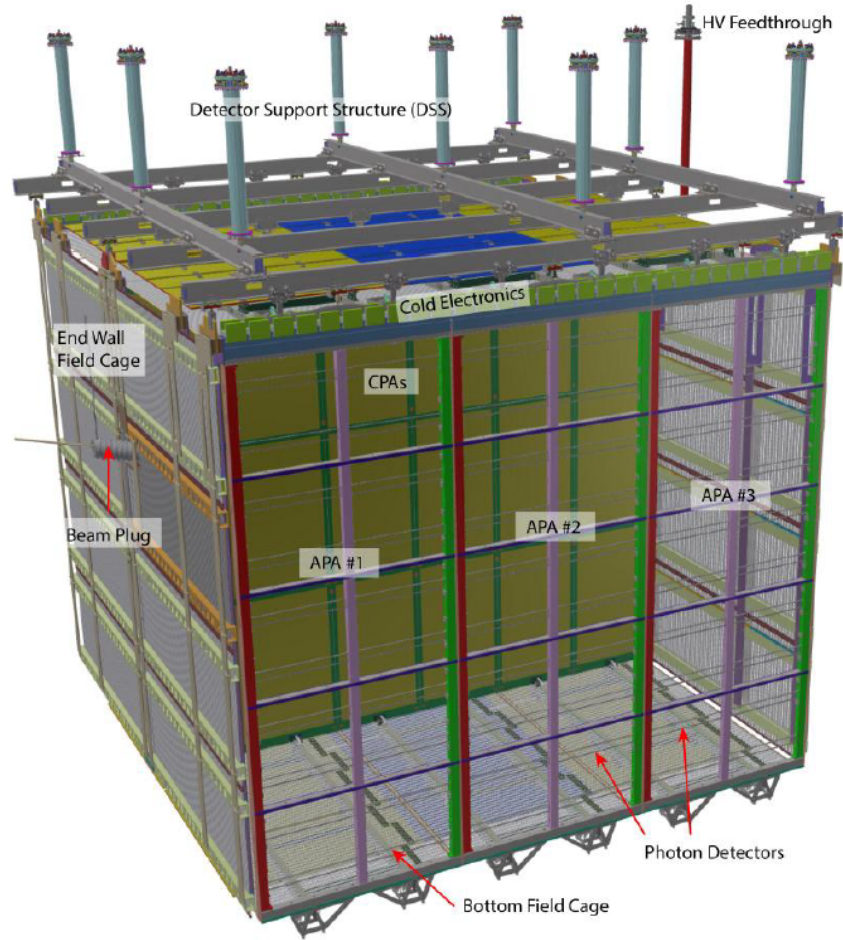
Figure 2.17: Design of ProtoDUNE-SP with all its internal components.

phase, a gaseous phase where the produced signal is amplified via multiplication of charged particles. ProtoDUNE-DP, with a total mass of 750 tons of LAr, took data from September 2019 to September 2020. After an intermediate update, a second run lasted from September 2021 to March 2022. Despite the good results obtained from its runs [34], it was decided not to implement the Dual Phase technology in any of the FD modules, since it would have required additional R&D for scaling to the DUNE size. Basing on the experience gained from its operation the design for the second module of the Far Detector has evolved into a Single Phase Vertical Drift technology LAr TPC.

Figure 2.18: Working principle of a Dual Phase Liquid Argon TPC (left). Schematic view of ProtoDUNE-DP with its main internal components (right).

Future perspectives

After the first run of the two prototypes, a new R&D phase has been carried out during last years. The cryostat once used for ProtoDUNE-SP (NP04) will be operational with the same technology but with upgraded components. ProtoDUNE-SP Horizontal Drift is now instrumented with updated Anode Plane Assemblies, Cathode Planes and cold electronics. Its design presents two Anode walls and one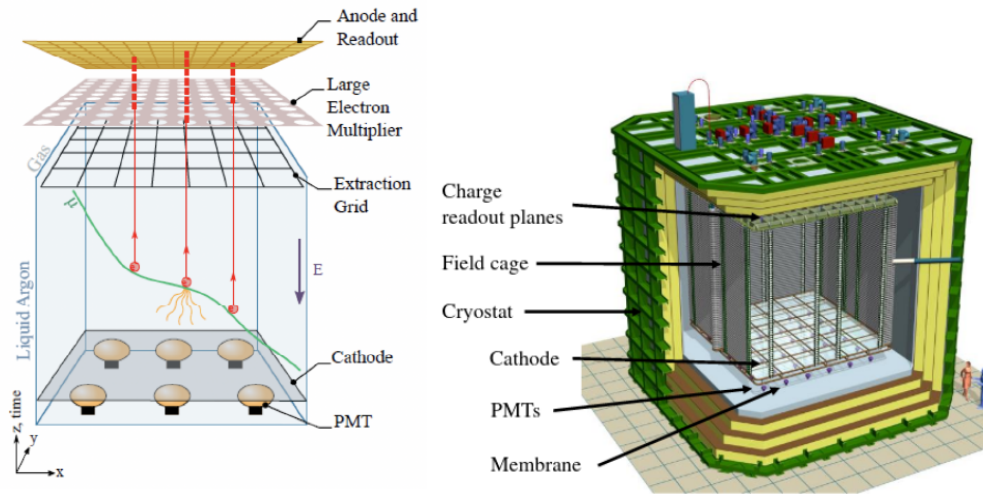 Cathode wall. The detector is hence formed by two back to back LAr TPC, each with a drift distance of 3.6 m. The foreseen applied electric field of 500 V/cm allows a drift time of milliseconds. In ProtoDUNE HD 40 optical modules, with 160 channels total, are embedded in the Anode walls (6.1 m long and 4.6 m wide) forming the PDS of the detector. Each APA, after being instrumented, has been tested in the cold box: a dedicated setup composed of a stainless steel vertical structure with dimension capable to host an APA. The tests performed at argon gas temperature, were aimed to study the response of the PDS. After these phase, all the APA were installed inside the cryostat.

The so called Module-0 in ProtoDUNE HD is ready since the end of 2022 and will be operated in 2024. It will represents the final validation of the Horizontal Drift technology in terms of: components production, assembly procedure and detector performances and stability. During its operation it will be exposed both to cosmic rays and to a beam of charged particles produced from the SPS, with E∼ 1GeV, to study and characterize the overall detector behaviour. Among them one of the first measurements will be aimed to characterization the slow component of the Liquid Argon scintillation light. Module0 will also test new proposed cali-

bration techniques such as a pulsed neutron source, radioactive source (^{207}Bi) and laser source.
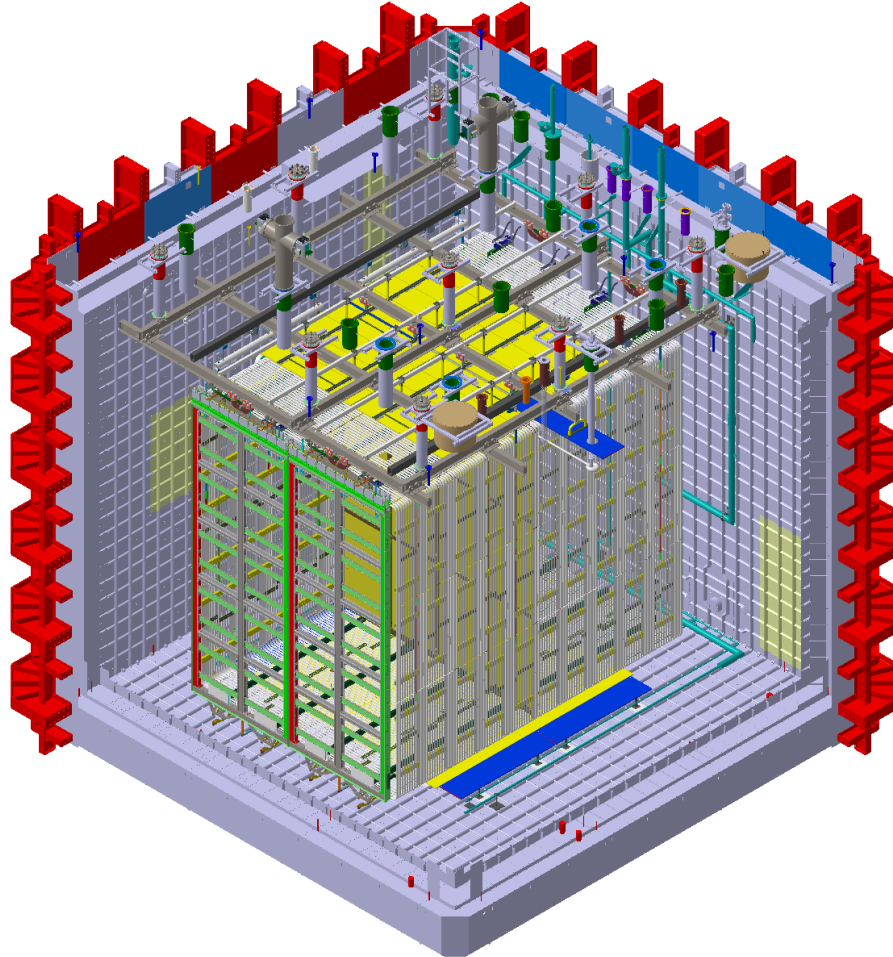
Figure 2.19: 3D model of the Module0 installed inside the NP04 cryostat.

As already said, many reasons has lead to discard a Dual Phase TPC solution for FD2, opting for a simplified design. The good LAr purity measured in the previous run of the prototypes, shown how it is possible a longer drift path. The charge readout electronics developed has demonstrated an excellent signal to noise ratio, making not necessary the multiplication in gas phase which, on the contrary, is challenging to maintain. Basing on these results and other practical consideration, it was decided to implement a LAr SP Vertical Drift TPC. The cryostat used to test the Dual Phase technology (NP02), will serves to validate the Single Phase Vertical Drift ones (Fig.2.20). Its instrumentation has started in
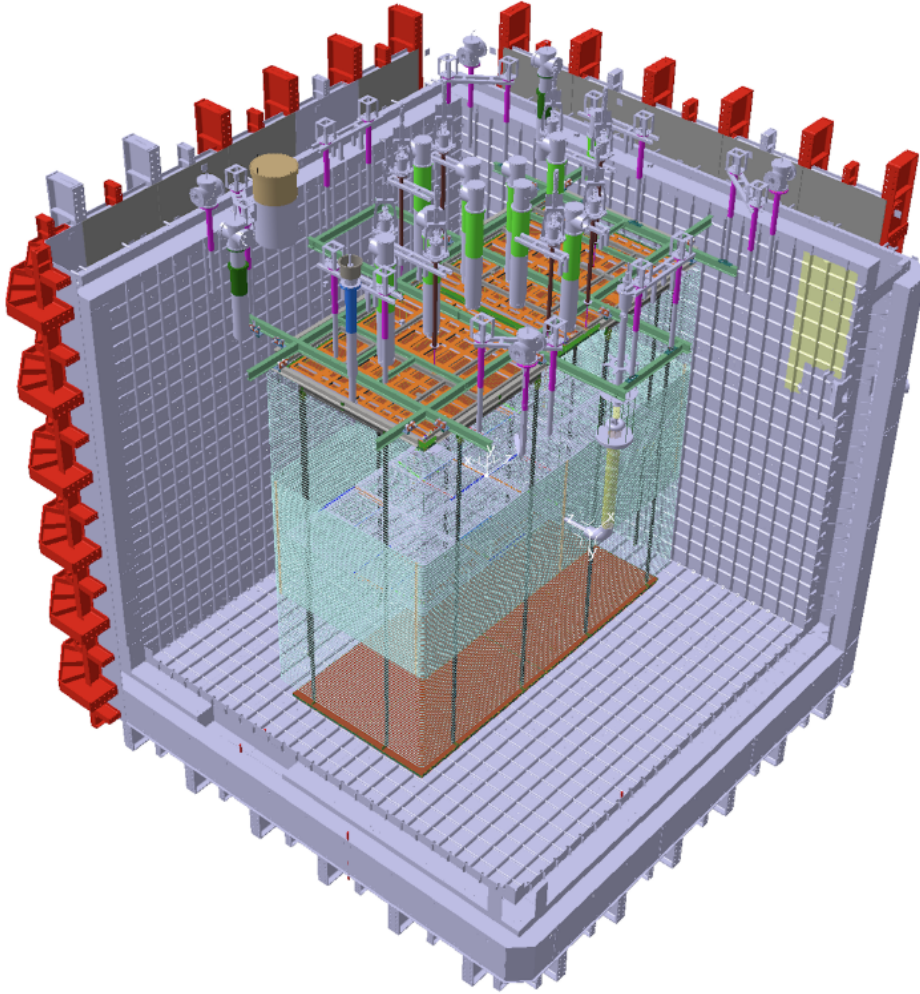
Figure 2.20: 3D model of the Module0 installed inside the NP02 cryostat.

2022 and ended in mid 2023. FD2-VD Module-0 contains an upper and a lower drift volume, each of which has two CRPs to read out the drift charge, separated by the cathode suspended at mid height. The photon detection system is installed in the cathode plane, a more detailed description will be given in the next chapter. Four additional PDS modules are installed on two of the cryostat membrane walls. As in the case of the ProtoDUNE HD, all the components of ProtoDUNE VD Module-0 have been tested in a specific setup. At the beginning of 2021, the NP02 cold box structure was refurbished and upgraded to host a full-scale CRP and cathode plane, with a cryogenic system ensuring stable thermodynamic conditions and good liquid argon purity. Several prototypes of CRP and cathode modules have been tested within the cold box. Module-0 has been instrumented with the latest optimized version of these modules.

The prototyping program has both engineering and scientific goals. The data taken in the past years has demonstrated the excellent detector's performance and have provided important information on the design, calibration and simulation of the DUNE Far Detector. The next campaign starting in 2024 will serve to validate the installation procedures, test the improved technologies and measure the physics response of the future detector modules with their newest design.

2.2 Physics program

DUNE has a rich scientific program. Its primary objectives are to determine unambiguously the neutrino mass ordering, observe a possible CP violation in the leptonic sector and test the three flavour scenario. Among these goals, DUNE has also a great potential in study other related fields. It will indeed search for physics beyond the standard model (BSM) such as proton decay, or perform astrophysics measurements such as studying supernova neutrinos burst.

2.2.1 Long baseline neutrino oscillation physics

DUNE will be designed as a long baseline neutrino oscillation experiment, with a travel distance of $\sim$ 1300 km. This characteristic will allow to conduct precise measurement of oscillation parameters and study phenomenon such as the matter-antimatter asymmetry which will contribute in determing the mass ordering and the value of δ_{CP}.

Neutrinos and antineutrinos travelling through matter present different oscillation probability, as already described in Sec. 1.3. The matter effect as shown in Eq.1.24 introduces a sensitivity to the sign of Δm_{31}^2, which specifies the neutrino mass ordering. Since the effect increases with baseline and amount of matter passed through, longer baseline experiments are more sensitive to the mass ordering. The matter-antimatter asymmetry adds to the one coming from a non zero value of δ_{CP} (Eq. 1.32). By measuring the total asymmetry in the case of $\delta_{CP} \neq 0, \pi$, the experiment will be both sensitive to CP violation and mass ordering. The two terms can be described with a dependence on the baseline and energy:

$$\mathcal{A}_{CP} \propto \frac{L}{E} \tag{2.1}$$

$$\mathcal{A}_{matter} \propto L \times E. \tag{2.2}$$

In Fig.2.21, the different values of the total asymmetry are shown both for the first and second oscillation maxima, for different baselines [35]. The plots report the oscillation probability asymmetries as a function of δ_{CP} and the green lines indicate the asymmetry at the first node for maximal CP violation ($\delta_{CP} = \pi/2$)

with an inverted ordering. At short baseline, at the first node, there is a degeneracy if the hierarchy is unknown. This means that at this baselines any observed asymmetry could be due to either the matter effect or CP violation at the first oscillation maximum. The degeneracy is solved at longer baseline values for which the matter asymmetry exceeds the maximal CP asymmetry at the first oscillation node, and the mass hierarchy and CP asymmetries can be resolved within the same experiment. This is the case of DUNE with its long baseline of ∼1300 km. Fig.2.22 reports DUNE's sensitivity to neutrino mass ordering and CP violation
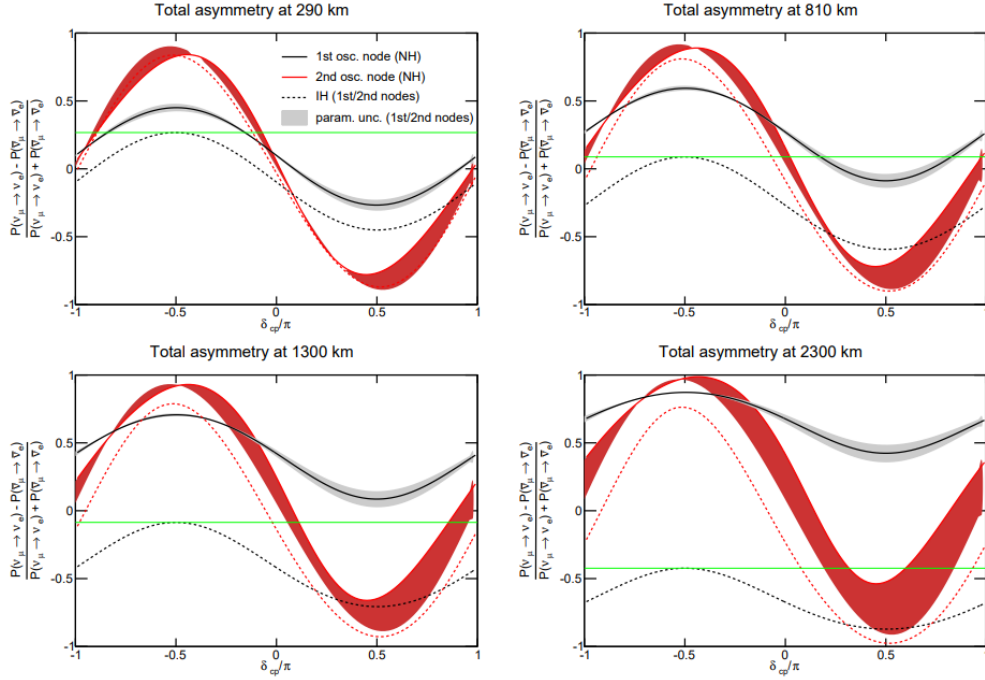
Figure 2.21: Oscillation probability asymmetries as a function of δ_{CP} for different baselines, calculated at the first two oscillation nodes. The black line represents the total asymmetry for normal hierarchy (solid line) and inverted hierarchy (dashed line) at the first node. The red lines are the asymmetries at the second oscillation node. The green lines indicate the asymmetry at the first node for maximal CP violation ($\delta_{CP} = \pi/2$) with an inverted hierarchy. In the first row it is shown how the value of δ_{CP} is ambiguous if the mass ordering is not known. In the second raw it is clear how the ambiguity is resolved.

as a function of the true value of δ_{CP}, in the case of normal ordering. The left plot shows how a sensitivity to the mass ordering of 5σ is reached independently by the δ_{CP} values, while the plot on the right shows how a 5σ sensitivity to CP violation is obtained with maximal violating values of δ_{CP}. DUNE will have different operational phases corresponding to different exposure rate. In Fig.2.23 it is

Figure 2.22: DUNE sensitivity to mass ordering (left) and CP violation (right) as a function of the true δ_{CP} value, for a given exposure and assuming normal neutrino mass ordering [36]. The dashed orizontal line highlights a sensitivity of 5σ (left) and also 3σ (right).
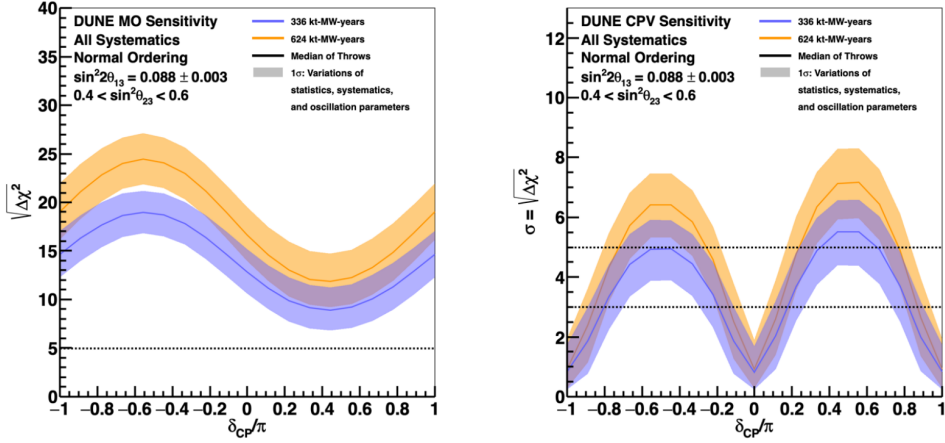
reported again DUNE's sensitivity to mass ordering and CP violation in the case of normal ordering, but this time as a function of the exposure. With an exposure of 100 kt-MW-years ($\sim$3 years of data taking), DUNE will be able to determine the mass ordering with a 5σ significance for 100% of δ_{CP} values. With the same exposure it will observe CP violation with 3σ significance for maximal CP violation (δ_{CP}=-$\pi/2$). The 5σ sensitivity will be reached for $\sim$350 kt-MW-years if δ_{CP}=-$\pi/2$. CP violation will be measured at 5σ and 3σ respectively for 50% and 75% of δ_{CP} values, after $\sim$700 kt-MW-years and $\sim$1000 kt-MW-years.

2.2.2 Low Energy Physics

Thanks to its large mass, DUNE Far Detector will be able to detect neutrinos in the energy range of 5-100 MeV. This feature is of great potential in studying neutrinos produced by the Sun or in supernovae core-collapse. These rare kind of events have a typical rate of few times per century. This means that it is not so unlikely to observe one of them during DUNE operational lifetime. Stars with a mass between 8 and 40 $M_\odot$ end their lives as Supernovae. This condition happens when the onion like star structure with a heavy iron core and lighter outer layers, is no longer in a thermal and pressure equilibrium state. The iron atoms start to decomposed due to the high temperature into alphas, protons and neutrinos. Electron Neutrinos are produced along with neutrons during the recombination of the free protons. Since they interact weakley, the produced ν_e can escape from the core, releasing energy but accelerating the collapse. This process, called
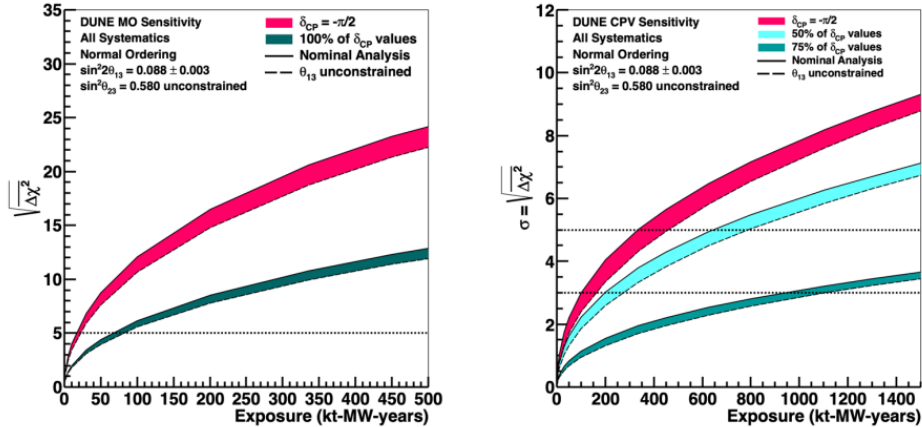
Figure 2.23: DUNE sensitivity to mass ordering (left) and CP violation (right) as a function of the exposure, assuming normal mass ordering. The curves reported are for maximal CP violation and for different fraction of δ_{CP} values [36].

neutronization (or *break-out*) burst correspond to a short, sharp signal of mainly ν_e. These escaping neutrinos are carriers of information from the inner layers. The following phase is the *accretion* one, of some hundreds of milliseconds duration, in which matter starts to collapse into the core. The star density begin to increase trapping the neutrinos inside the core, only those reaching the outer layers can escape. The final phase is the *cooling*, lasting over 10 s and representing the main part of the neutrino signal.

The flavour content and energies of the neutrinos emitted vary during these phases as shown in Fig.2.24. This means that the supernova's evolution can be studied through the neutrino signal. Exploiting the sensitivity to neutrino interaction of neutrino experiment can give a huge contribution to neutrino astronomy. An example of this capability came from Kamiokande and IMB which detected neutrinos emitted during the famous core-collapse of the SN1987 A. DUNE Far Detector is mostly sensitive to charged current of ν_e and $\overline{\nu}_e$, via absorption with Argon atom:

$$\nu_e(\overline{\nu}_e) + ^{40}Ar \rightarrow e^-e(+) + ^{40}K^* \left(^{40}Cl^*\right) \tag{2.3}$$

Until now, other experiments as for example HyperKamiokande and JUNO are sensitive primarily to electron antineutrino flavor, via inverse beta decay. This exclusive feature of being able to detect also to measure the ν_e content of the burst, which carries particularly interesting information, with high statistics and good event reconstruction will offer a valuable opportunity to the supernova neutrino detectors.In this context, the FD Photon Detection System will allow proper location of the event vertex and improve energy resolution by allowing position-dependent energy corrections and complementary direct calorimetric measurements. The
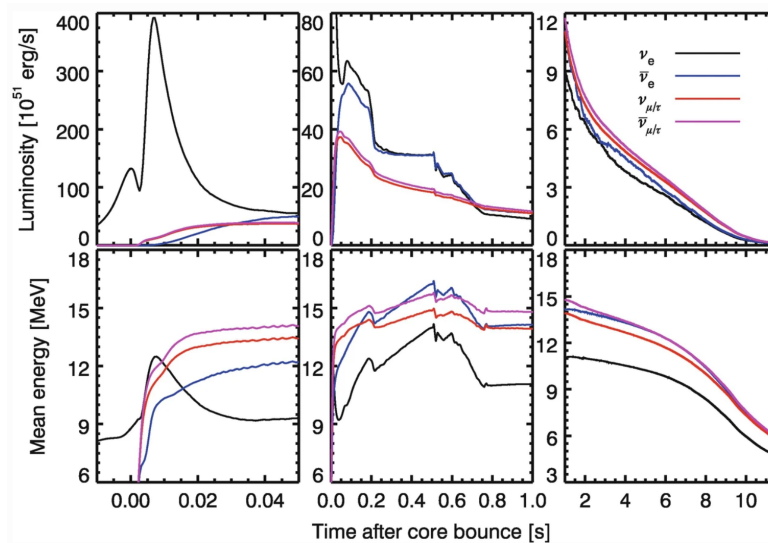
Figure 2.24: Neutrino luminosities and mean energies over time during the main different phases for the supernova explosion of a star of 27 M$_\odot$ [37]. The neutrino burst (left), the accretion phase (center) and the final cooling (right). The different curves corresponds to the neutrino flavour involved.

PDS will also play a crucial role by enabling a complementary triggering scheme for the burst itself, increasing reliability, reducing dead time, and extending the sensitivity further out to nearby dwarf galaxies. These applications to supernova physics set the average light yield requirement for the PDS.

DUNE will contribute in the so called SuperNova Early Warning System (SNEWS), a network of worldwide neutrino detectors, aimed to measure Supernova neutrino bursts and point back to the source. This prompt reconstruction will be a fundamental information in order to identify the region of the sky where to point telescopes.

2.2.3   Physics beyond the Standard Model

As already mentioned, DUNE will have a rich program of physics Beyond the Standard Model (BSM). Some of the fields involved in these studies are the search for sterile neutrino mixing, non standard interaction, dark matter candidates, violation of the charge parity time reversal symmetry (CPT) and baryon number violating processes [38].

DUNE will be sensitive over a broad range of potential sterile neutrino mass splittings by looking for disappearance of charge-current and neutral-current interactions thanks to the long baseline between the ND and FD and also over the short baseline of the ND.

The long travel distance along with the broad-energy beam, will also allow to improve the search for Non-Standard Interactions (NSI). The impact of this effect can be observed in a modification of the data collected since the neutrino are effected while propagating through the Earth if the parameters involved are large enough.

Searches for ligth-mass dark matter candidates (LDM) will be a focus in DUNE. Since no evidence of weakly-interacting massive particles (WIMP) has been detected at the high energy experiments as LHC, the focus has been shifted to LDM candidates. This search will be conducted mostly at the Near Detector. At the ND the Dark Matter (DM) particles can be detected via neutral current interactions with nucleons or electrons. This, considering the high flux neutrino beam, makes DUNE competitive but also complementary to others experiments in the field. Other types of DM candidates are the boosted dark matter (BDM). They will be potentially detected at the Far Detector.

The present limits for CPT violation in the neutrino sector will be improved by DUNE. In this context, studies conducted on atmospheric neutrinos should be promising in approaching physics BSM.

Lastly, the search for baryon number violating events will be feasible thanks to DUNE's deep underground location and large fiducial mass of the Far Detector. DUNE indeed will be able to observe the signature of protons ($p \rightarrow K^+\overline{\nu}$) and neutrons decays ($n \rightarrow e^- K^+$) at rates lower than the ones set by previous experiments. Fundamental in this case will be its excellent event imaging reconstruction, particle identification and calorimetric capabilities.

Chapter 3

Far Detector Photon Detection System

Main purpose of the Photon Detection System (PDS) is to collect and measure the scintillation light emitted during neutrino interactions in the Liquid Argon.
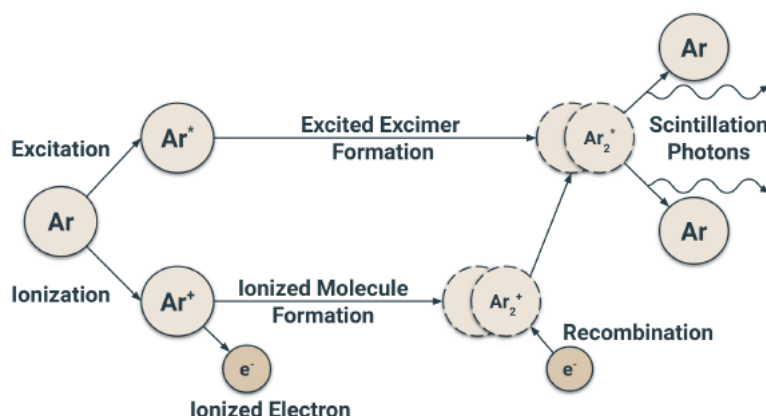
Figure 3.1: Schematic principle of the two processes to which an Argon atom can undergo after the passage of a ionizing radiation. The two chains of events are reported for both the excitation and ionization case.

The working principle is the excitation and ionization of argon atoms after the passage of ionizing radiation (Fig. 3.1). The products of these two processes are, an exciton (Ar^*) in the case of excitation and an electron-ion pair (Ar^++e^-) for the ionization. Both states, coupling with an Ar atom, lead eventually to the formation of the excited dimer of Ar_2^*. Scintillation photons emission results after the de-excitation fo the lowest lying singlet $^1\Sigma_u^+$ and triplet state $^3\Sigma_u^+$ to the dissociative ground state [39]. The two characteristic decay times are very different. While the singlet is characterized by a fast lifetime (τ_{fast}) of $\sim$7 ns, the triplets

is much slower, with $\tau_{slow} \sim 1.5$ μs. In both cases, the photons are emitted in a 10 nm band centered around 127 nm referred to as Vacuum Ultra Violet (VUV). The time profile of the emission is thus composed of a fast component and a slow one. In a Liquid Argon TPC the point of collection of electrons on the anode plane is combined with their drift time from the fast component of scintillation light to reconstruct charged particle tracks. The total number of collected photons, including also the slow component, is used to increaase calorimetric energy resolution.

Liquid Argon emits, in absence of external electric fields, about 40k photons/ MeV when excited by minimum ionizing particles (mip). The potential electron recombination is suppressed in presence of an external electric field. In doing so, also the excimers which contribute to generate most of the VUV light emission in LAr are suppressed. Scintillation intensity decreases with the increase of the applied electric field [40]. The general impact is a reduction of the photon yield. In the case of DUNE Horizontal Drift, with nominal module field of 500 V/cm, the yield for a mip is $\sim$ 25k photons/MeV .

Scintillation light production and propagation is affected by possible impurities present in Liquid Argon. Depending on the type of impurity, they can effect the process by quenching or absorption. Nitrogen (N_2) for example, can quench scintillation light production by reducing the number of Ar_2^* excited molecules through non-radiative collisional reactions, before their deexcitation ($Ar_2^*+N_2 \rightarrow 2Ar+N_2$). As a consequence, since the effect impacts particularly the triplet excimer states, it reduces the amplitude of the slower component of LAr scintillation light. A solution to mitigate the process is by Xenon doping of Liquid Argon. The doping produce a competing reaction ($Ar_2^*+Xe_2 \rightarrow ArXe^*+Ar$), recovering most of the scintillation light. Additionally, Xenon doping reduce Nitrogen absorption of VUV light, which affects Argon transparency. Small amount of Xenon [41] indeed has the consequence of shifting the slow component of scintillation light to 175 nm, at which the Nitrogen photoabsorption cross-section is lower than at 127 nm.

3.1   FD1 Photon Detection System

As already described in Sec. 2.1.3, the first module of DUNE FD will be a single phase LAr TPC with Horizontal Drift. Its Photon Detection System main task will be to collect and measure the VUV scintillation light produced by ionizing tracks inside the detector, within the geometrical constraints of the Anode Plane Assembly (APA) structure. The configuration of the HD LAr TPC develops throught the width of the cryostat. Its segmentation starts with an APA plane in front of one cryostat wall followed by a Cathode Plane Assembly (CPA), repeating the scheme in an alternated way until the instrumentation of the active volume is complete.

One of the difficulties encountered in designing the PDS is the necessity to reduce its impact on the LAr active volume, while maximizing the light collection efficiency. This, along with the APA structure, makes not feasible the use of traditional large area photomultiplier tubes (PMT). The solution opted for is to place the light collector modules embedded in the APA, placed in the inactive space between the innermost wire planes. The PDS modules are so confined into slots of reduced size, having considered the geometry of the APA. This reduce to zero the impact of the PDS on the active volume but, consequently, implies to choose photosensors with small surfaces but high efficiency. The design of the PD light collector module is based on the ARAPUCA technology.

The process of detecting scintillation light over a large area into a compact space requires several steps. The ARAPUCA is a device composed of a light collector which act as light trap and captures photons inside boxes with highly reflective internal surfaces. The photons are then read-out by Silicon Photomultipliers (SiPMs) coupled to the collectors. The acceptance window of the box is a short-pass dichroic filter, which is highly transparent to photons with wavelength below a given cut-off, but highly reflective to photons with wavelength above the same cut-off [42]. Since photons from LAr are emitted in the VUV, it is necessary to shift their wavelength and make them detectable to standard photosensor. This is made once by a thin layer of wavelength shifting (WLS) material deposited on the outer side of the dichroic filter. This first shifting is to a wavelength of 350 nm below the cut-off, to allow the photons entering the ARAPUCA. Once inside, a second shifting is performed again but this time to a wavelength of 430 nm, above the cut-off in order to trap photons inside and prevent them to leave. The internal shifting can be made in different ways. In a first design of the ARAPUCA, it was performed by coating with reflective material either the inner surface of the filter or the internal surfaces of the box. This was the so called S-ARAPUCA (Standard ARAPUCA). Different versions of the S-ARAPUCA have been tested. This technology was also one of those installed and tested during the first run of ProtoDUNE-SP. A subsequent and final design is the X-ARAPUCA (Extended ARAPUCA). In this case the shifting in the wavelength is feasible thanks to a WLS plate inside the box (Fig. 3.2). The emission is performed at wavelength higher than the filter plate transmission frequency.

This structure of multiple different layers composes a cell (Fig. 3.3). Photons coming from the WLS plate can eventually reach the SiPMs or being transported along the WLS plate via total internal reflection or also, those escaping the plate, being reflected back inside the device by the dichroic filter. One of the improvements made in the X-ARAPUCA is the possibility of being single-face, having only one face instrumented, or dual-face with a second dichroic filter window on the second face. In the case of DUNE FD1, the photon detector modules inserted
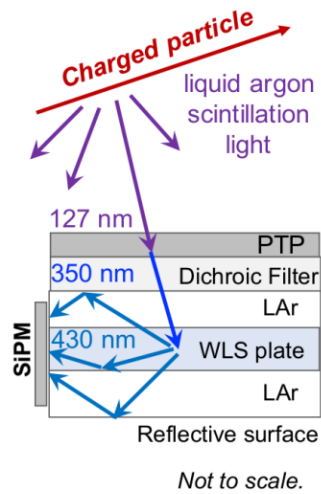
Figure 3.2: Working principle of an X-ARAPUCA. The pictures shows the wavelenght shifting process of the photons reaching the device along with different possible paths for their internal reflection.

in the central anode walls will be dual-face, while those closer to the cryostat walls will be single-face.
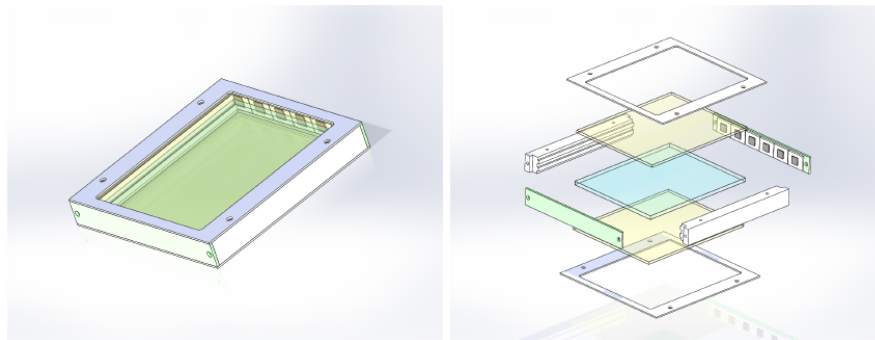
Figure 3.3: An X-ARAPUCA dual-face cell, assembled (left) and exploded view (right). The yellow surfaces are the dichroic filters while the blue one is the WLS plate. The SiPMs are visible on the short sides of the cells.

3.1.1 X-ARAPUCA Supercell

In DUNE FD1, the base element of the Photon Detection System modules is the X-ARAPUCA Supercell. A supercell is assembled in a bar-like structure. Each of them hosts six dichroic filters tiles for an entrance window of 78 mm×93 mm and total exposed area of 43.524 mm^2 (Fig. 3.4). Dual-face modules have twice the

filters, in order to instrument both sides. The Silicon Photomultipliers are located on the long edges of the cell facing the short side of the WLS plate. The light collected by the module is eventually turned into electrical signal by the SiPMs. Each Supercell has a total of 48 SiPMs, grouped in arrays of 6 mounted on a same Printed Circuit Board (PCB) and electrically connected in parallel ("passively ganged"). The area of a single SiPM is 6×6 mm^2.
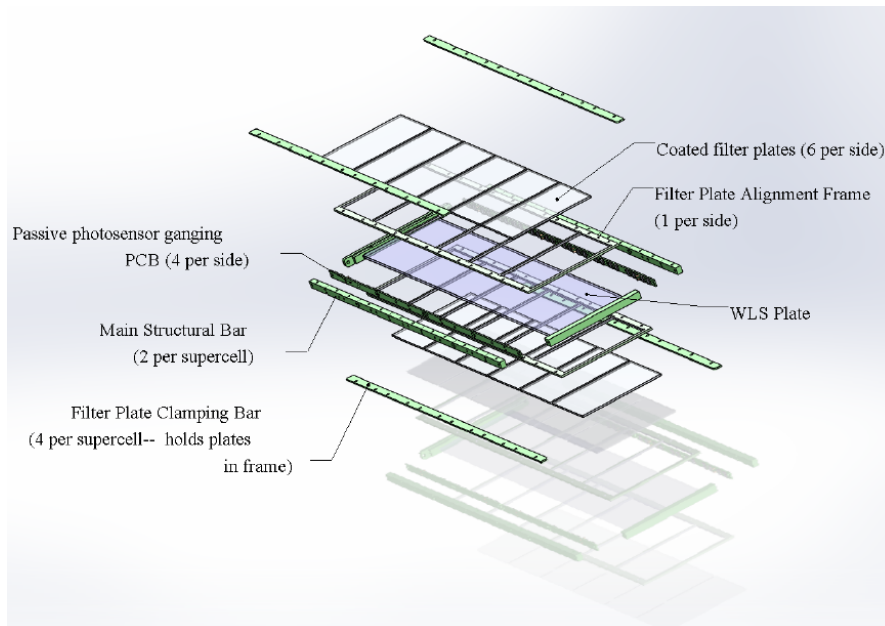
Figure 3.4: Individual Supercell of the PD System.

The individual module of the Photon Detection System is composed of four Supercells (Fig. 3.5) with total dimensions of 2092 mm × 118 mm× 23 mm. A G10 frame holds all the components of the PD module. All the internal surfaces of the Supercell are lined with Vikuiti®, a highly reflective material, in order to maximize the internal reflection.

The 192 SiPMs per each PD module are electrically ganged in group of 48, into four electronics readout channels. This configuration implies a total of 288000 SiPMs for DUNE FD1, as reported in Tab. 3.1. A cryogenic amplifier [43] [44] forms the obtained output signals before transmitting them over an average length of ∼20 m cables, to the input of the front-end electronics.

The PD module is not empty inside: Liquid Argon fills all the gaps of the module structure. This, on one hand ensures the discontinuity of the refractive index that contributes to effective trapping of the photons while on the other hand, requires that all the components of the PD module withstand cryogenic temperature, especially the photosensors used. The detailed description of the
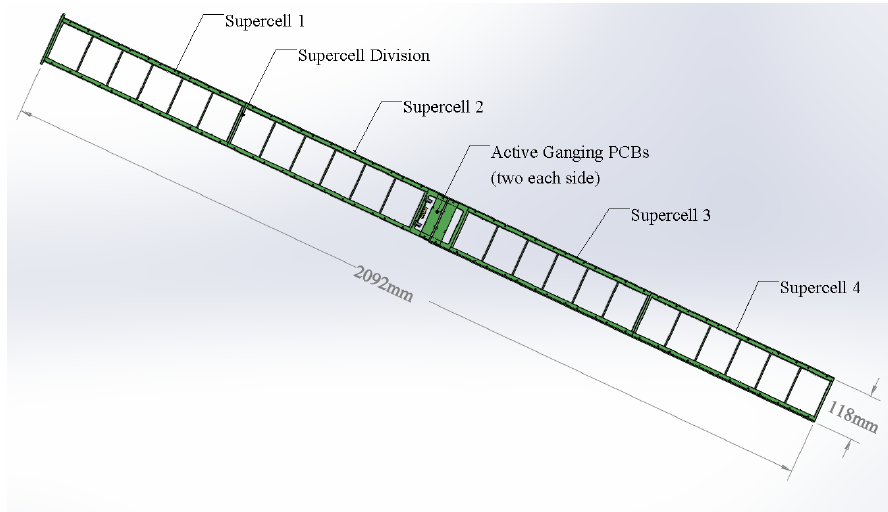
Figure 3.5: PD module for DUNE FD1. One module is composed of 4 Supercells, each of them with 48 SiPMs for a total of 192 photosensors per PD module. This bar-shaped structure is eventually inserted in the inactive space of an APA.

tests performed to select and validate the optimal model of SiPM to install in DUNE PDS, will be describe in Chapter 4.

The different PDS components are listed in Tab. 3.1.

Component	Description	Amount
Light collectors	X-ARAPUCA	10 PD modules per APA; 1500 total for FD1, (1000 single-side, 500 double-side)
Photosensor	SiPM 6×6 mm²	192 SiPMs per PD module, 288000 total for FD1
SiPMs signal ganging	6 passive × 8 active	4 circuit per PD module, 6000 total for FD1.

Table 3.1: Reference configuration of the components for FD1 Photon Detection System. One PD module is composed of 4 X-ARAPUCA Supercells.

3.2 FD2 Photon Detection System

The second module of DUNE Far Detector will be a single phase LAr TPC with Vertical Drift. With this technology the detector develops in height. The configuration foresees a Charge-Readout Plane suspended from the top and one located

Figure 3.6: Detail of the PD modules location in the APA frame (left). Supercells inserted between the wires planes, in an APA inside the ProtoDUNE-HD cryostat (right). From the picture are visible the bar-shaped modules with the mounted filters.

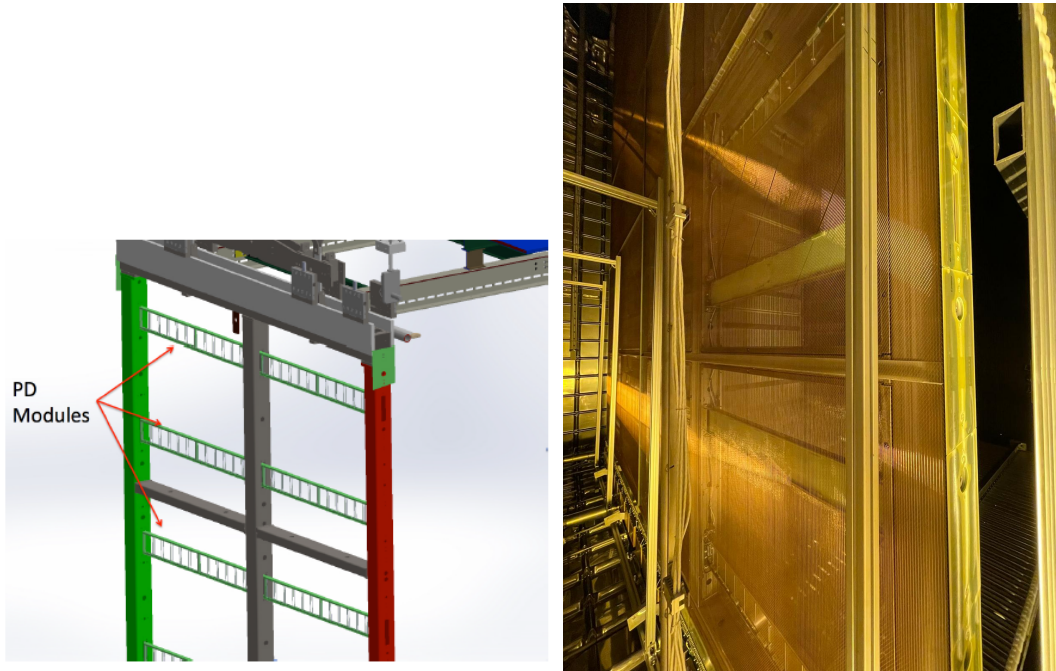at the bottom of the cryostat. This design, already described in Sec.2.1.3, does not allow to install the Photon Detection System in the anode plane as in FD1, since the CRP is effectively opaque to the light. As a consequence the PDS can only be located on the cathode plane and on the cryostat walls behind the field cage. Placing the PD module on all the four cryostat membrane walls, significantly reduces the non-uniformity in the light yield along the drift direction. This is only feasible of course, provided the field cage is sufficiently transparent to light. The two solutions present the advantage of improving the light detection uniformity by increasing the PD coverage to 14%. But, on the other hand, the cathode placement is challenging due to the high voltage (HV) environment. The PD modules mounted on the cathode will not be able to use the same copper-based sensor biasing and readout technology of FD1-HD, as the membrane modules will do, due to their properties of being at the same cathode voltage, so no conductive path to ground is possible. The solution adopted to address this constraint is to power the modules through power-over-fiber (PoF), a non conductive technology using fiber-optic cables to carry optical power remotely. Power is transmitted by sending laser light (at 971 nm) through non-conductive optical fibers. The PoF units is composed of

a laser transmitter module on the warm side, a fiber link, and a PoF receiver on the LAr side, which is an optical photovoltaic converter (OPC), delivering power to the readout electronics and to the bias generation circuit (Fig. 3.7). The same concept is used for the output signal transmission, exploiting a signal-over-fiber (SoF) mechanism: SiPM electrical signals are converted into optical signals and transmitted by SoF laser diode via optical fiber. Even though the PoF technology is well known, its application to cryogenic environment is quite innovative.
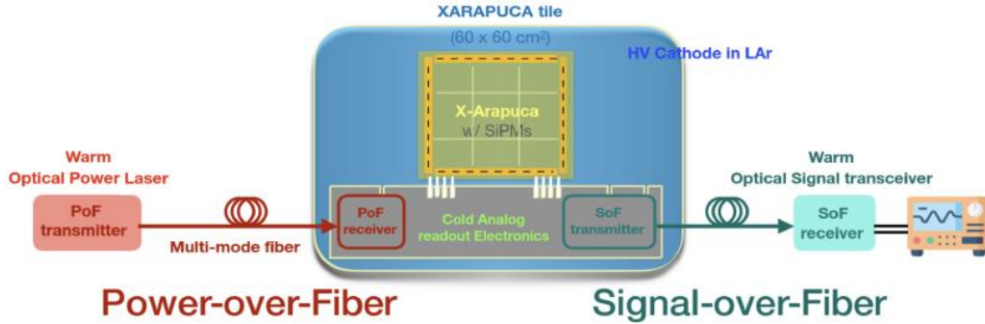

Figure 3.7: Diagram of the PoF and SoF components used for the FD2 PD module.

3.2.1 X-ARAPUCA Megacell

The Photon Detection System of FD2 will be used to collect scintillation light, the X-ARAPUCA technology as in FD1. Even though the light trapping principle is the same, the design of the single modules is different. The basic unit is the so called X-ARAPUCA Megacell, a tile-shaped thin module with dimensions of 653mm × 653mm × 29.9mm plus an attached electronics box with dimensions 645mm × 89.6mm × 42.4mm in which the cold electronics is enclosed (Fig. 3.8). Depending on their final placement, the modules can be either double-sided (cathode-mounted) or single sided (membrane modules). Fig. 3.9 shows how the cathode module are embedded in its structure. Each double-sided Megacell has mounted 32 PTP-coated dichroic filters tiles while the membrane modules have 16 filters only, since the back side facing the cryostat wall is a G10 plate lined with Vikuiti®. Inside the module a WLS-doped acrylic plate acts as a secondary shifter. The light collected is eventually converted into electric signal by SiPM to which the WLS plate is coupled. Each module has a total of 160 SiPMs, mounted on a flexible Kapton PCB in groups of 20 passively ganged to sum their signal. The SiPMs on a same flex are biased at the same voltage ensuring a small capacitance and thus a lower noise and faster response time. The output from four flex PCBs are fed into a cold amplifier, thus providing a readout of the combined response of 80 ganged into a single electronic channel.

The list of configuration components for the FD2 Photon Detection System is reported in Tab. 3.2.
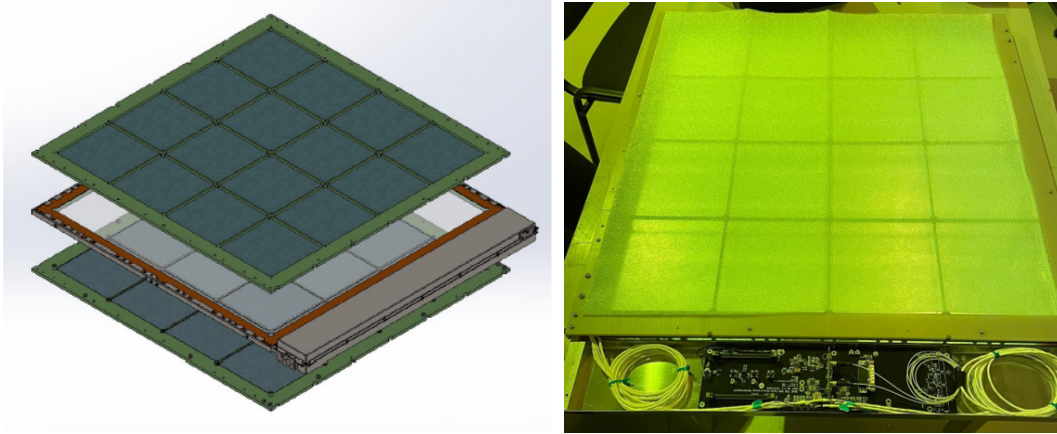
Figure 3.8: Design of a double-sided Megacell meant to be installed in the cathode plane structure (left). Single-sided membrane module with the electronic box open (right), the electronic board with no PoF receiver is visible.
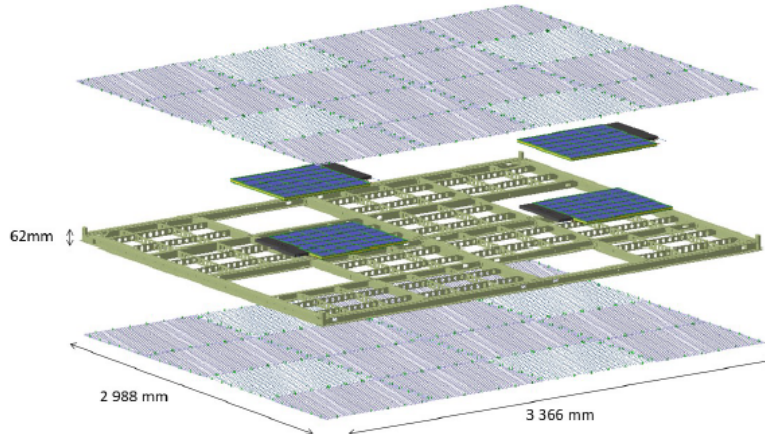
Figure 3.9: Cathode plane module structure with visible where the PD modules (blue box) are inserted. Each side of the cathode is covered by a resistive mesh, which is conductive only above/below the ARAPUCA modules, to protect the PD module from the effects of potential discharge. The mesh is however of 90% optical transparency, thus minimizing its impact as an obstacle for light collection.

Component	Description	Amount
Light collectors	X-ARAPUCA	352 membrane modules (single sided), 320 cathode-mounted modules (double sided) 672 total for FD2.
Photosensor	SiPM 6×6 mm^2	160 SiPMs per PD module, 107520 total for FD2
SiPMs signal summing	4 passive × 5 active	8 flex PCBs per PD module, 65372 total per FD2

Table 3.2: Reference configuration of the components for FD2 Photon Detection System. A PD module is an X-ARAPUCA Megacell.

3.2.1.1 Modules tests - Optimization of the electronic box design

A cryogenic facility to test full scale X-ARAPUCA Megacell modules and their readout electronics, has been constructed at the Neutrino Platform, CERN. The system has been used to check the functionality and validate the modules before their installation in Module 0 inside ProtoDUNE Vertical Drift cryostat. To test the PD module in LAr, an open dewar of 70 cm diameter and 120 cm height filled with non purified LAr, is used. The dewar can be sealed with a lid to ensure light tightness. A trolley with a winch is employed to lower or extract the PD module from the LAr bath (Fig. 3.10). The lid of the dewar, to which the Megacell is attached by a support structure, is instrumented with an optical and electrical feedthrough to inject controlled light with an LED, to power the cold electronics and bias the SiPMs and read out their signal. Temperature sensors located at different heights within the Megacell support structure allow to monitor the temperature and LAr level during the submersion and warm-up phases. From beginning of 2023 all 16 X-ARAPUCA modules for FD2-VD Module 0 were tested and validated using this facility.

During the training period abroad foreseen by my PhD course, I participated in the assembly, testing and mounting of the Photon Detection System modules of ProtoDUNE Vertical Drift.

The validation procedure performed on the Megacell modules in the LAr bath, included the study of the modules response to different LED intensities and data taking with cosmic rays. From the data acquired by the LED run an evaluation of the Signal to Noise ratio (SNR) was computed, while the cosmic rays data have been used to estimate the gain ratio between the two channels of the modules. Throughout these analyses an unexpected light leakage from the PoF was
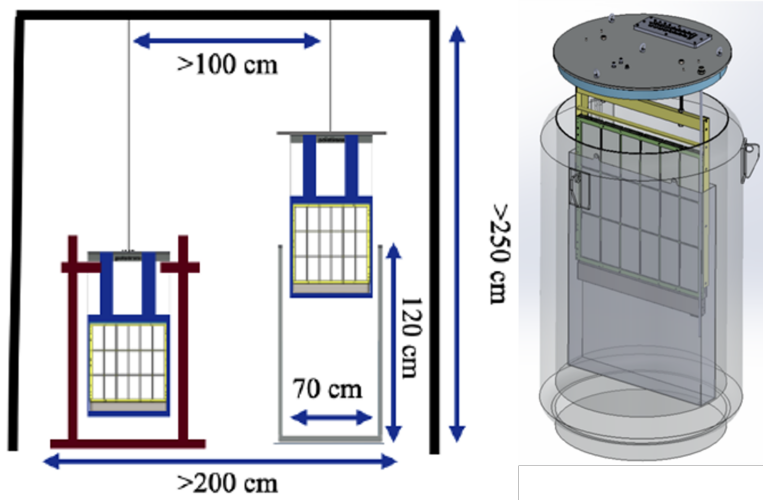
Figure 3.10: Design of the test facility constructed at the Neutrino Platform (CERN), to test and validate the PD module for ProtoDUNE Vertical Drift.

measured. The leakage affecting the module response was caused by the light transmitted by the PoF escaping from the holes present in the electronic box for LAr circulation.

In this context it was evident the necessity to improve the electronic box design. Taking part in the tests, I developed a study on several possible geometries of the electronic box, in order to reduce the observed light leakage.

The geometries I implemented describe different solutions to cover the circulation holes on the lid and base of the box. In the code are defined the elements with major size (as the fiber support, led driver, DC/DC converter etc) composing the electronic board housed in the box and measured on site at CERN. Fig. 3.14 shows on the left the electronic box opened with the holes on the lid covered with PTFE (Polytetrafluoroethylene) tubes, as one of the first solutions, and on the right the electronic board, attached to the base of the box, with the main components described in the geometry.

The cases I defined are:

- an initial condition of geometry with only the electronic box, the LAr circulation holes and the electronic board housed inside. This solution presents on the lid four holes in staggered position with respect to the x,y axis (Fig. 3.14) and four holes in the bottom part of the box in symmetric position to the x,y axis. This represents the starting point of the study as it is the box design as originally produced;

- a first case of holes covered. In this first attempt to reduce the light leakage,
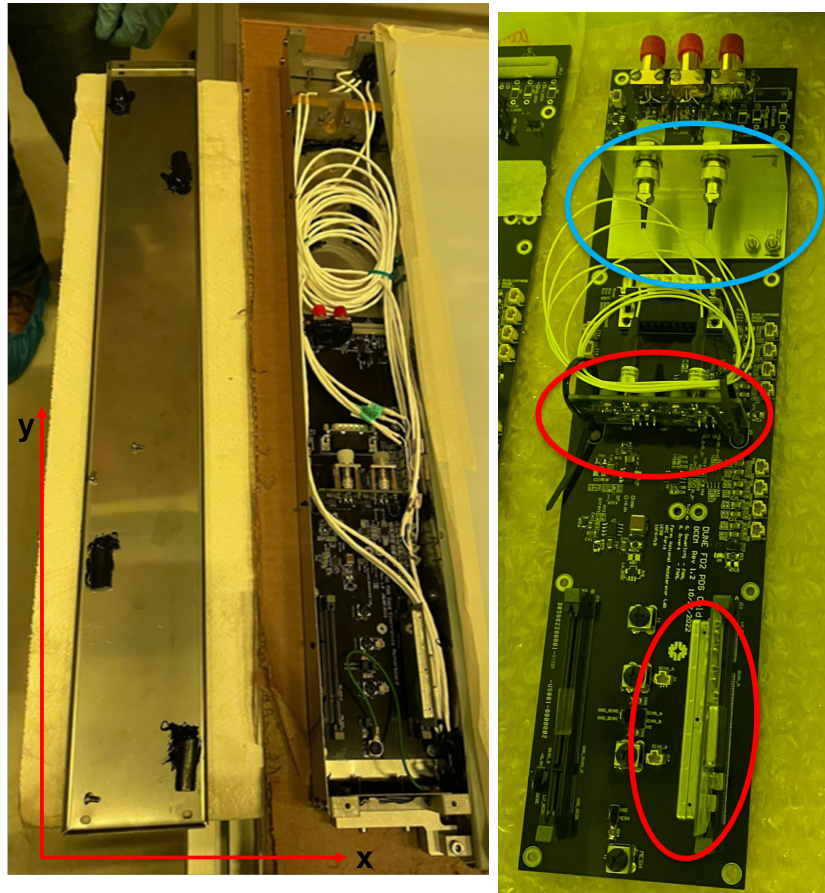
Figure 3.11: Electronic box opened with visible on the lid the tubes covering the ventilation holes (left) and the electronic board with circled the main components described in terms of dimensions, material and properties in the geometry code.

the elements used to screen the openings are long sliced Polytetrafluoroethylene (PTFE) tubes, with closed edge on the side facing the PoF and the other opened to ensure the LAr circulation;

- a solution with two absorbing plates covering the holes, placed on the lid and on the top of the PoF entrance side of the box. The openings on the opposite side of the fibers are covered again with PTFE tubes as defined above;

- a third solutions with only tubes as above closed on the side facing the fiber and open on the opposite side, but longer and made of Stainless Steel (SS);

- a combination of plates placed around the PoF and SS longer tubes;

- a final solution with only plates placed both around the fibers entrance side

and on the opposite side above the electronic board.

Tab. 3.3 reports the different elements along with their material and reflectivity as assumed in the geometry code, further investigation on the effect due to reflectivity deviation from the baseline values will be conducted with a full simulation of the entire PD module geometry. Tab. 3.4 reports the more specific material compositions implemented.

Component	Material	Reflectivity [%] (976 nm)
Box structure	stainless steel (polished)	64
Fiber support	Aluminum	90
Electronics elements (dc-dc converter, led driver etc)	FR4	~40
Tube	PTFE (Polytetrafluoroethylene)	~30
Absorbing plate	FR4	~40

Table 3.3: Reflectivity of the different components implemented in the electronic box geometries.

Each geometry has been implemented in a framework of Geant4 optical simulations to study the photons production from the PoF and light interaction with LAr and electronic box. The simulation run was performed with a production of 20×10^6 photons considered statistically satisfactory. In Tab. 3.5 are reported some of the assumptions for LAr proporties implemented in the simulations framework.

The ventilation holes have been implemented in all the geometries as absorbing disks. The fraction of photons escaping the electronic box through them has been calculated as the ratio between the number of photons arriving on the openings and those simulated as produced by the source.

Material	Composition
FR4	Epoxy resin and Fibrous Glass
PTFE	G4 Rubber Butyl

Table 3.4: Composition of the more peculiar material implemented in the geometry code.

LAr Properties	Values
refractive index	1.24
group velocity	$2.41 \cdot 10^8$ m/s
Rayleigh scattering	>90 m
Absorption	50 m

Table 3.5: Liquid Argon optical properties assumed in the simulation framework.
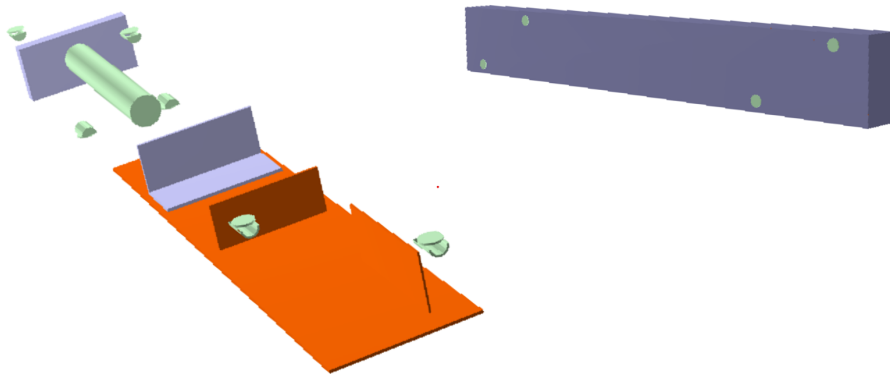
Figure 3.12: Example of a visual representation of the major elements inside the electronic box: fiber support, led driver, DC/DC converter, PCB board, LAr circulation holes and tubes (left) and of the closed box structure (right).
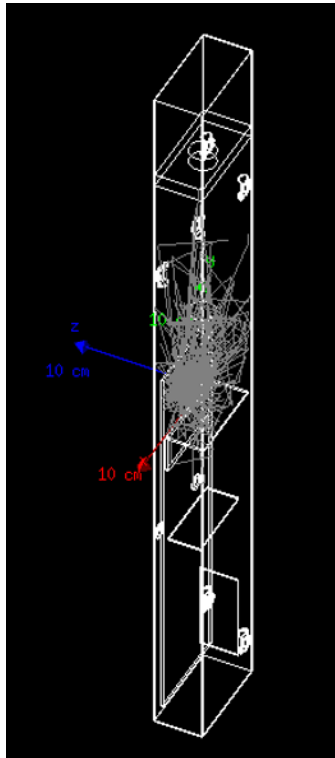
Figure 3.13: Example of the photons behaviour as simulated based on the geometry with holes covered with short PTFE tubes.

Geometry	Fraction of photons escaping
Box with only ventilation/circulation holes	$(3.86 \pm 0.05) \times 10^{-4}$
holes shadowed by PTFE tubings	$(4.1 \pm 0.5) \times 10^{-6}$
holes covered by absorbing plates, PTFE tubings	$(1.4 \pm 0.3) \times 10^{-6}$
holes shadowed by 4.0 cm long Stainless Steel (SS) tubes	$(1.14 \pm 0.08) \times 10^{-5}$
holes covered by absorbing plates, SS tubings	$(2.0 \pm 0.3) \times 10^{-6}$
holes covered by absorbing plates	$(1.2 \pm 0.2) \times 10^{-6}$

Table 3.6: Fraction of photons escaping the electronics box as obtained per each geometry inserted in the simulation framework. It is clear how the solution which foresees only absorbing plates covering the circulation holes, shows the lower fraction of photons.

In Tab. 3.6 are reported the results obtained for the different geometries. From the simulations campaign, the design which foresees covering the openings in the electronic box with only absorbing plates both in the lid and in the base is the one with the lower light leakage. The achievement obtained represents an important step in understanding how to produce the next boxes. Currently even other possible geometry solutions are under evaluation as for example implementing a structure around the PoF to shield even more light.

Figure 3.14: Design of the geometry with lower light leakage basing on the simulations results.

Chapter 4

Characterization and selection of DUNE SiPMs

This Chapter describes the down-selection campaign conducted in order to select the best SiPM model for the DUNE FD1 Photon Detection System. As already mentioned in Sec. 3.1.1, the DUNE PDS will use light collector modules coupled to Silicon Photomultipliers (SiPMs) to detect the VUV scintillation light.

The SiPMs for DUNE are custom products by two vendors: Fondazione Bruno Kessler (FBK) and Hamamatsu Photonics K.K. (HPK), specifically optimized for being used DUNE cryogenic conditions. Several prototypes addressing DUNE technical requirements have been produced and accounted in the selection campaign undertaken. In this chapter the features of the different SiPM models, the down-selection criteria, and the outcome of the down-selection procedure will be described.

4.1 DUNE requirements

The DUNE PDS and SiPMs requirements are determined by the working conditions and the physics cases to be studied in DUNE experiment. [45].

Although cryogenic conditions help to drastically reduce the SiPM dark count noise, the thermal stress during the conditioning of the PDS can damage the package of the device or its soldering to the printed circuit board. In the selection of the best model, the devices were required to withstand at least 20 thermal cycles, a number three times larger than the one expected during their operational lifetime.

In FD1, the final configuration of a Supercell envises 48 SiPMs electrically connected in parallel (passively ganged), summing their signal in order to reduce the total amount of readout channels in the experiment. With the configuration

69

mentioned above, a group of SiPMs is biased with the same voltage. Therefore, it is important that the grouped sensors have breakdown voltages (V_{bd}) as similar as possible. Large discrepancies in the values of V_{bd} would imply different gain for the grouped SiPMs and thus, a loss in uniformity in the response of the Photon Detection system.

Given the DUNE scientific goal to study extremely rare events, it is essential to ensure a low level of noise affecting the output signal to allow a low energy threshold and good signal to noise ratio. Therefore, a crucial aspect in selecting the SiPM model is to investigate the different contribution of noise sources to the device response.

SiPMs working in LAr at extremely low temperature as in DUNE, presents low values of dark count rate [46], which represents one of the main noise contribution. The correlated noise as Afterpulsing and direct Crosstalk (Sec. 4.3.4) also have to be studied, to fully characterize their contribution to the overall noise.

A complete list of the specific photosensors features demanded by the experiment is reported in Tab. 4.1.

Considering all the experiment requirements described above, a wide test campaign is necessary to ensure the mechanical and electrical integrity and to fulfill the quality requirements for the devices. The DUNE Single Phase Photon Detection System Consortium is responsible for testing and validating the photosensors which will be then used in DUNE Far Detector PD system.

4.1.1 Features of samples

Two vendors were identified as possible providers of the SiPMs for the PDS of FD1. The two vendors proposed two different technology to be tested in the preproduction phase are:

- Hole Wire Bond (HWB) technology of HPK with a Silicon package;

- NUV-HD-Cryo (Near Ultra Violet-High Density-Cryo) technology of FBK implemented in SMD epoxy resin package.

Different types of these technologies have been produced with area of 6×6 mm². The characteristics of the different sensors for each vendors are reported in Tab. 4.2.

The Hamamatsu **S13360-6050HS-LRQ (S13360-9932)** model is low capacitance device, with 50 μm cell pitch and nominal metallic quenching resistance. The same model samples with a larger cell pitch of 75 μm have been also produced labeled as **S13360-6075HS-LRQ (S13360-9934)**.

Since the recovery time of these devices is quite short ($\sim$30-65 ns) they are prone to afterpulsing events (Sec. 4.3.4) due to the short duration of the pulse

Parameter	Requirement
SiPM dimension and packaging	6x6 mm^2, SMT (Surface Mount Technology)
Cell pitch	50-150 μm
PDE (at 430 nm)	>35%
Window material	Siliconic or epoxidic
DCR (at V$_{op}$, 77 K)	<200 mHz/mm^2
Crosstalk probability (at V$_{op}$, 77 K)	<35%
Afterpulsing probability (at V$_{op}$, 77 K)	<5%
Gain	2-8 $\cdot 10^6$
SiPM recovery time	200-1000 ns
Breakdown voltage V$_{bd}$ spread per PD module (max-min)	<200 mV
Maximum V$_{bd}$ voltage global spread	<2 V (max-min)
Thermal cycles	>20
Signal to noise ratio (per Supercell)	>4

Table 4.1: Specific Requirements for the SiPMs of the FD1-HD Photon Detection System.

Model	Characteristics
HPK S13360-9932 50μm-LQR	Cell pitch 50 μm, low quenching resistance (280 kΩ) at 77 K
HPK S13360-9933 50μm-HQR	Cell pitch 50 μm, high quenching resistance (660 kΩ) at 77 K
HPK S13360-9934 75μm-LQR	Cell pitch 75 μm, low quenching resistance (280 kΩ) at 77 K
HPK S13360-9935 75μm-HQR	Cell pitch 75 μm, high quenching resistance (660 kΩ) at 77 K
FBK NUV-HD-Cryo	Cell pitch 30 μm, Single Trench
FBK NUV-HD-Cryo	Cell pitch 50 μm, Triple Trench

Table 4.2: Different SiPMs prototypes produced by Hamamatsu Photonics (HPK) and Fondazione Bruno Kessler (FBK).

signal. HPK has produced two additional models with a higher quenching resistance, 50 and 75 μm cell pitch to mitigate the effect, labeled as **6050HS-HRQ (S13360-9933)** and **6075HS-HRQ (S13360-9935)**. The recovery time of these models are incremented by tuning the thickness and composition of the metallic resistance, varying between $\sim$115-225 ns.

The NUV-HD-Cryo technology developed by FBK has been previously produced for other experiments and well studied [47]. However, it was never been implemented for 6$\times$6 mm^2 sensors and with the SMD package. A first SiPM model was produced with 30 μm cell pitch and a recovery time of $\tau \sim$400 ns, named **Standard DUNE or Single Trench**. Because the NUV-HD-Cryo trenches are not filled with a metal layer, this technology presents a relatively high crosstalk. A second model was developed and produced, with a triple trench design with the goal of reducing the crosstalk: three SiO$_2$ trenches are used to prevent electrons and photons diffusion to neighbouring cells. As a disadvantage, these samples could present a corresponding loss of the fill factor which is compensated by a larger cell pitch of 50 μm.

A pre-production test campaign, aimed to down-select one sensor per vendor among those proposed, was conducted first on a small-size production batch (25 SiPMs per model), followed by a wider batch of 250 SiPMs per model. In the first production the SiPMs were individually mounted on a package (Fig. 4.1,

top), while in the 250-batch they were mounted in group of six on a same PCB board, as in the final configuration for the PDS of DUNE FD1 (Fig. 4.1, bottom). The sample of both batches have been shared between six different laboratories
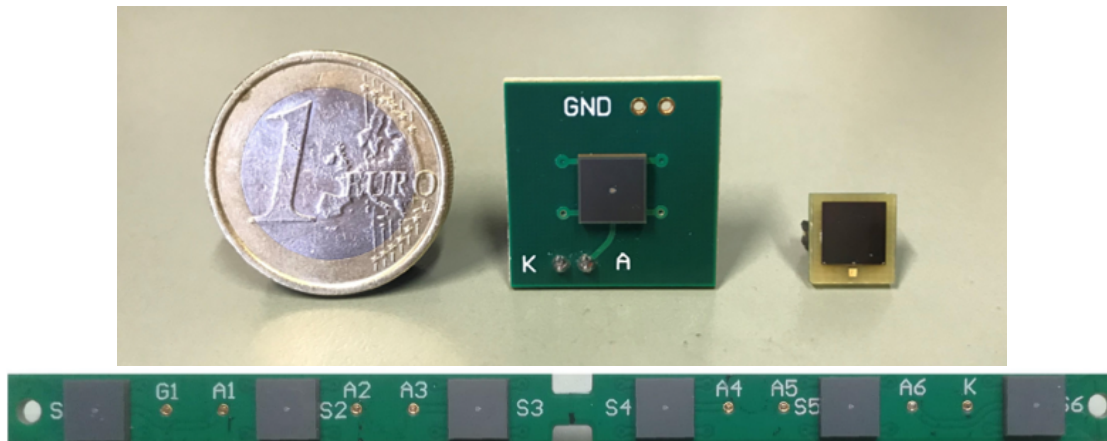

Figure 4.1: Top: single SiPM from the first batch of 25 samples per model: on the left HPK type, on the right FBK. Bottom: array of 6 HPK SiPMs mounted on a PCB with common cathode and single anode per each sensor as in the final design for DUNE FD1-HD.

members of the PDS Consortium, including the Bologna INFN group, in order to crosscheck the measurements.

Basing on the results obtained from the selection, ∼3000 SiPMs for FBK and ∼3000 SiPMs for HPK have been produced, fully characterized and eventually installed in ProtoDUNE-HD at CERN.

The Bologna INFN group is one of the teams in charge of characterizing the devices foreseen for the pre-production phase. During the work of my PhD I was deeply involved in all the tests conducted to identify the optimal SiPM model, actively participating in the measurements campaign and analysis of the results. This was crucial in determining the most suitable device model that met the experiment requirement for sensitivity, noise levels, and overall reliability.

4.2 Measurement procedure and experimental setup

The characterization of the samples has followed a precise protocol I've actively participated in defining and agreed by the Consortium. A description of the testing procedure and experimental setup used is given in this section, distinguishing the case of individually mounted SiPM or array of them.

Testing protocol of single sensors

For the characterization of the sensors at the level of single SiPMs some preliminary tests at room temperature were performed before the first cool down in LN2 to validate the information provided by the vendors. The I-V characteristics in forward and reverse bias were measured at room temperature for all the sensors of the 25-batch. This allow to obtain the SiPM breakdown voltage and quenching resistance and compare them to the data given by the vendors. Then, a first submersion in Liquid Nitrogen was excuted. Since the characteristics of the SiPMs change at 77 K, measurements of the main sensors features were performed again. The sensors reliability to thermal stress was verified in Liquid Nitrogen (LN) over many thermal cycles: the response of the SiPM in terms of reverse I-V curve was tested at 77 K before and after the cycles and the results eventually compared to ensure no significant change in the sensors characteristics.

The test sequence is here summarized:

- preliminary I-V curve in forward and reverse bias at room temperature. The measurement is aimed at providing a direct estimate of the quenching resistance and breakdown voltage;

- I-V curve measured at 77 K at the first bath in Liquid Nitrogen, both in forward and reverse bias;

- 18 consecutive thermal cycles to verify the cryo-reliability and mechanical integrity of the packaging;

- I-V curve measured again at 77 K after the thermal stress, performed in both polarization;

- measurement of the primary Dark Count Rate (DCR) at 77 K during last LN2 bath. Rates below 200 mHz/mm^2 at the 0.5 p.e. threshold is required.

- study of the correlated noise (crosstalk and afterpulsing). DCR and correlated noise was extracted by data from the same acquision.

Testing procedure of SiPMs mounted on boards

In the second batch of 250 samples, the SiPMs are mounted in group of six on a same PCB board, with individual output per each anode of the sensors but a common cathode, allowing to individually test them. The design of the tested board is the same as the final ones for ProtoDUNE-HD and DUNE FD1. The characterization procedure for the 250-batch is the same as in the case of the first batch described above. The only difference adopted stands in the DCR and

correlated noise measurements, which in this case were performed for only a 10% of the SiPMs of each model tested in LN2.

Experimental setup

The different laboratories involved in the tests made use of similar setups with same specifications. A detailed description of the setup I established and used in Bologna is provided below (Fig. 4.2). The system is composed of a small dewar
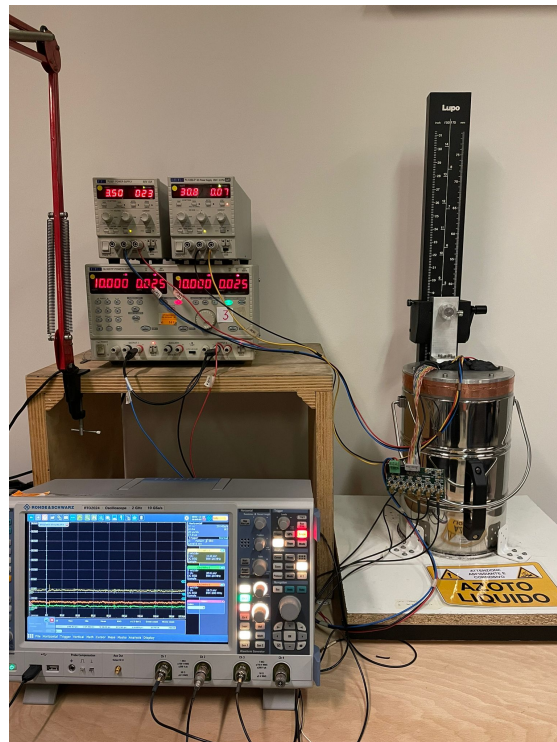
Figure 4.2: Bologna setup as an example of the system used for the measurements. On the right, the dewar filled with Liquid Nitrogen were the samples are allocated and the second stage warm amplifier board. On the left, the output signals connected to a scope for DCR measurements and power suppliers for the amplifiers and samples bias.

($\sim$ 5 liters volume) which can be filled with LN2 and the top opening of the dewar can be closed with a lid to allow measurements in the dark. The plug can be manually moved up and down through a mechanical system. Power and signal cables go inside the dewar through holes drilled in the flange where the light tightness is ensured by black silicone or putty. A support structure is attached to the plug holding a metallic box containing a pre-amplifier and the device under test

(Fig. 4.3, right). The box helps in shielding the amplifier from the environmental electromagnetic noise and also from the Cherenkov light produced by cosmic rays inside the volume of the dewar which would affect the intrinsic Dark Count Rate (DCR) measurement. During the tests of the 250-batch the amplifier used was developed by the Milano-Bicocca group [44], while during the 25-batch tests the Bologna group used an alternative one, based on a SiGe transistor in common emitter configuration with analogous characteristics, developed by its electronic service. For the DCR measurements the output of the amplifier is connected to the input of a digital scope for the data taking. The waveforms are analysed
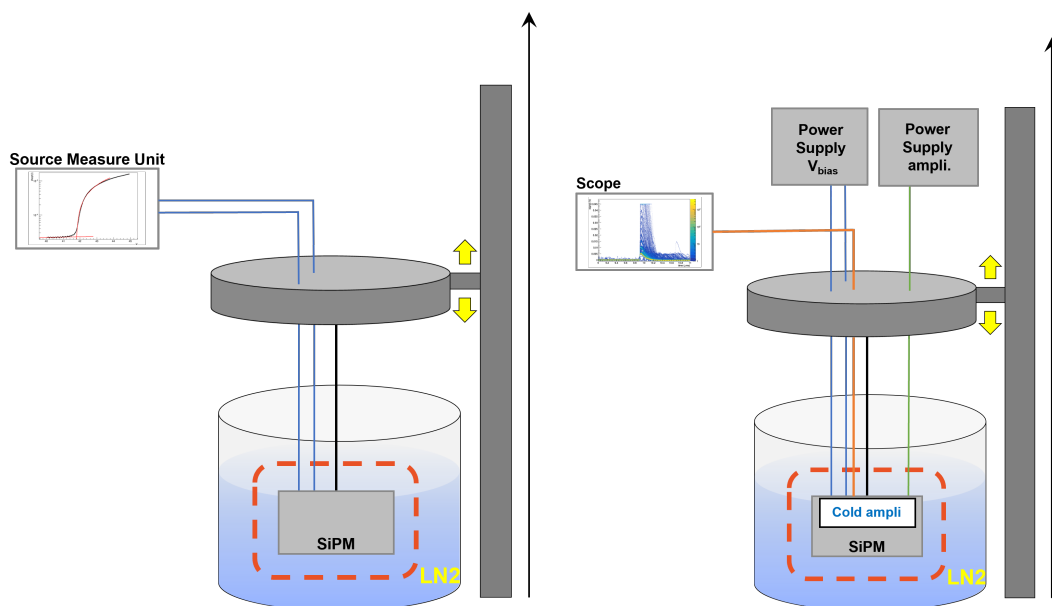

Figure 4.3: Sketch of the experimental setup used for the I-V measurements (left) and for the DCR, correlated noise and gain tests (right).

offline. For accurate measurement of the very low DCR it is crucial to ensure the light tightness of the plug. Placing the test system in a dark room aids in shielding the dewar from external light. The current-voltage characteristics (I-V curves) are obtained by directly connecting the device under test directly to a Keysight B2901A Series precision source/measure unit (Fig. 4.3, left). The relevant specifications of the instrumentation are summarized in Tab. 4.3. During the thermal cycles and all the measurements in Liquid Nitrogen, the temperature was continuously monitored by two platinum resistance termometers (PT100): one attached inside the metallic box at the same level as the SiPM to be tested and the other placed at room temperature. The sensors are readout by an Arduino board connected to the USB port of the oscilloscope. The temperature is recorded every

76

Device	Specifications
Scope	1 GHz bandwidth, 5 Gs/s, 8 bit vertical scale, 10 Msample memory
Source Measure Unit (SMU)	±210 V, Voltage range ±3 A DC and ±10.5 A pulsed, Current range resolution down to 10 fA and 100 nV
Source meter cable	less than few pA loss

Table 4.3: Relevant specifications of instrumentation used for the measurements.

0.5 second and a real time temperature-time plot is created by using a python script.

4.3 Measurements

The devices delivered from the vendors to the Bologna group are listed in Tab. 4.4 for the 25 batch and Tab. 4.5 for the 250 batch. All the samples from the 25 batch that arrived in Bologna were fully characterized according to the planned procedure, but only the I-V curves were done for a smaller number of samples from the 250 batch.. In the case of the HPK SiPMs, we performed the I-V curves at room temperature for all the boards of each model, while I-V curves at 77 K have been conducted for only 3 boards out of 10 for the 50 μm cell pitch model and for 2 boards out of 10 for the 75 μm cell pitch model. In the case of the FBK samples, only 5 boards out of 10 for both model were measured in their I-V curves at room temperature and in Liquid Nitrogen. The missing boards, after they had initially been delivered to Bologna, were sent to other labs of the Photosensor Working Group for some Supercell tests [48][49]. Hence only a partial characterization of these samples was possible.

4.3.1 Reliability to cryogenics cycles

Due to the LAr temperature to which the SiPMs will operate, a key aspect to test during the down-selection tests is their cryo-reliability. Thermal gradients stress the devices at the level of features, bonding and packaging. To verify their mechanical integrity, the sensors with their packages have been tested in Liquid Nitrogen over many consecutive thermal cycles.

Vendor	Cell pitch (μm)	number of boards
FBK	30	4
	50	5
HPK (LQR)	50	2
	75	7

Table 4.4: SiPMs samples of the 25-batch received and fully characterized in Bologna

			T_{room}	T_{cryo}	
Vendor	Cell pitch (μm)	boards received	IV	IV (1st)	IV (20th)
FBK	30	10	5	5	3
	50	10	5	5	3
HPK (LQR)	50	10	10	10	2
	75	10	10	2	2

Table 4.5: SiPMs samples of the 250 batch received and tested in Bologna

In order to verify that after the thermal cycles the SiPMs are still working within the nominal requirements, the measurements of the devices features shall be carried out before and after the thermal tests.

Basing on the protocol I've contributed in developing, the thermal cycle is composed of three phases (Fig. 4.4): exposing the sensor to LN2 vapors for ∼8 minutes, submerging the sensor in the liquid for ∼11 minutes, then a phase in which it is pulled up and again exposed to LN2 vapors for ∼8 minutes and finally warmed up at room temperature until it thermalizes to the temperature of the lab. Such thermal cycle should last for ∼30 minutes. Each sensors had to be tested over ∼20 thermal cycles, which implied a total time of at least ∼500 minutes per SiPM (∼ 8 hours). The precision in the thermal profile of the phases has been possible thanks to the temperature monitoring with the PT100.
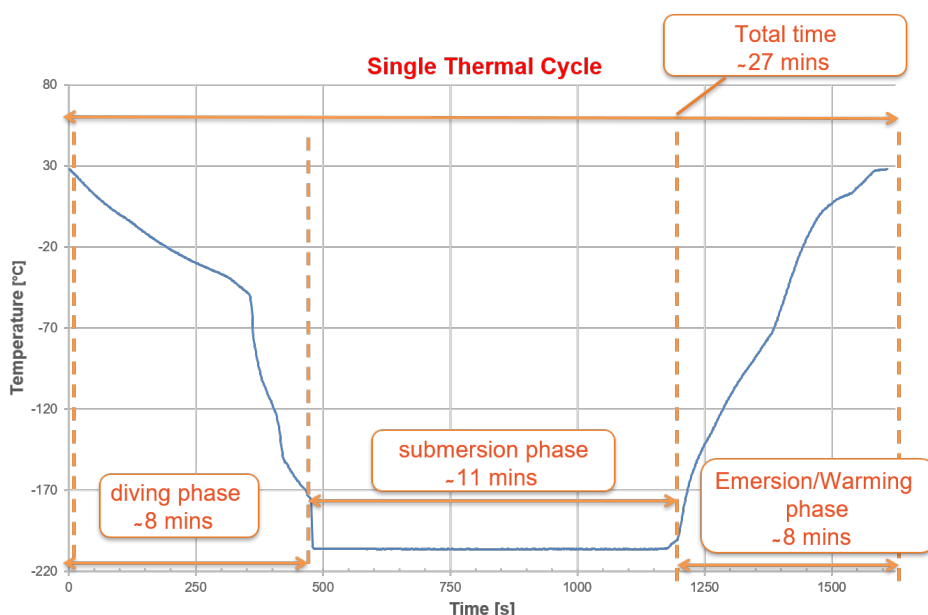

Figure 4.4: Temperature profile over time of a single thermal cycle. The different phases are shown along with their duration and total time of a cycle.

4.3.2   Breakdown voltage and quenching resistance

The current-voltage relation of the SiPMs known as I-V curve is a fundamental characteristic tested during the validation. From the I-V curves it is possible to obtain features as the breakdown voltage (V_{bd}) and the quenching resistance (R_q) and compare their values with those required by the experiment.

The V_{bd} is estimated from the I-V curve of the SiPM in reverse bias polarization as the intersection point between a linear fit on the initial linear region of
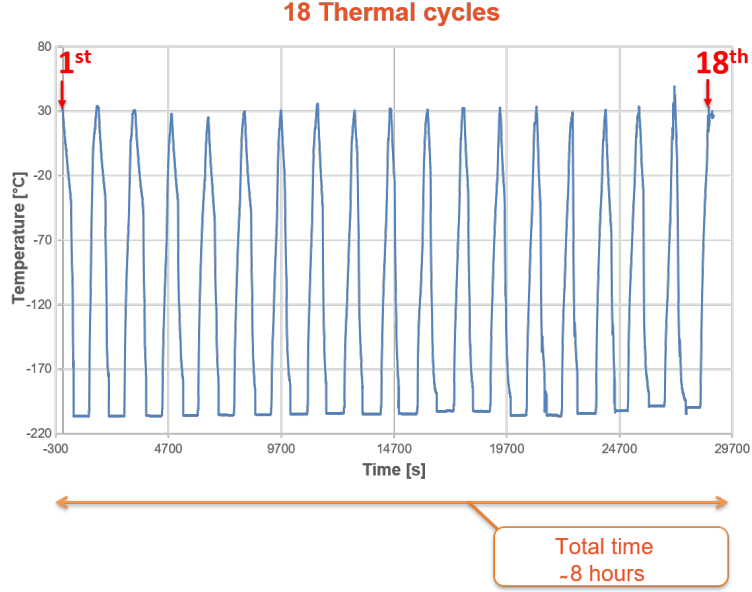
Figure 4.5: Temperature profile over time of 18 consecutive thermal cycles. The total requirements of 20 cycles is reached taking into account each submersion in LN2 to obtain IV curves before and after the thermal stress tests.

the curve and a fit on the following exponential region. This method was used during measurements of the 25-batch while for the next batch the parameters was estimated with a different method, agreed by the Consortium, exploiting the first derivative of the SiPM I-V curve ($\frac{dI}{IdV}$, also known as variation rate). The maximum of this curve was considered as the breakdown voltage of the sensor. Fig. 4.6 shows different methods used to obtain the V_{bd} of a SiPM.

In a forward biased configuration, the current generated in the device is initially approximately zero then, a limited exponential increasing occurs, followed by a linear growing of the current with the applied voltage. The SiPMs acts as a diode in series with the quenching resistor and so the measured current as a function of the voltage is inversely proportional to the equivalent quenching resistance of the SiPM. To obtain the parameter a linear fit is applied to the linear region and the best estimate of the quenching resistance R_q of a single microcell is extracted as the inverse of the angular coefficient of the line:

$$R_q = \left(\frac{1}{m}\right) \cdot N_{cells} \tag{4.1}$$

where m is the angular coefficient of the line and N_{cells} is the total number of cells of the SiPM.

The I-V curves of the samples have been measured for all the SiPMs of the 25-batch both at room temperature to test the sensor initial condition and in liquid
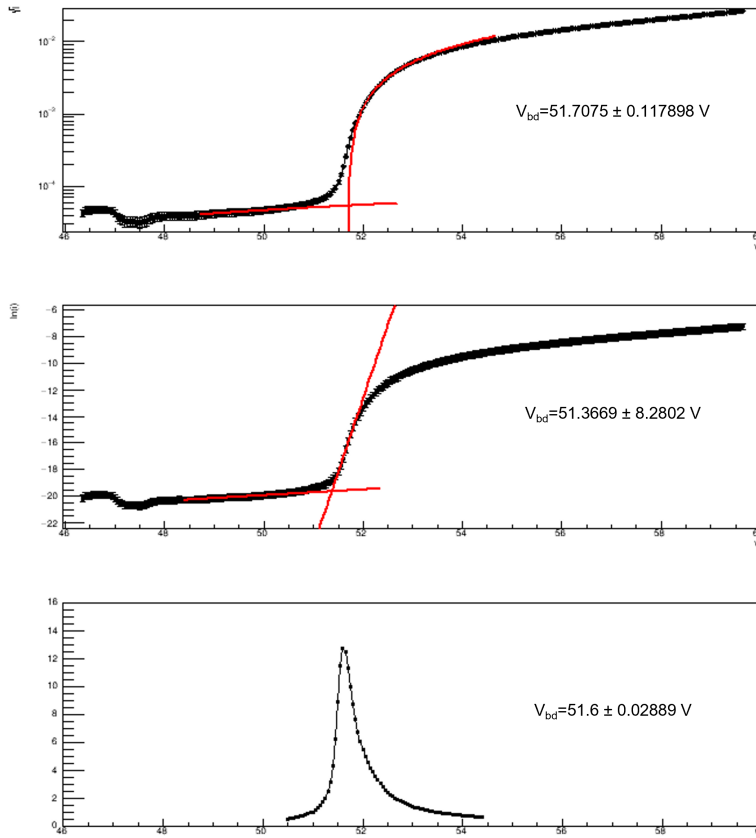
Figure 4.6: Examples of different models to obtain the value for the breakdown voltage of a tested SiPM from its I-V curve in reverse polarization. Top: value is estimated as the intersection between a linear and exponential fit of the two correspondent region of the curve. Center: V_{bd} is estimated as the intersection of two linear fit applied in small ranges of the two different regions of the curve. Bottom: breakdown voltage is obtained as the maximum of the first derivative of the I-V curve in reverse biased.

nitrogen (77 K) before and after the thermal stress tests.

Experimental results

The main characteristic of the samples tested are expected to change at the two temperature of reference, due to their specific technologies. The breakdown voltage of a SiPM decreases with the temperature decreasing, while the quenching resistance increases at low temperature.

In Tab. 4.6 are reported the 25-batch results for the measurements I obtained

from the I-V curves performed at room temperature. This first phase was used to validate the test setup and ensure the initial working condition of the SiPMs.

25-batch			T_{room}	
Vendor	Cell pitch (μm)	ID	R_q (Ω) ± 1	V_{bd} (V) ± 0.2
FBK	30	14	25	33.1
		15	25	33.0
		19	21	33.1
		20	32	33.1
FBK	50	21	61	32.9
		22	61	32.8
		23	82	33.9
		24	86	33.9
		25	88	33.9
HPK	50	18	28	51.9
		19	27	51.1
HPK	75	22	44	52.0
		23	45	51.9
		25	54	51.5
		26	45	51.7
		27	46	51.6
		28	44	52.1
		29	44	51.9

Table 4.6: Results for the I-V measurements at room temperature, of the FBK and HPK SiPMs for the 25-batch.

Following the protocol, I then tested the samples in Liquid Nitrogen. At the first submersion in the bath I performed the I-V curves and the obtained values were considered as the referenced ones. Then the measurements were performed

again after 20 monitored thermal cycles as explained in Sec. 4.3.1. Tab. 4.7 reports the measurements performed in Liquid Nitrogen and a comparison of the results, before and after the thermal stress tests. All the samples validated have been considered not subjected to any particular changes that could affect their performance in satisfying the requirements.

As shown in Tab. 4.6 and Tab. 4.7, the main SiPM parameters change from T_{room} to T_{cryo}: for HPK the R_q values at 77 K increase $\sim$ twice that at room temperature, while the FBK SiPMs have values of R_q at 77 K that increase by a factor of $\sim$ four compared to that at room temperature. For what concerns the value obtained for the breakdown voltage, in the case of the HPK it decreases of $\sim$ 10 V, while in the FBK case of $\sim$ 6 V.

Concerning the 250-batch, the I-V curve measurements at room temperature were performed for all the received samples. An example of comparison for HPK sensors between the vendor data and our data for the V_{bd} measured at room temperature is reported in Fig. 4.7. After this initial test, part of the arrays were requested and sent to other labs of the PDS Working Group, in order to perform some Supercell tests. Due to this, only the remaining samples were validated through the thermal stress tests and their performances evaluate after the cycles. The results are reported in Tab. 4.10 and 4.11. All the tested arrays were considered satisfying the specifications passing all the tests.
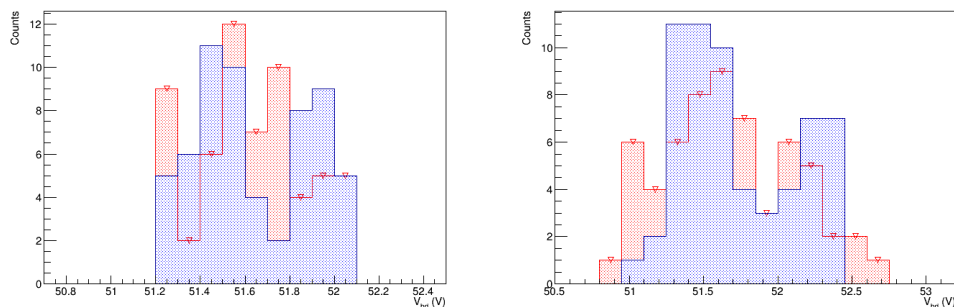

Figure 4.7: Comparison of the V_{bd} distribution measured at T_{room} between the vendor's data (blue) and the data from the Bologna group (red), for the HPK samples of the 250-batch with 50 μm cell pitch on the left and 75μm on the right.

4.3.3 Dark Count Rate (DCR)

Noise sources in SiPMs can be either of primary type or correlated one. The first mainly arises from charge carriers thermally originated in the sensitive volume of a SiPM cell: under the effect of the applied high electric field, they can trigger an avalanche even in absence of light. This noise is hence named Dark Current. The

| Vendor | Cell pitch (μm) | ID | T$_{cryo}$ (before) | | T$_{cryo}$ (after) | | | |
			R$_q$ (Ω) ±1	V$_{bd}$ (V) ±0.2	R$_q$(Ω) ±1	V$_{bd}$ (V) ±0.2	ΔR$_q$ (Ω) ±1	ΔV$_{bd}$ (V) ±0.2
FBK	30	14	ND	ND	107	27.0	ND	ND
		15	ND	ND	118	27.1	ND	ND
		19	92	27.2	96	27.1	4	0.1
		20	127	27.2	127	27.1	0	0.1
FBK	50	21	283	27.0	280	27.1	3	0.1
		22	294	27.0	295	27.0	1	0.0
		23	319	27.0	311	27.0	8	0.0
		24	308	27.0	311	27.0	3	0.0
		25	478	27.0	476	27.0	2	0.0
HPK	50	18	57	41.9	67	41.8	10	0.1
		19	57	42.1	63	42.1	6	0.0
HPK	75	22	89	42.1	95	42.1	6	0.0
		23	91	41.9	92	41.9	1	0.0
		25	88	41.7	101	41.9	13	0.2
		26	93	41.7	98	41.7	5	0.0
		27	87	41.7	96	41.9	9	0.2
		28	85	41.9	85	41.7	0	0.2
		29	90	42.0	90	41.7	0	0.0

Table 4.7: Results for the I-V measurements at cryogenic temperature, of the FBK SiPMs for the 25-batch. The SiPMs 14 and 15 of FBK arrived already tested by the vendor with 18 thermal cycles, hence it was not possible to measure the DCR before the thermal tests.

Vendor	Cell pitch (μm)	ID	R_q (Ω) ± 1	V_{bd} (V) ± 0.03
			T$_{room}$	
FBK	30	1	18	33.01
		3	19	33.43
		5	18	33.09
		7	21	32.93
		9	17	33.10
FBK	50	2	51	32.92
		4	53	32.93
		6	49	32.94
		8	57	32.81
		10	49	32.93

Table 4.8: Results for the I-V measurements at room temperature, for the FBK SiPMs of the 250-batch. The values reported for R_q and V_{bd} are the averaged on the measurements for 6 SiPMs on same array.

correspondent resulting signal is identical to that produced by one photoelectron, creating thus a noise source at the single photon level. A similar mechanism can also be originated by tunneling in the high field region. At room temperature the Dark Current is dominated by the thermal contribution while at cryogenic temperature as that of Liquid Nitrogen or Liquid Argon the noise is greatly reduced and mostly dominated by tunneling. This noise can be often neglected for measurements of high amplitude signals, while can significantly affect the detection of very small light signals (of one or few photoelectrons) especially at room temperature at which the dark count rate is expected to be ~ 100 kHz/mm^2. [50, 51]. The effect can be reduced by operating at lower temperatures or decreasing the volume of the depletion region. At liquid Nitrogen temperature for example, the effect is of the order of $\sim$Hz/mm^2. Considering the working condition of the DUNE SiPMs, it is crucial to study in a cryogenic environment, the impact of the Dark Count Rate on the readout signal.

To investigate this SiPMs primary noise, I performed measurements at 77 K in our setup in dark, ensuring the absence of real signals due to external pho-

Vendor	Cell pitch (μm)	ID	R_q (Ω) ± 1	V_{bd} (V) ± 0.03
			T_{room}	
HPK	50	32	30	51.37
		33	30	51.35
		34	31	51.94
		35	31	51.83
		36	30	51.63
		37	31	51.88
		38	30	51.57
		39	30	51.34
		40	31	51.67
		119	31	51.63
HPK	75	52	45	51.52
		53	49	51.57
		54	54	51.53
		55	49	52.12
		56	44	51.65
		57	52	51.86
		58	51	51.88
		59	44	51.11
		60	50	51.56
		61	51	51.79

Table 4.9: Results for the I-V measurements at room temperature, for the HPK SiPMs of the 250-batch. The values reported for R_q and V_{bd} are the averaged on the measurements for 6 SiPMs on same array.

Vendor	Cell pitch (μm)	ID	T_{cryo} (before)		T_{cryo} (after)			
			R_q (Ω) ± 1	V_{bd} (V) ± 0.03	R_q (Ω) ± 1	V_{bd} (V) ± 0.03	ΔR_q (Ω) ± 1	ΔV_{bd} (V) ± 0.03
FBK	30	1	76	26.88	75	26.84	1	0.1
		3	75	26.86	-	-	-	-
		5	70	26.81	70	26.78	0	0.03
		7	78	26.78	-	-	-	-
		9	77	26.78	78	26.77	1	0.01
FBK	50	2	246	26.77	245	26.77	1	0
		4	239	26.77	-	-	-	-
		6	229	26.83	230	26.76	1	0.07
		8	259	26.76	-	-	-	-
		10	240	26.76	240	26.77	0	0.01

Table 4.10: Results for the I-V measurements at cryogenic temperature, for the FBK SiPMs of the 250-batch. The values reported for R_q and V_{bd} are the averaged on the measurements for 6 SiPMs on same array. Some values are missing because part of the samples was sent to other labs for Supercell tests, before the conclusion of the validation.

tons in order to identify only the contribution of the noise. The samples under test were mounted on the mechanical support, submerged in Liquid Nitrogen and reversed biased at the correspondent operating voltage depending on the model. The amplified output signal was readout with an oscilloscope and data stored in binary format. The waveforms were acquired inside a time window of 5 μs, with a division of 500 ns/div and a sampling of 1 GS/s. A trigger threshold was set at 0.5 photoelectron (p.e), the time acquisition lasts for ~1 hour. Data were converted in ROOT file and eventually analyzed by means of a C++ software I've developed. An example of a waveform corresponding to a single p.e.is reported in Fig. 4.8 (left), while an example of the persistency of several waveform acquired during a test run is shown in Fig. 4.8 (right).

Vendor	Cell pitch (μm)	ID	T_{cryo} (before)		T_{cryo} (after)			
			R_q (Ω) ± 1	V_{bd} (V) ± 0.03	R_q (Ω) ± 1	V_{bd} (V) ± 0.03	ΔR_q (Ω) ± 1	ΔV_{bd} (V) ± 0.03
HPK	50	32	59	41.57	NA	NA	-	-
		33	59	41.58	NA	NA	-	-
		34	61	41.96	NA	NA	-	-
		35	60	41.78	NA	NA	-	-
		36	61	41.61	NA	NA	-	-
		37	62	41.89	NA	NA	-	-
		38	62	41.61	NA	NA	-	-
		39	59	41.43	NA	NA	-	-
		40	62	41.71	61	41.70	1	0.01
		119	61	41.63	73	41.62	12	0.02
HPK	75	52	89	41.57	93	41.55	4	0.02
		53	93	41.86	94	41.85	1	0.01

Table 4.11: Results for the I-V measurements at cryogenic temperature, for the HPK SiPMs of the 250-batch. The values reported for R_q and V_{bd} are the averaged on the measurements for 6 SiPMs on same array. Some arrays are missing of some values after the thermal cycles since they are part of those samples sent for Supercell tests before the conclusion of the validation.

Experimental results

In the tests I conducted, I considered the SiPM DCR as the ratio between the number of waveforms recorded and the time acquisition of the measurements. To characterize the Dark Count Rate, a threshold scan can be performed at different increased voltage thresholds. The curves obtained are called *staircase curves* (Fig. 4.9) and the overall noise rate can also be obtained by fitting the curve with a constant function in the region of the first plateau ("step").

The DCR results obtained from the data of the 25-batch are reported in Tab. 4.12 for the FBK and HPK samples and compared before and after 20 thermal cycles.
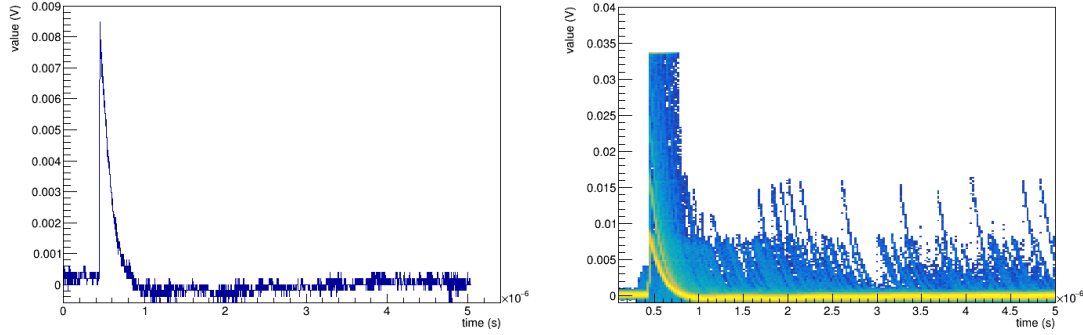
Figure 4.8: Left: example of waveform corresponding to a single p.e.. The signal is acquired in a time window of 5 μs. Left: persistency of several waveforms on a same data acquisition. In the tale of the primary signal, it is visible the presence of spurius ones due to afterpulsing.

For the SiPMs of the 250-batch only a 10% of those samples remained in Bologna and tested in LN2 were also characterized in their DCR. In Tab. 4.13 are reported the results of the measurements. The Single Trench (30μm cell pitch) FBK samples were biased with a +4 OV and the Triple Trench (μm cell pitch) with +4.5 OV corresponding to 45% of PDE of the sensor, while all the HPK samples were biased with +3 OV as the vendor's recommended operating voltage. Even in the case of the 250-batch all the SiPMs measured fulfill the DUNE requirements in terms of DCR values.

4.3.4 Correlated noise

Along with an evaluation of the DCR of the samples tested, I also studied the so called Correlated noise. From the waveforms analysis of the same data set acquired to evaluate the primary noise, it was possible to study the optical Crosstalk (CT) probability and the Afterpulsing (AP) probability in a SiPM. The first one is the probability of a photon, emitted by accelerated electrons during a Geiger discharge inside a cell, to migrate to neighbouring cells and trigger a second spurious avalanche. The latter is the probability that a charge carrier can be trapped by impurities inside the Silicon crystal lattice and released after a characteristic time: this can produce a delayed pulse. Considering these two definitions, their probabilities were evaluated from measurements performed in the dark and at 77 K. At such low temperature and in absence of light, the DCR is low enough to assume that any signal coming from the SiPM corresponding to more than a single p.e. is generated by optical crosstalk. Basing on this assumption, the CT probability was estimated as the ratio of events above one and a half p.e. divided by the total
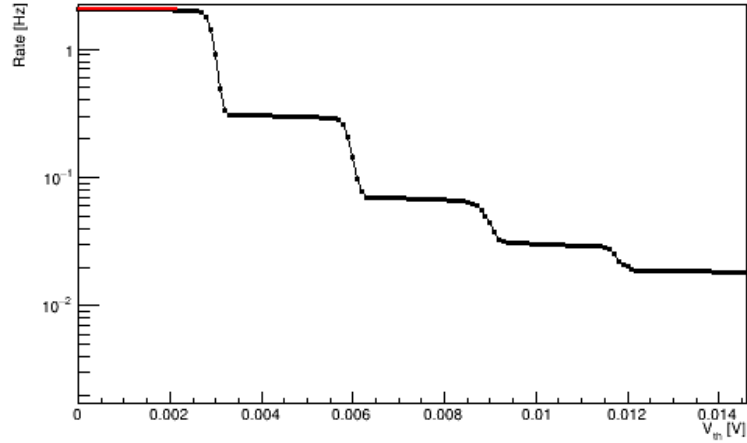
89

Figure 4.9: Example of the threshold scan at different voltage thresholds (*staircase curves*) performed at 77 K. The DCR is estimated by fitting with a constant function the first step of the curve, the results of the fit is divided for the SiPM surface and so expressed in mHz/mm^2.
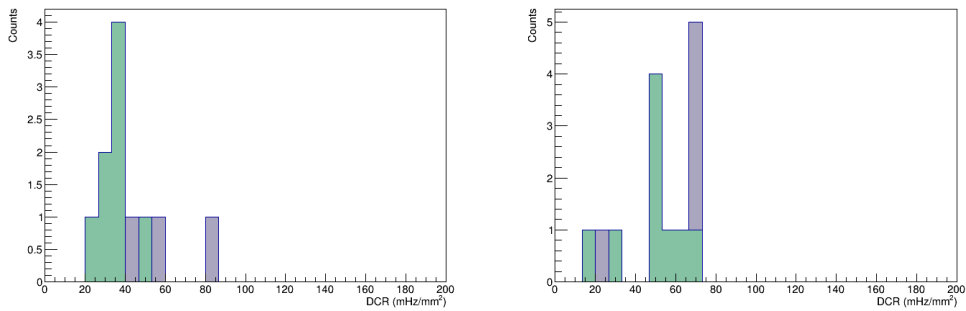

Figure 4.10: DCR measurements distribution for the 25-batch in lilac before the thermal cycles and in green after, for the HPK samples (left) and FBK samples (right). All the measurements are below the requirements of 200 mHz/mm^2.

90

Vendor	Cell pitch (μm)	ID	T_{cryo} (before) DCR (mHz/mm^2) ± 1	T_{cryo} (after) DCR (mHz/mm^2) ± 1
FBK	30	14	NA	47
		15	NA	28
		19	69	72
		20	24	16
FBK	50	21	73	61
		22	73	56
		23	61	48
		24	67	51
		25	72	51
HPK	50	18	44	32
		19	58	36
HPK	75	22	34	21
		23	33	27
		25	82	38
		26	39	38
		27	47	48
		28	NA	34
		29	61	62

Table 4.12: Results for the DCR measurements at cryogenic temperature for the FBK and HPK samples of the 25-batch. The SiPMs 14 and 15 of FBK arrived already tested by the vendor with 18 thermal cycles, hence it was not possible to measure the DCR before the thermal tests. The missing value for ID 28 of HPK before the tests is due to a very noisy acquisition, it was however considered sufficient to verify if the DCR requirement was satisfied after the thermal cycles.

Vendor	Cell pitch (μm)	ID	anode	T$_{cryo}$ (before) DCR (mHz/mm^2) ±1
FBK	30	1	3	21
			4	38
			5	31
FBK	50	2	3	78
			4	115
			5	101
HPK	50	32	1	54
			2	52
			3	55
			4	177
			5	95
			6	53
HPK	75	52	2	55

Table 4.13: Results for the DCR measurements at cryogenic temperature for the FBK and HPK samples of the 250-batch. The SiPMs were baised at their operational overvoltages which for FBK correspond to +4 OV in the case of Single Trench samples and +4.5 OV for the Triple Trench ones, while the HPK SiPMs were all biased at +3 OV. The measurements are only for the 10% of the samples remained in Bologna at tested in Liquid Nitrogen. The values were measured only before the thermal stress test since shortly after the thermal cycles they were shipped for Supercell tests.

number of events, with a trigger threshold set to half a p.e.. The AP probability was instead calculated as the number of events with one or more peaks in a time window of 4 μs after the main pulse, divided by the number of main pulses.

Experimental results

From the analysis I conducted on the data taken, I obtained values for the CT and AP probability for all the samples of the 25-batch, before and after 20 thermal cycles. The results are reported in Tab. 4.14. The measurements do not show any significance changes in the SiPMs characteristics after the thermal stress tests and all the samples fulfill the DUNE requirements for what concerns the correlated noise. In the case of the 250-batch SiPMs, I performed measurements of CT and AP probability for only a 10% of the samples tested in LN2. The results are shown in Tab. 4.15. All the sensors fulfill even in this case DUNE requirements.

4.3.5 Unexpected observation of bursts of signals

During measurements of the Dark Count Rate, an unexpected behaviour was soon observed. In some of the measurements the rate fluctuated randomly instead of increasing as the overvoltage increased [52]. By means of waveforms analysis it was possible to identify different components populating the DCR measurements. Fig. 4.11 (top) shows the SiPM pulse amplitude as a function of the time difference between consecutive events. It is clearly visible a population of events correspondent to the primary dark signal with one p.e. amplitude and the typical time difference of the order of s, and a second cluster of events with same amplitude but time difference between [0.1-10] ms, well separated from Afterpulsing or Crosstalk populations. Fig. 4.11 (bottom) shows the time distribution of events with single p.e. : the right component corresponds to the expected standard DCR, and the left one to the unexpected cluster of events. With a more detailed waveforms analysis it was possible to identify events with a main large pulse of several photoelectrons amplitude followed by hundreds of single photoelectrons with a time separation of the order of ms, named burst. Fig. 4.12 (left) shows an example of this phenomenon: a high amplitude main signal trace, followed by what is the start of a trains of smaller signals. Fig. 4.12 (right) shows the time interval between consecutive events as a function of the events id: this reveals regions where all events are delayed by a few seconds and regions that look like valleys where events happen quickly, called bursts. Different technique have been developed to identify the bursts and remove their contribution from the dark rate [52]. The one I used during the analysis performed was based on the identification of burst events one by one. For each acquired waveform, I identified consecutive events separated by short time interval but still inside a maximum time window of ~hundreds ms then, in order to distinguish them from the expected afterpulsing contribution, their number was compared with a defined threshold (N_{min}) set to 5. If the amount of events recorder was larger than this threshold in the specified time interval, then a train of burst was found.

Vendor	Cell pitch (μm)	ID	T_{cryo} (before)		T_{cryo} (after)	
			AP (%)	CT (%)	AP (%)	CT (%)
FBK	30	14	NA	NA	3±0.2	11.5±2.3
		15	NA	NA	3±0.2	17.2±0.5
		19	4±0.2	16.2±0.4	2±0.2	16.8±2.3
		20	4±0.2	24.1±0.6	3.3±0.1	22±2.2
FBK	50	21	2.0±0.2	13.5±0.4	2.7±0.2	13.8±0.4
		22	3.9±0.2	13.6±0.4	3.7±0.3	14.2±0.4
		23	2.8±0.2	13.4±0.4	4.2±0.3	14.7±0.5
		24	3.2±0.2	12.9±0.4	5.6±0.3	14.1±0.4
		25	2.7±0.2	13.5±0.4	4.2±0.2	13.3±0.4
HPK	50	18	3.1±0.2	7.2±0.4	3.8±0.3	7.9±0.4
		19	13.4±0.4	15.1±0.5	4.8±0.3	6.5±0.3
HPK	75	22	3.6±0.2	9.1±0.3	4.2±0.4	12.5±0.6
		23	4.2±0.3	15±0.4	3.1±0.3	13.7±0.6
		25	6.4±0.3	14.4±1	4.9±0.5	17.8±0.9
		26	6.2±0.2	17±0.4	5.2±0.3	15.5±0.5
		27	4.7±0.3	17.7±0.4	4.7±0.2	14.5±0.5
		28	ND	ND	5.4±0.4	15.1±0.5
		29	5.0±0.2	10.7±0.3	4.4±0.3	10.8±0.4

Table 4.14: Results for the Afterpulsing and Crosstalk probability at cryogenic temperature for the FBK and HPK samples of the 25-batch. The SiPMs 14 and 15 of FBK arrived already tested by the vendor with 18 thermal cycles, hence it was not possible to measure the AP and CT before the thermal tests. The missing value for ID 28 of HPK before the tests is due to a very noisy acquisition, it was however considered sufficient to verify if the correlated noise requirement was satisfied after the thermal cycles.

Vendor	Cell pitch (μm)	ID	anode	T_{cryo} (before) AP (%)	T_{cryo} (before) CT (%)
FBK	30	1	3	1.5±0.2	8.9±0.6
			4	1.4±0.2	9.6±0.6
			5	1.6±0.3	9.2±0.8
FBK	50	2	3	1.7±0.2	13.3±0.4
			4	1.6±0.1	13.0±0.4
			5	1.3±0.1	12.8±0.4
HPK	50	32	1	2.3±0.4	3.6±0.4
			2	1.8±0.3	3.7±0.3
			3	0.9±0.2	2.7±0.4
			4	0.5±0.1	2.1±0.2
			5	0.6±0.1	1.9±0.3
			6	1.2±0.3	3.1±0.4
HPK	75	52	2	1.4±0.7	9.3±3.1

Table 4.15: Results for the Afterpulsing and Crosstalk probability at cryogenic temperature for the FBK and HPK samples of the 250-batch. The measurements are only for the 10% of the samples remained in Bologna at tested in Liquid Nitrogen. The values were measured only before the thermal stress test since shortly after the thermal cycles they were shipped for Supercell tests.
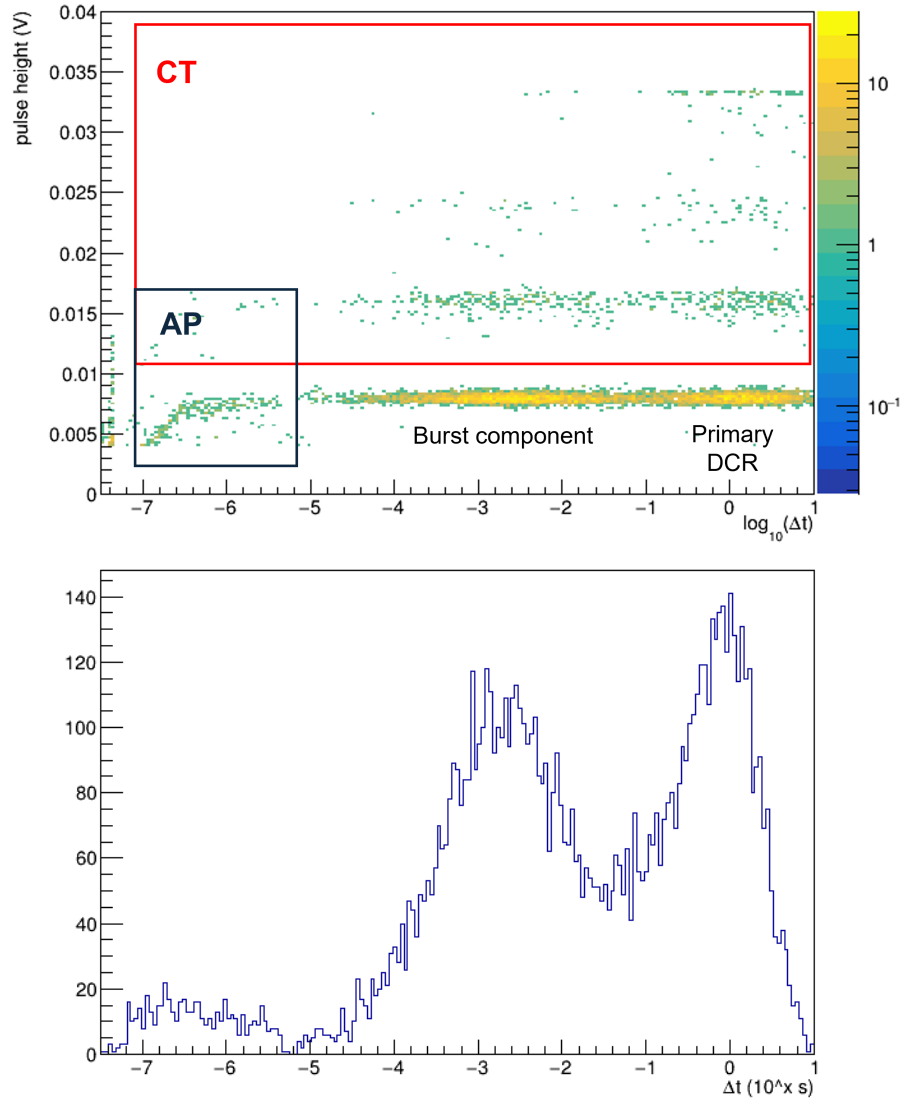
Figure 4.11: Top: SiPM pulse amplitude and relative frequency as a function of the time difference between consecutive events. Different regions of cluster of events are visible, correspondent to primary DCR, Crosstalk and Afterpulsing. Bottom: time difference distribution between events for the contribution measured during DCR data taking. The left population is the one populated by burst events, the right one is the primary DCR.

The burst phenomenon has been also studied by comparing the SiPM models proposed for DUNE with ones with different packaging. SiPMs with silicon or
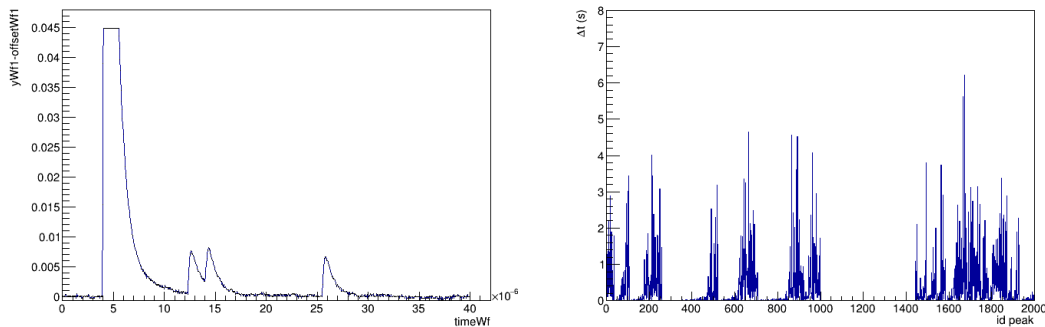
Figure 4.12: Left: example of the burst phenomenon investigated. In the signal trace over time a high pulse saturating the scale anticipates a burst of lower signals close in time. Right: time difference between consecutive events as a funcion of the number of event number (id Peak). The regions with valleys correspond to intervals interested by close burst of signals.

epoxy coating, with hole wire bond or through silicon via, have shown these bursts of events. However, this behavior was not observed in the models which are ceramic mount SiPMs with a lateral bond. [53]. The investigation of the phenomenon was an interesting opportunity, however its nature was considered not affecting the DUNE physics performance since, even including its contribution in the rate of dark pulses, the result is below the DUNE DCR specification of 200 mHz/mm^2 per sensor [52].

4.4 Downselection results

The results obtained by the Bologna group during the characterization campaign to which I participated, among with the data of all the other labs involved, were used in the selection of the best SiPM model for the DUNE experiment. The PDS consortium identified a figure of merit (FoM) basing on the evaluation of the SiPM performance in gain, crosstalk, afterpulsing and DCR at 77 K. The evaluation of this FoM was obtained by the product of correlated noise (crosstalk + afterpulse) times the DCR divided by the gain. The sensor with the lowest value of this parameter is the one with best performance.

For the HPK samples, the selected model basing on the results of the campaign is the HPK S13360-9935 with 75μm cell pitch and high quenching resistance (HQR). Its FoM shows the advantages of a high gain thanks to a large cell pitch, while the HQR ensures a low impact of the afterpulsing in the recovery time of the cell.

Among the FBK samples, the Triple Trench ones with 50μ cell pitch, are those

selected for the DUNE experiment. For these samples the values obtained in Bologna for the CT are comparable to those with Single Trench however, even in their case a larger cell pitch allowed higher gain, while higher quenching resistance makes them less affected by afterpulsing, justifying hence their preference.

Both vendors have been selected to partecipate in the production of all the SiPMs eventually installed in ProtoDUNE PDS, and in the mass production of samples for the first module of DUNE Far Detector.

Chapter 5

System for cryogenic characterization and tests results

The results obtained from the downselection campaign described in Chapter 4, have led to the production of the SiPMs for the Photon Detection System (PDS) of ProtoDUNE Horizontal Drift (HD) and eventually of the first module of DUNE Far Detector (FD1). A characterization of both the productions was demanded, in order to verify their performances according to the experiment requirements. Considering the amount of samples to be tested in both batches ($\sim$4000 SiPMs for ProtoDUNE, $\sim$300000 for FD1), the development of a semi-automated validation facility is mandatory.

From 2021 I participated in the realization and optimization of a custom system, designed to characterize and test a large number of SiPMs in a cryogenic environment.

The commissioning of the system ended in 2022 with the test of all the sensors now installed in the PDS of ProtoDUNE HD. After this successfully operation of the apparatus, the facility has been replicated in other labs of the PD Consortium that joined the mass test campaign.

In this Chapter, a description of the apparatus developed and installed in Bologna is given, along with the results obtained for the SiPMs tested for the DUNE prototype during the system commissioning phase. All the data acquired for the production of FD1 PDS, updated up to the beggining of 2024, are also reported.

5.1 Testing protocol and system description

The totality of the DUNE SiPMs is validated among all the labs involved in the campaign using the system later described and basing on a prescribed procedure.

The sequence of measurements foreseen by the mass-test campaign is the following:

- I-V curves performed at room temperature to ensure the initial working condition of all the samples;

- I-V curves of all the SiPMs at 77 K at the first submersion;

- thermal stress tests composed of 2 consecutive cycles of submersion-emersion phases to validate the cryo-reliability of the sensors;

- I-V curves measured again in LN2 after the thermal cycles to check the functioning of the samples and evaluate possible changes in their features;

- I-V curves at the last submersion in complete dark environment, performed over an extended range of overvoltage, to check anomalies in the dark current;

- Dark Count Rate measurements in dark environment during the last submersion to verify that the overall noise contribution is within the DUNE requirements. Only a measurement of the rate is demanded and not a complete characterization through waveform analysis.

A 10% of the total samples together with the arrays out of specification are sent to other labs of the PD Consortium and fully characterized in terms of correlated noise.

The apparatus developed by the joint effort of the Bologna INFN and the University of Ferrara groups, is able to test up to 120 SiPMs in parallel following a specific procedure.

The system is composed of a black box hosting the mechanics and the front-end electronics. Some LEDs are mounted on the upper structure of the black box and used to provide a controlled light source during measurements at cryogenic temperature. For the tests at 77 K a 55 lt dewar filled with Liquid Nitrogen is used, equipped with an automated refill system and level monitoring. An aluminum flange is attached to a vertical movable semi-automated mechanical stage and used as a lid to the dewar. On the top of the flange (Fig. 5.1, 2) the warm front-end electronics is mounted while on the bottom, it is attached the supporting structure where the samples under test are located (Fig. 5.1, 1). A power supply is used to set the operating voltage to the mechanical stage and the electronics. A source/measure unit (SMU) is used to set the voltage bias to the SiPMs under test. The user can control all the operations through a custom LabVIEW interface installed in the main PC station of the facility.
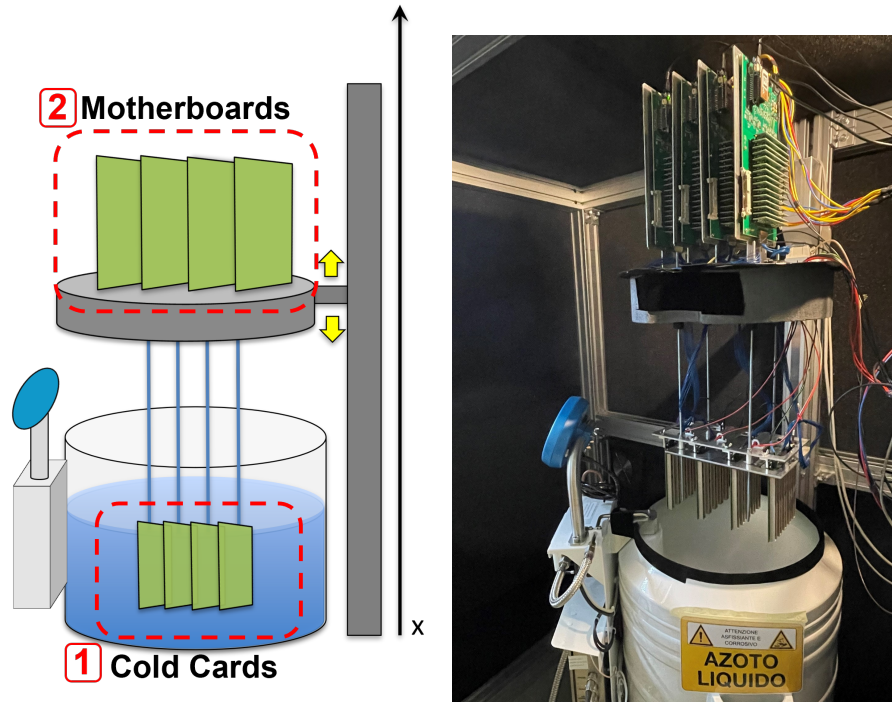
Figure 5.1: Left: sketch of the system used during the massive characterization. The samples under test are mounted on the Cold Cards (1) eventually submerged in LN2, while the motherboards, attached to the movable flange, host the warm electronics (2). Right: picture of the facility implemented in Bologna as one of the sites involved in the mass-test campaign. In the background the wall of the dark box.

5.1.1   Hardware and front-end electronics

The system presents four boards, named Cold Cards and developed by the electronics group of the Bologna INFN section, to which the SiPMs arrays under test are mounted. Up to 5 PCBs (30 SiPMs) are hosted on each Cold Card, for a total of 20 arrays (120 SiPMs). These are the only components that undergoes Liquid Nitrogen submersion during the validation procedure.

Each Cold Card is connected with a 30 channels cable (Samtec EQCD-020-23.62-SBR-SBR-1-B) to a board mounted on the top of the flange at room temperature, the SiPM signal is thus extracted and sent to the warm electronics. A platinum resistance termometer (PT100) is mounted on each Cold Card monitoring the temperature during the different phases of the thermal cycles. The SiPMs are biased through a coaxial cable splitted on one end into four lines connected to each cold board, while the other end is directly plugged to a source/measure unit (Keysight B2901A Series). All the cold electronics is composed of just passive

elements.

The warm electronics is composed of 4 motherboards attached 1:1 to the Cold Cards (Fig. 5.1). Each motherboard has plugged an Arduino MKR Zero as a micro-controller and 15 front-end cards for the signal amplification of two SiPMs each. Two flat cables on the two sides of each motherboards deliver the amplified signal to an FPGA-based system used to perform DCR measurements.A low-voltage power supply is used to power all the warm electronics and the DCR system. The Arduino MKR Zero are connected to and controlled by a Raspberry Pi 4, eventually connected to a switch inside a local network via ethernet. The main PC used to control the system and all the instruments are connected to the same network switch. The Raspberry Pi is plugged on to an ASIC board along with four Adafruit PT100 cards for the readout of the temperature sensors of the Cold Card. The diagram of the elements composing the testing facility is shown in Fig. 5.2.
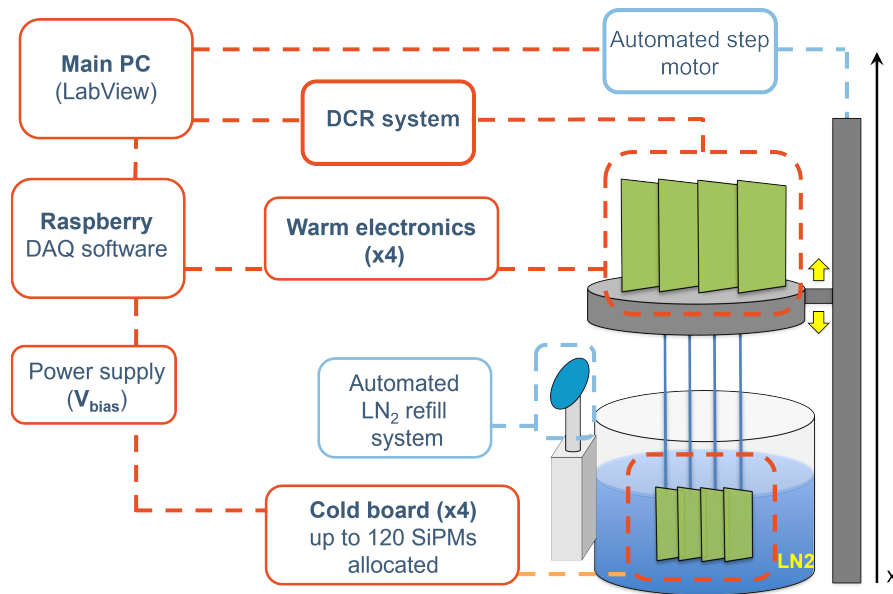
Figure 5.2: Diagram of the different elements composing the testing facility installed in the cryogenic laboratory of the INFN Bologna group. The system components are managed from the main PC station through a custom LabVIEW interface.

5.1.2 Software

The apparatus makes use of several software and scripts to perform the validation procedure. Two main python scripts run in parallel on the Raspberry Pi: one is used for the temperature measurements via the readout of the Adafruit PT100

cards, the other controls the data acquisition and analysis by communicating with the Arduino MKR Zero firmware and the SMU. The latter one interacts with the SMU setting up all the parameters for the I-V characteristics (as current and voltage range, number of steps or number of points for the curve) and performs the analysis extracting results for the characteristic values. An example of the output results obtained is reported in Fig. 5.3. The raw data and the results obtained
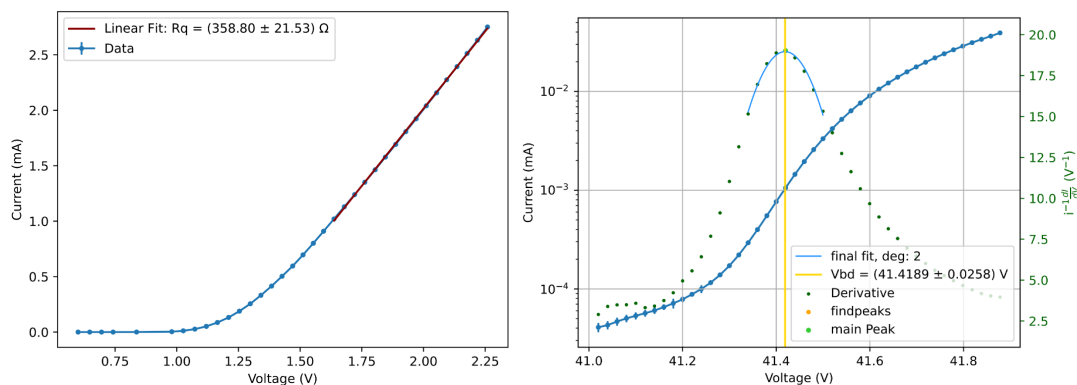
Figure 5.3: Example of the I-V curve measurements performed with the system: in a forward biased polarization (left) from which the value of quenching resistance is extracted, and in reverse polarization (right) obtaining the SiPM breakdown voltage value.

from the I-V curves are directly stored in the Raspberry Pi memory. A third python script runs on the main PC and is used for the DCR measurements: by communicating with a system controller, it configures the FPGA system for the counting measurements in a defined time window.

The start and operation of each code is managed by a LabVIEW interface working on the main PC. Through a custom interface specifically developed for the validation tests, to which I contributed, each operation of the system is controlled.

5.1.3 System operation

At the launch of the LabVIEW, an initial configuration window allows the user to (Fig. 5.4):

- set the different measurement parameters,

- set the sequence of movements for the mechanical stage,

- take note of all the information for the SiPMs load under test,

- select the path where to store all the resulting data.
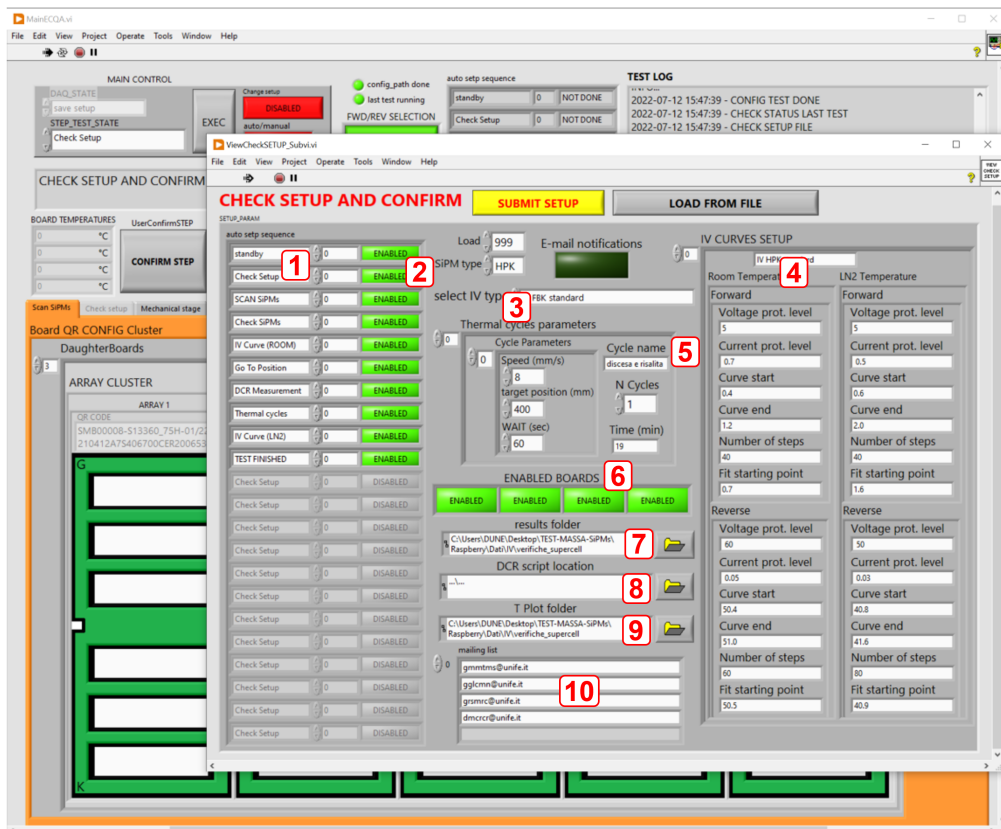
Figure 5.4: Initial configuration window displayed once the LabVIEW is launched. 1-2: name and enabling of the operations sequence used in the AUTO mode. 3-4: selection of the type of measurements and of the corresponding parameters. 5-6: selection of the sequence of step for a specific movements of the mechanical stage. 6: list of the enabled Cold Cards in the tests. 7-8-9: path in the main PC where to store the results data and to find the DCR script. 10: mailing list of people contacted by the system in case of errors.

Once the run started, the user can choose the operation mode. LabVIEW can operate in MANUAL or in AUTO mode, depending if the user wants to performed individual selected operations or a sequence of them, which can be customize on the initial configuration window.

As a first step, before mounting the samples on the Cold Cards, the user must scan a QR code present on the PCB of each arrays, with an optical reader connected via USB to the PC station. LabVIEW stores this information along with the SiPM position in which they are mounted, to associate the results of the analysis to the individual array.

Once the samples are mounted, if operating in MANUAL mode, the user can

start the validation procedure following the testing protocol described in Sec. 5.1 and selecting the corresponding operations. If a measurement is selected, Lab-VIEW automatically interacts with the corresponding python script without any other action from the user. The results of the analysis performed is displayed on the interface at the end of the operation. If instead a specific movements is demanded to the mechanical stage, the interface will communicate a defined sequence of steps to the automated step motor. During this phase, the temperature monitoring as a function of the position of the mechanical stage is also displayed and logged.

If the AUTO mode was chosen instead, once ended the initial operations for which the user action is requested, the pre-selected sequence of operations is executed.

The overall process to characterize up to 120 SiPMs with the facility lasts ∼4 hours.

5.2 Experimental results and analysis

5.2.1 ProtoDUNE SiPMs

In 2022, only the Ferrara and Bologna group had installed in their laboratories the facility for the mass test campaign. During the commissioning phase, both of them have been involved in the tests of all the SiPMs arrays belonging to the ProtoDUNE HD production. The results obtained from the operation of the Bologna system are reported in the following.

Since the FPGA-based system used to measure the DCR was not ready at that time, the data from the Bologna site include only the I-V measurements and are missing in the DCR ones. However, due to the tight schedule, the Consortium agreed to proceed in performing the tests even if not in the totality of the protocol.

Regarding the SiPMs FBK production for the ProtoDUNE PDS, 119 arrays (714 SiPMs) have been delivered and tested in Bologna while concerning the HPK batch, 89 arrays (534 SiPMs) were tested at our site.

The FBK samples were first delivered to Bologna at the beginning of 2022 and hence measured with the system in its early stage. Fig. 5.5 reports the results of the I-V curve measurements for the FBK SiPMs at room temperature, while Fig. 5.6 shows the quenching resistance (R_q) and breakdown voltage (V_{bd}) values distribution measured at their first LN2 bath. The distribution at both temperatures are within the experiment requirements, with a global spread in the V_{bd} at 77 K less than 2 V. After these initial tests, the totality of the samples have been validated through a sequence of two consecutive thermal cycles after which, the I-V curves measurements have been repeated. No significant variation in the main

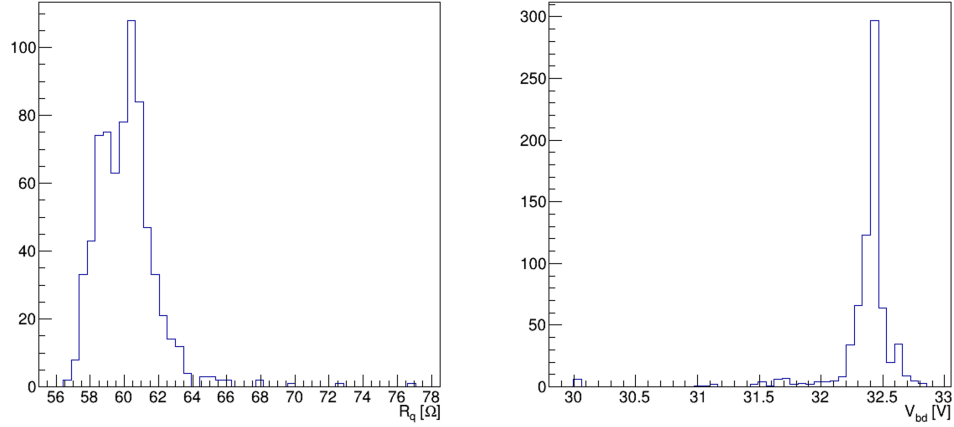features of the sensors has been observed as a consequence of the cycles, as shown in the Fig. 5.7.

Figure 5.5: Left: distribution of quenching resistance values for the FBK samples measured at T_{room}. Right: break down voltage values distribution measured at room temperature, of FBK samples for the ProtoDUNE HD production.
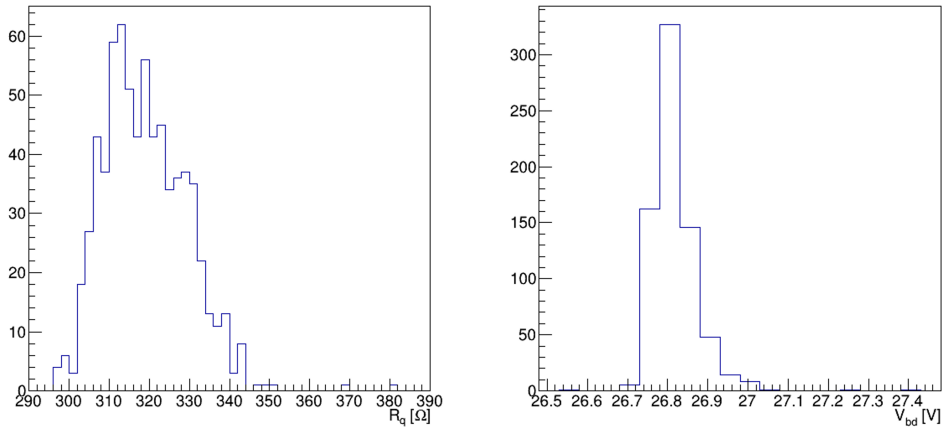

Figure 5.6: Left: distribution of the quenching resistance values in LN2 for the FBK SiPMs of ProtoDUNE-HD. Right: V_{bd} distribution for the FBK samples measured at 77 K.

The HPK production was delivered in late spring 2022 and measured after the completion of the FBK tests. Following the protocol I first performed the I-V measurements at room temperature, the results obtained are reported in Fig. 5.8.
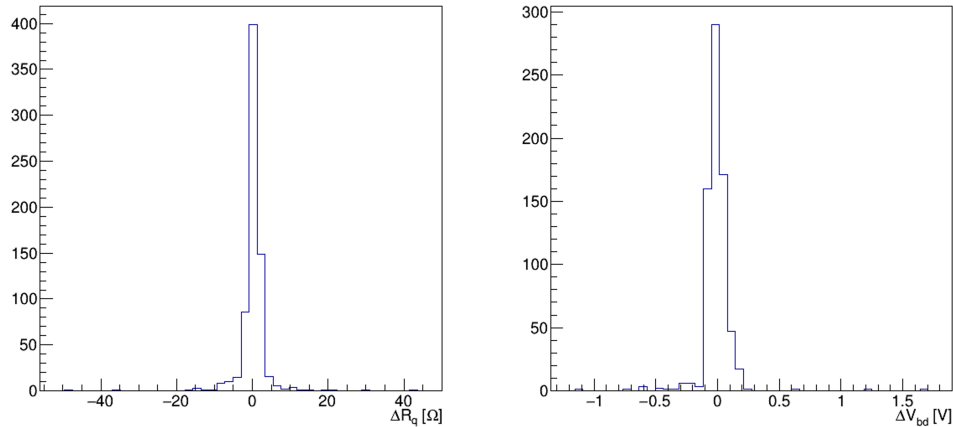
Figure 5.7: Variation of the quenching resistance (left) and breakdown voltage values (right) before and after the thermal cycles measured at 77 K, for the FBK samples tested. The outlier values in the histograms are attributed to issues with cable connections, affecting the results in one of the comparative measurements..

Then, measurements at 77 K were conducted. Fig. 5.9 shows the values distribution for the quenching resistance and breakdown voltage of the SiPMs in Liquid Nitrogen. The global spread in V_{bd} is less than 2 V, which meets the experimental requirements. Fig. 5.10 reports the variation of the same parameters before and after the completion of the thermal cycles: even in this case none of the samples showed any damage or significant effect. Although it was not possible to measure
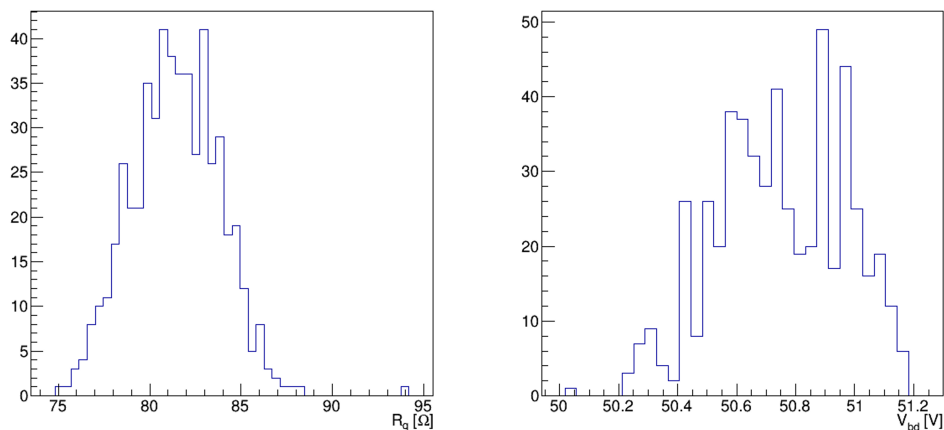
Figure 5.8: Quenching resistance (left) and breakdown voltage (right) values distribution obtained for the HPK samples measured at T_{room}.

107
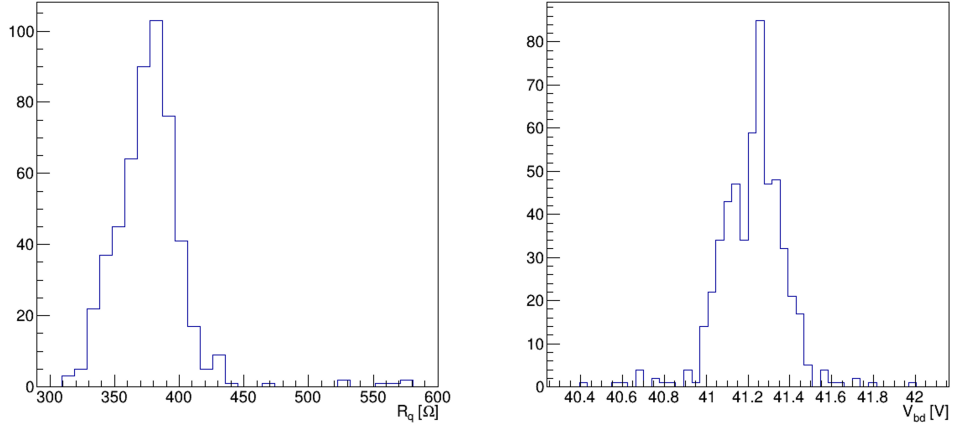
Figure 5.9: Quenching resistance (left) and breakdown voltage (right) values distribution obtained for the HPK samples measured at 77 K.
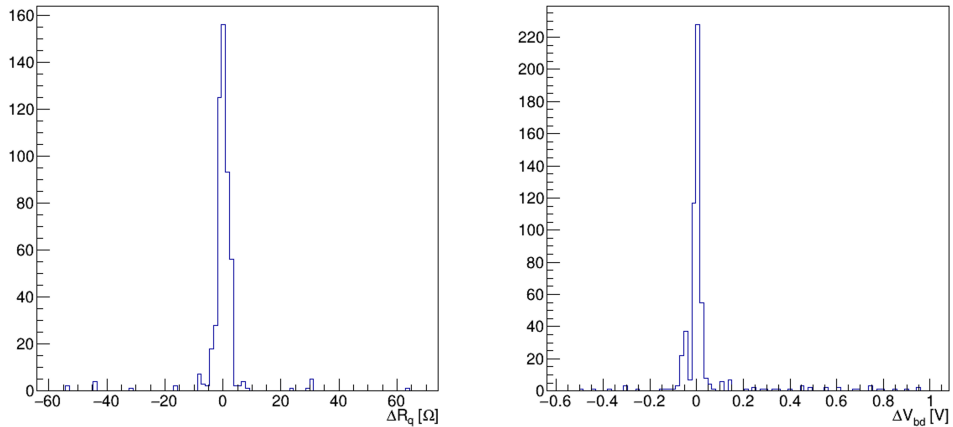
Figure 5.10: Variation of the quenching resistance (left) and breakdown voltage values (right) before and after the thermal cycles measured at 77 K, for the HPK samples tested.

the DCR during the SiPMs production validation for ProtoDUNE, I explored an alternative method to identify noisy samples. I conducted I-V curve analyses on some high DCR samples measured from other laboratories, along with an additional samples with low DCR. I then tested them in reverse bias polarization with an overvoltage up to +9 V, in a dark environment. The goal of these tests was to understand if an increase of the dark current at very high voltage could be observed.

108

The results obtained for both FBK and HPK samples are reported in Fig. 5.11. Even if the statistics of the investigation was limited, all the noisy SiPMs were spot-
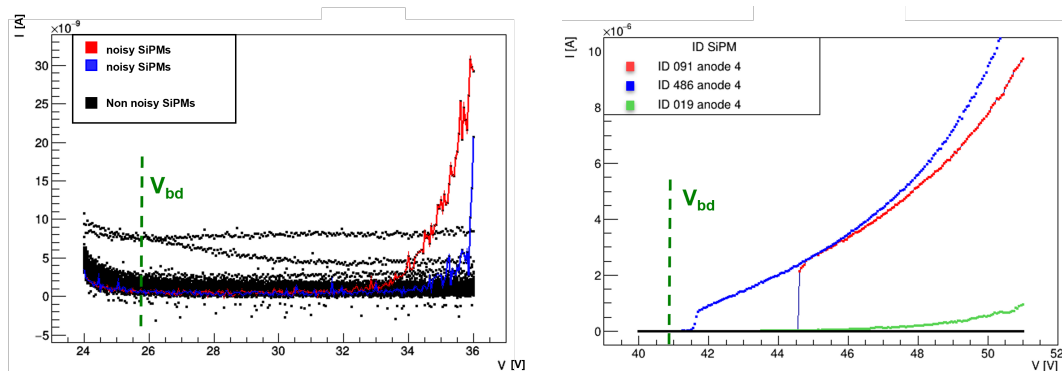
Figure 5.11: Left: comparison between I-V curve measured in dark for non noisy and noisy samples, for FBK SiPMs. In black the curves correspondent to the samples within the DCR requirements, in blue and red those out of specifications which show an increment of the dark current at high overvoltage. Right: the same type of mesurements performed with HPK samples. The black curves correspond to SiPMs with low DCR and the others of noisy sensors. Even in this case it can be observed an increment in the dark current well above the breakdown voltage, which is a clue for high DCR.

ted out from the others. This alternative method, named "extended I-V curves", was considered promising for the validation procedure, hence it was decided to include it in the mass-test protocol. This method, with a larger statistic, has the potential to investigate a correlation between its results and those obtained by the facility FPGA-system. While these latter one demand dedicated elements and operation of the facility, the extended I-V curves require only the control of a source measure unit, already implemented in the apparatus, offering a possible simplification of the system.

5.2.2   FD Module 1 SiPMs

The system's commissioning phase concluded successfully with the validation of SiPMs for the ProtoDUNE PDS. The initial testing phase led to several improvements both in the electronics and in the analysis:

- a new design for the warm electronics was implemented, initially developed using the only components available on the market in 2021, following the pandemic period. An optimization of its design became feasible only in late 2022;

- some problems in the continuity of the SiPMs signal observed during measurements in Liquid Nitrogen after the thermal cycles were solved by changing the cable connector attached to the Cold Card, with a new one less affected by humidity;

- the tools performing the data analysis were improved and optimized.

At the beginning of 2023 the system was in its full operational stage and from spring of the same year the mass test campaign of SiPMs for the PDS of the first module of Far Detector (FD1) started.

The first production of sensors delivered to be tested was that from HPK. The data I obtained participating in the validation campaign carried out in Bologna are presented in the following.

The batch was delivered organized in boxes of 400 arrays each (2400 SiPMs) and up to January 2024 Bologna received 7 boxes, having tested 5 of them, following the procedure reported in Sec. 5.1.

Fig. 5.12 shows the global distribution of the obtained values of quenching resistance (R_q) and breakdown voltage (V_{bd}) for all the samples tested at room temperature. The left plot presents some outliers due to some initial problem with the bias cable connected to the Cold Card and later solved. The right plot shows different populations in the distribution,due to different batch production.
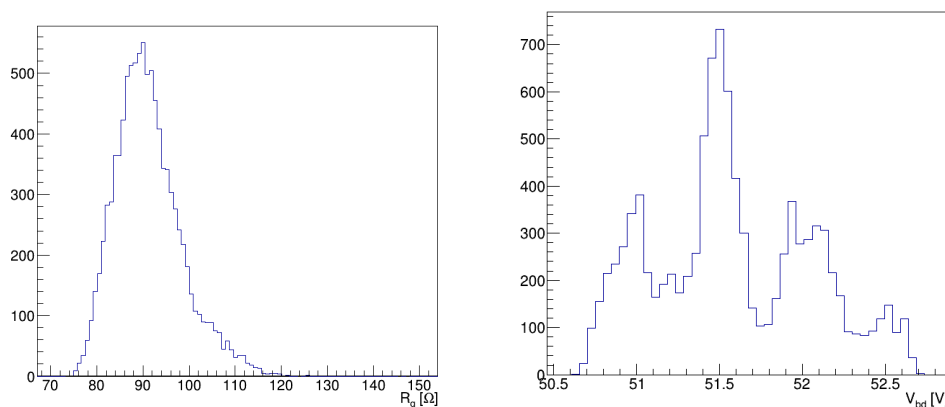
Figure 5.12: Left: distribution of values for the quenching resistance at room temperature. The outlayers are connected with some problems in the cable used to deliver the bias to the arrays and now solved. Right: Distribution of values for the breakdown voltage, different populations due to different SiPMs batch production are visible.

After the first submersion and measurement in the cryogenic bath, all the thermal stress tests were performed. Fig. 5.13 reports the results of R_q and V_{bd}

measured at 77 K after the thermal cycles. As in the case of the measurements at T_{room}, different populations in the breakdown voltage values due to different SiPMs batch production are visible Fig. 5.13. This trend is also reflected in Fig. 5.14. The variations of quenching resistance and breakdown voltage before and after the thermal tests are shown in Fig. 5.15. As demanded by the validation protocol, at
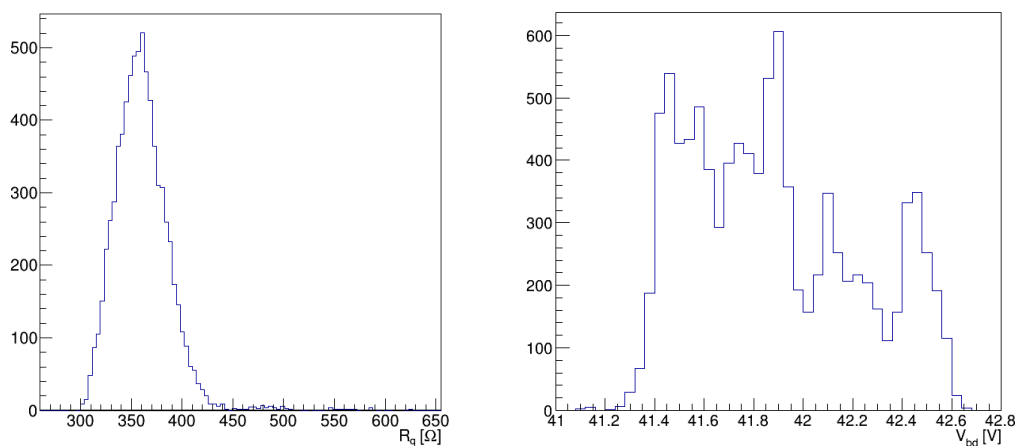

Figure 5.13: Left: distribution of R_q measured at 77 K after the thermal cycles. Right: values for V_{bd} at the same temperature and condition.
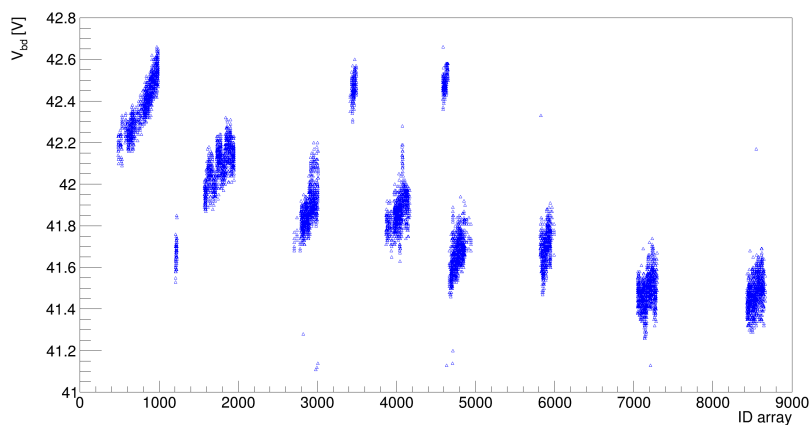
Figure 5.14: V_{bd} values as a function of the arrays ID. Grouped of similar breakdown voltage values correspond to different SiPMs batch production and closed array ID.

the last bath in Liquid Nitrogen, the Dark Count Rate (DCR) of the samples was

111
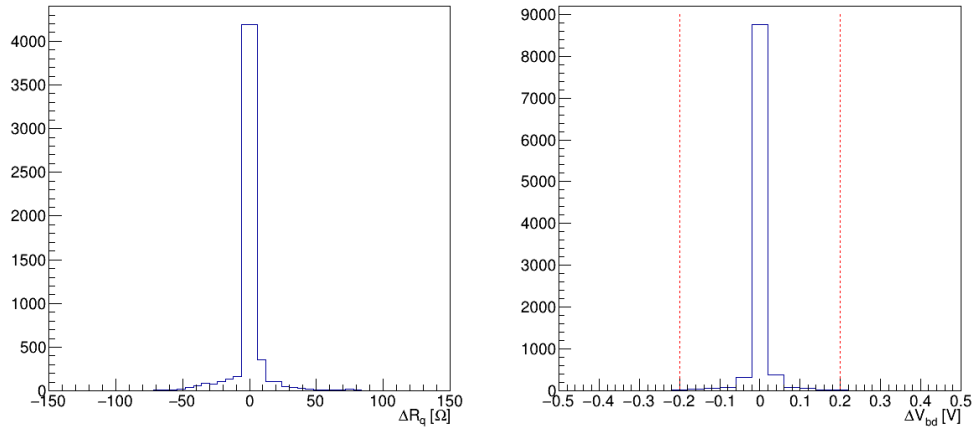
Figure 5.15: Variation in the quenching resistance (left) and breakdown voltage values (right) measured at 77 K, before and after the thermal cycles.

measured in complete dark along with the extended I-V curves. The distribution of the obtained values for the DCR is reported in Fig. 5.16. During the DCR tests one channel reported systematically high level of noise, invalidating the measurements for the correspondent SiPMs. These samples have been removed from the distribution and will be individually tested with a separated setup. Few sensors present DCR values larger than 200 mHz/mm², but with no correlated anomalies in the extended I-V measurements. These SiPMs could have been affected by the burst phenomenon (Sec. 4.3.5) and will be part of those samples to be fully characterized by other labs of the Consortium. On the totality of the arrays validated, only 3 SiPMs showed very large values of DCR correlated with an increase in the current at high values of overvoltage for the extended I-V. These samples (not shown in Fig. 5.16) were considered out of specifications and discard.
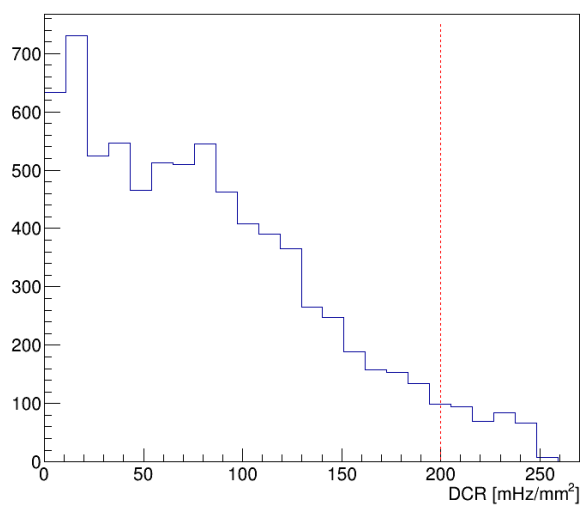
Figure 5.16: Distribution of the Dark Count Rate for measured in Liquid Nitrogen for the HPK samples tested. From the population were removed the samples correspondent to one channel of the system systematically affected by some external electronic noise. The SiPMs with DCR>200 mHz/mm² will be fully characterized in a dedicated setup, to exclude the effect of burst of signal.

Conclusions

The work presented in this thesis has been carried out in the framework of the DUNE experiment.

DUNE will provide measurements of oscillation parameters with unprecedented levels of precision, giving an important contribution to the field. Its design foresees a dual-site structure, with a Near Detector (ND) and a Far Detector (FD) placed at ~1300 km distance. The main purpose of the ND will be the characterization and monitoring of the neutrino beam near its source and the reduction of systematic uncertainties in the analysis of neutrino event data at the Far Detector. At the far-site the FD will observe and reconstruct neutrino interactions. The FD will be composed of four modules of Liquid Argon Time Projection Chamber. The Photon Detection System (PDS) that detects the scintillation light produced in neutrino interactions is composed of light collectors coupled to Silicon Photomultipliers (SiPMs). Given the challenging working conditions, a careful selection of the devices that fulfill all the experiment requirements was performed as well as a characterization and qualification campaign before the PDS installation. Detailed specifications for the samples have been determined in terms of uniformity of their properties, level of noise, efficiency and reliability.

This thesis reports all the activities that I carried out on the selection, characterization, and validation of the SiPMs that eventually will be in the PDS of the first module of DUNE Far Detector (FD1).

During a first phase, different photosensor technologies have been proposed and produced in order to identify the samples that best match the experiment requirements. The evaluated samples presented a $6{\times}6$ mm^2 surface with different cell pitch (30, 50 and 75 μm), quenching resistance and technology. A description of the validation tests and down-selection criteria adopted are reported. The properties of the SiPMs have been tested both at room and cryogenic temperature, showing a uniformity in the quenching resistance (R_q) and breakdown voltage (V_{bd}). In FD1, the final configuration of a Supercell envisages 48 SiPMs electrically connected in parallel (passively ganged), summing their signal in order to reduce the total amount of readout channels in the experiment. With this configuration, groups of SiPMs are biased with the same voltage. Therefore, it is important that

the grouped ones present breakdown voltages (V_{bd}) as similar as possible. Large discrepancies in the values of V_{bd} would imply different gain for the grouped SiPMs and thus a loss in the uniformity of the PDS response. The reported tests results showed a good agreement with this request with a global spread in the V_{bd}<2 V. The main sources of noise have been studied at 77 K, along with an unexpected newly observed burst of signals phenomenon affecting the SiPMs noise level. The measurements obtained are compatible with the experiment requirements. The Dark Count Rate was measured to be <200 mHz/mm^2 and the correlated noise are within the specification. Having a low photosensor noise, is critical to ensure a good signal to noise ratio in the read out electronics. The samples have been validated through a series of thermal stress tests. All of them showed no mechanical damage as well as no change in their main features. From the evaluation of some Figure of Merit the selected model for the mass production was the 75 μm High Quenching Resistance (HQR) model produced by Hamamatsu Photonics K.K. (HPK) and the NUV-HD-cryo Triple Trench technology from Fondazione Bruno Kessler (FBK).

Once concluded the selection campaign, a larger number of SiPMs was produced, for the PDS of ProtoDUNE Single Phase Horizontal Drift, at CERN. A specific setup has been developed in order to automate the validating procedure of all the sensors before instrumenting the detector. I was involved in the installation and commissioning of a testing facility in Bologna: during the latter phase ∼1300 SiPMs were tested using the system. The results showed no significant damages after the thermal stress tests and in the variation of the sensors properties. The spread in the values of the SiPMs quenching resistance and breakdown voltage have been analyzed and judged compliant with the requirements.

This phase serves as a test bench for the final production and validation of the photosensors to be installed in the first module of DUNE Far Detector. Currently a mass test campaign is ongoing to validate a first production and the data obtained so far are here reported.

Concluding, thanks to the results reported in this thesis it was possible to select and validate the technology adopted for the production of the SiPMs and to develop a custom cryogenic facility for the required measurements. The different results discussed in this thesis are relevant for other photon detectors operated in cryogenic environment in several applications.

Bibliography

[1] P.W. Higgs. "Broken symmetries, massless particles and gauge fields". In: *Physics Letters* 12.2 (1964), pp. 132–133. ISSN: 0031-9163. DOI: https://doi.org/10.1016/0031-9163(64)91136-9. URL: https://www.sciencedirect.com/science/article/pii/0031916364911369.

[2] ALEPH Collaboration. "A precise determination of the number of families with light neutrinos and of the Z boson partial widths". In: *Physics Letters B* 235.3 (1990), pp. 399–411. ISSN: 0370-2693. DOI: https://doi.org/10.1016/0370-2693(90)91984-J. URL: https://www.sciencedirect.com/science/article/pii/037026939091984J.

[3] Gregg B. Franklin. *The KATRIN Neutrino Mass Measurement: Experiment, Status, and Outlook*. 2018. arXiv: 1809.10603 [physics.ins-det].

[4] N. Aghanim et al. "Planck2018 results: VI. Cosmological parameters". In: *Astronomy amp; Astrophysics* 641 (Sept. 2020), A6. ISSN: 1432-0746. DOI: 10.1051/0004-6361/201833910. URL: http://dx.doi.org/10.1051/0004-6361/201833910.

[5] Carlo Giunti and Kim Chung Wook. *Fundamentals of Neutrino Physics and Astrophysics*. Oxford: Oxford Univ., 2007. DOI: 10.1093/acprof:oso/9780198508717.001.0001. URL: https://cds.cern.ch/record/1053706.

[6] Maurizio Spurio. *Probes of Multimessenger Astrophysics: Charged cosmic rays, neutrinos, γ-rays and gravitational waves*. Astronomy and Astrophysics Library. Springer, 2018. DOI: 10.1007/978-3-319-96854-4.

[7] Aldo Serenelli. "Alive and well: A short review about standard solar models". In: *The European Physical Journal A* 52.4 (Apr. 2016). DOI: 10.1140/epja/i2016-16078-1. URL: https://doi.org/10.1140%2Fepja%2Fi2016-16078-1.

[8] B. T. Cleveland et al. "Measurement of the solar electron neutrino flux with the Homestake chlorine detector". In: *Astrophys. J.* 496 (1998), pp. 505–526. DOI: 10.1086/305343.

[9] KS Hirata et al. "Real-time, directional measurement of 8B solar neutrinos in the Kamiokande II detector." In: *Physical review D: Particles and fields* 44 (Nov. 1991), pp. 2241–2260.

[10] R.Jeffrey Wilkes. "Results on neutrino oscillations from Super-Kamiokande". In: *Advances in Space Research* 26.11 (2000), pp. 1813–1822. ISSN: 0273-1177. DOI: https://doi.org/10.1016/S0273-1177(99)01228-4. URL: https://www.sciencedirect.com/science/article/pii/S0273117799012284.

[11] M.P. Decowski. "KamLAND's precision neutrino oscillation measurements". In: *Nuclear Physics B* 908 (2016). Neutrino Oscillations: Celebrating the Nobel Prize in Physics 2015, pp. 52–61. ISSN: 0550-3213. DOI: https://doi.org/10.1016/j.nuclphysb.2016.04.014. URL: https://www.sciencedirect.com/science/article/pii/S0550321316300529.

[12] Sindhujha Kumaran et al. "Borexino Results on Neutrinos from the Sun and Earth". In: *Universe* 7.7 (July 2021), p. 231. DOI: 10.3390/universe7070231. URL: https://doi.org/10.3390%2Funiverse7070231.

[13] The Borexino Collaboration M. Agostini. "Experimental evidence of neutrinos produced in the CNO fusion cycle in the Sun". In: *Nature* 587 (2020), pp. 577–582. ISSN: 7835. DOI: 10.1038/s41586-020-2934-0. URL: https://doi.org/10.1038/s41586-020-2934-0.

[14] Y. Fukuda et al. "Evidence for oscillation of atmospheric neutrinos". In: *Phys. Rev. Lett.* 81 (1998), pp. 1562–1567. DOI: 10.1103/PhysRevLett.81.1562. arXiv: hep-ex/9807003.

[15] Yasuo Takeuchi. "Recent results and future prospects of Super-Kamiokande". In: *Nuclear Instruments and Methods in Physics Research Section A: Accelerators, Spectrometers, Detectors and Associated Equipment* 952 (2020). 10th International Workshop on Ring Imaging Cherenkov Detectors (RICH 2018), p. 161634. ISSN: 0168-9002. DOI: https://doi.org/10.1016/j.nima.2018.11.093. URL: https://www.sciencedirect.com/science/article/pii/S0168900218317200.

[16] The Double Chooz Collaboration. "Double Chooz θ_{13} measurement via total neutron capture detection". In: *Nature Physics* 16 (5 2020), pp. 558–564. ISSN: 1745-2481. DOI: 10.1038/s41567-020-0831-y. URL: https://doi.org/10.1038/s41567-020-0831-y.

[17] RENO Collaboration and J. K. Ahn. *RENO: An Experiment for Neutrino Oscillation Parameter theta_13 Using Reactor Neutrinos at Yonggwang.* 2010. arXiv: 1003.1391 [hep-ex].

[18] Daya Bay Collaboration. *A Precision Measurement of the Neutrino Mixing Angle theta˙13 using Reactor Antineutrinos at Daya Bay*. 2007. arXiv: hep-ex/0701029 [hep-ex].

[19] F. P. An et al. "Measurement of electron antineutrino oscillation based on 1230 days of operation of the Daya Bay experiment". In: *Phys. Rev. D* 95 (7 Apr. 2017), p. 072006. DOI: 10.1103/PhysRevD.95.072006. URL: https://link.aps.org/doi/10.1103/PhysRevD.95.072006.

[20] S. Abe et al. "Precision Measurement of Neutrino Oscillation Parameters with KamLAND". In: *Physical Review Letters* 100.22 (June 2008). DOI: 10.1103/physrevlett.100.221803. URL: https://doi.org/10.1103%2Fphysrevlett.100.221803.

[21] M. H. Ahn et al. "Measurement of neutrino oscillation by the K2K experiment". In: *Phys. Rev. D* 74 (7 Oct. 2006), p. 072003. DOI: 10.1103/PhysRevD.74.072003. URL: https://link.aps.org/doi/10.1103/PhysRevD.74.072003.

[22] P. Adamson et al. "Combined Analysis of ν_μ Disappearance and $\nu_\mu \to \nu_e$ Appearance in MINOS Using Accelerator and Atmospheric Neutrinos". In: *Phys. Rev. Lett.* 112 (19 May 2014), p. 191801. DOI: 10.1103/PhysRevLett.112.191801. URL: https://link.aps.org/doi/10.1103/PhysRevLett.112.191801.

[23] N. Agafonova et al. "Discovery of τ Neutrino Appearance in the CNGS Neutrino Beam with the OPERA Experiment". In: *Phys. Rev. Lett.* 115 (12 Sept. 2015), p. 121802. DOI: 10.1103/PhysRevLett.115.121802. URL: https://link.aps.org/doi/10.1103/PhysRevLett.115.121802.

[24] M.G. Catanesi. "T2K Results and Perspectives". In: *Nuclear Physics B - Proceedings Supplements* 237-238 (2013). Proceedings of the Neutrino Oscillation Workshop, pp. 129–134. ISSN: 0920-5632. DOI: https://doi.org/10.1016/j.nuclphysbps.2013.04.074. URL: https://www.sciencedirect.com/science/article/pii/S0920563213001953.

[25] L Kolupaeva and for the NOvA collaboration. "Recent three-flavor neutrino oscillation results from the NOvA experiment". In: *Journal of Physics: Conference Series* 1690.1 (Dec. 2020), p. 012172. DOI: 10.1088/1742-6596/1690/1/012172. URL: https://dx.doi.org/10.1088/1742-6596/1690/1/012172.

[26] The T2K Collaboration. "Constraint on the matter–antimatter symmetry-violating phase in neutrino oscillations". In: *Nature* 580 (2020), pp. 339–344. ISSN: 7803-1476-4687. DOI: 10.1038/s41586-020-2177-0. URL: https://doi.org/10.1038/s41586-020-2177-0.

[27] Ivan Esteban et al. "The fate of hints: updated global analysis of three-flavor neutrino oscillations". In: *Journal of High Energy Physics* 2020.9 (Sept. 2020). ISSN: 1029-8479. DOI: 10.1007/jhep09(2020)178. URL: http://dx.doi.org/10.1007/JHEP09(2020)178.

[28] B. Abi et al. *Deep Underground Neutrino Experiment (DUNE), Far Detector Technical Design Report, Volume I: Introduction to DUNE.* 2020. eprint: 2002.02967.

[29] James Strait et al. *Long-Baseline Neutrino Facility (LBNF) and Deep Underground Neutrino Experiment (DUNE) Conceptual Design Report Volume 3: Long-Baseline Neutrino Facility for DUNE June 24, 2015.* 2016. arXiv: 1601.05823 [physics.ins-det].

[30] M. Ball et al. "The PIP-II Conceptual Design Report". In: (Mar. 2017). DOI: 10.2172/1346823. URL: https://www.osti.gov/biblio/1346823.

[31] A. Abed Abud et al. *Deep Underground Neutrino Experiment (DUNE) Near Detector Conceptual Design Report.* 2021. arXiv: 2103.13910 [physics.ins-det].

[32] B. Abi et al. *Deep Underground Neutrino Experiment (DUNE), Far Detector Technical Design Report, Volume IV: Far Detector Single-phase Technology.* 2020. arXiv: 2002.03010 [physics.ins-det].

[33] B. Abi et al. "First results on ProtoDUNE-SP liquid argon time projection chamber performance from a beam test at the CERN Neutrino Platform". In: *Journal of Instrumentation* 15.12 (Dec. 2020), P12004–P12004. DOI: 10.1088/1748-0221/15/12/p12004. URL: https://doi.org/10.1088%2F1748-0221%2F15%2F12%2Fp12004.

[34] Adam Abed Abud et al. "Scintillation light detection in the 6-m drift-length ProtoDUNE Dual Phase liquid argon TPC". In: *Eur. Phys. J. C* 82.7 (2022), p. 618. DOI: 10.1140/epjc/s10052-022-10549-w. arXiv: 2203.16134 [physics.ins-det].

[35] LBNE Collaboration et al. *The Long-Baseline Neutrino Experiment: Exploring Fundamental Symmetries of the Universe.* 2014. arXiv: 1307.7335 [hep-ex].

[36] DUNE Collaboration et al. *Snowmass Neutrino Frontier: DUNE Physics Summary.* 2022. arXiv: 2203.06100 [hep-ex].

[37] Hans-Thomas Janka. "Neutrino Emission from Supernovae". In: *Handbook of Supernovae.* Ed. by Athem W. Alsabti and Paul Murdin. Cham: Springer International Publishing, 2017, pp. 1575–1604. ISBN: 978-3-319-21846-5. DOI: 10.1007/978-3-319-21846-5_4. URL: https://doi.org/10.1007/978-3-319-21846-5_4.

[38] B. Abi et al. *Deep Underground Neutrino Experiment (DUNE), Far Detector Technical Design Report, Volume II: DUNE Physics.* 2020. arXiv: 2002.03005 [hep-ex].

[39] Ettore Segreto. "Properties of liquid argon scintillation light emission". In: *Phys. Rev. D* 103 (4 Feb. 2021), p. 043001. DOI: 10.1103/PhysRevD.103.043001. URL: https://link.aps.org/doi/10.1103/PhysRevD.103.043001.

[40] T Doke. "Fundamental properties of liquid argon, krypton and xenon as radiation detector media". In: *Portugal. Phys.* 12.1-2 (1981), pp. 9–48. URL: https://cds.cern.ch/record/432394.

[41] C. Vogl et al. "Scintillation and optical properties of xenon-doped liquid argon". In: *Journal of Instrumentation* 17.01 (Jan. 2022), p. C01031. DOI: 10.1088/1748-0221/17/01/C01031. URL: https://dx.doi.org/10.1088/1748-0221/17/01/C01031.

[42] E. Segreto et al. "Liquid argon test of the ARAPUCA device". In: *Journal of Instrumentation* 13.08 (Aug. 2018), P08021–P08021. ISSN: 1748-0221. DOI: 10.1088/1748-0221/13/08/p08021. URL: http://dx.doi.org/10.1088/1748-0221/13/08/P08021.

[43] C. Brizzolari et al. "Cryogenic front-end amplifier design for large SiPM arrays in the DUNE FD1-HD photon detection system". In: *JINST* 17.11 (2022), P11017. DOI: 10.1088/1748-0221/17/11/P11017. arXiv: 2207.13616 [physics.ins-det].

[44] P. Carniti et al. "A low noise and low power cryogenic amplifier for single photoelectron sensitivity with large arrays of SiPMs". In: *JINST* 15.01 (Jan. 2020), P01008–P01008. DOI: 10.1088/1748-0221/15/01/p01008. URL: https://doi.org/10.1088/1748-0221/15/01/p01008.

[45] Babak Abi et al. "Deep Underground Neutrino Experiment (DUNE), Far Detector Technical Design Report, Volume III: DUNE Far Detector Technical Coordination". In: *JINST* 15.08 (2020), T08009. DOI: 10.1088/1748-0221/15/08/T08009. arXiv: 2002.03008 [physics.ins-det].

[46] Alberto Gola et al. "NUV-Sensitive Silicon Photomultiplier Technologies Developed at Fondazione Bruno Kessler". In: *Sensors* 19.2 (2019). ISSN: 1424-8220. DOI: 10.3390/s19020308. URL: https://www.mdpi.com/1424-8220/19/2/308.

[47] Massimo Capasso et al. "FBK VUV-sensitive Silicon Photomultipliers for cryogenic temperatures". In: *Nuclear Instruments and Methods in Physics Research Section A: Accelerators, Spectrometers, Detectors and Associated Equipment* 982 (2020), p. 164478. ISSN: 0168-9002. DOI: https://doi.org/10.

1016/j.nima.2020.164478. URL: https://www.sciencedirect.com/science/article/pii/S0168900220308755.

[48] Niccolò Gallice et al. "Development of a design for SiPMs readout in cryogenic environment for large area photon detectors". In: *2021 IEEE International Instrumentation and Measurement Technology Conference (I2MTC)*. 2021, pp. 1–6. DOI: 10.1109/I2MTC50364.2021.9459995.

[49] Carmen Palomares. "Detection efficiency measurement and operational tests of the X-Arapuca for the first module of DUNE far detector". In: *JINST* 18.02 (2023), p. C02064. DOI: 10.1088/1748-0221/18/02/C02064. arXiv: 2211.15503 [hep-ex].

[50] Fabio Acerbi et al. "Cryogenic Characterization of FBK HD Near-UV Sensitive SiPMs". In: *IEEE Transactions on Electron Devices* 64.2 (2017), pp. 521–526. DOI: 10.1109/TED.2016.2641586.

[51] G. Collazuol et al. "Studies of silicon photomultipliers at cryogenic temperatures". In: *Nuclear Instruments and Methods in Physics Research Section A: Accelerators, Spectrometers, Detectors and Associated Equipment* 628.1 (2011). VCI 2010, pp. 389–392. ISSN: 0168-9002. DOI: https://doi.org/10.1016/j.nima.2010.07.008. URL: https://www.sciencedirect.com/science/article/pii/S0168900210015500.

[52] M. Andreotti et al. "Cryogenic characterization of Hamamatsu HWB MPPCs for the DUNE photon detection system". In: *Journal of Instrumentation* 19.01 (Jan. 2024), T01007. DOI: 10.1088/1748-0221/19/01/T01007. URL: https://dx.doi.org/10.1088/1748-0221/19/01/T01007.

[53] M. Guarise et al. "A newly observed phenomenon in the characterisation of SiPM at cryogenic temperature". In: *JINST* 16.10 (Oct. 2021), T10006. DOI: 10.1088/1748-0221/16/10/T10006. URL: https://dx.doi.org/10.1088/1748-0221/16/10/T10006.